The Evolution of Galaxies in Proto-clusters

Stephane V. Werner

Thesis submitted to the University of Nottingham
for the degree of Doctor of Philosophy

February 2023

Supervisors:	Dr. Nina Hatch	
Examiners:	Dr. John Stott	(Lancaster University)
	Prof. Meghan Gray	(University of Nottingham)
Examination chair:		
Submitted:	4th February 2023	
Examined:	30th March 2023	
Final version:	Date	

Contents

List of Tables

List of Figures

Abstract

In this thesis, I report on my work on galaxy evolution in proto-clusters. In Chapter 1, I describe previous knowledge about clusters and proto-clusters of galaxies. The next three Chapters correspond to three different projects I have completed during my PhD that are connected to the topic of galaxy evolution in proto-clusters.

In Chapter 2, I quantify the relative importance of environmental quenching versus pre-processing in $z \sim 1$ clusters by analysing the infalling galaxy population in the outskirts of 15 galaxy clusters at $0.8 < z < 1.4$ drawn from the GOGREEN and GCLASS surveys. I find significant differences between the infalling galaxies and a control sample; in particular, an excess of massive quiescent galaxies in the infalling region. These massive infalling galaxies likely reside in larger dark matter haloes than similar-mass control galaxies because they have twice as many satellite galaxies. Based on these findings, I conclude that it may not be appropriate to use 'field' galaxies as a substitute for infalling pre-cluster galaxies when calculating the efficiency and mass dependency of environmental quenching in high redshift clusters. By comparing the quiescent fraction of infalling galaxies at $1 < R/\mathrm{R}_{200} < 3$ to the cluster sample ($R/\mathrm{R}_{200} < 1$) I find that almost all quiescent galaxies with masses $> 10^{11}\,\mathrm{M}_{\odot}$ were quenched prior to infall, whilst up to half of lower mass galaxies were environmentally quenched after passing the virial radius. This means most of the massive quiescent galaxies in $z \sim 1$ clusters were self-quenched or pre-processed prior to infall.

In Chapter 3, I report on my work on intracluster light in proto-clusters at $z \sim 2$. In contrast to theoretical expectations, I report on the detection of intracluster light within two proto-clusters at $z = 2$ using deep *HST* images. I use the colour of the intracluster light to estimate its mass-to-light ratio in annuli around the brightest cluster galaxies (BCG), up to a radius of 100 kpc. I find that $54 \pm 5\%$ and $71 \pm 3\%$ of the stellar mass in these regions is located more than 10 kpc away from the BCGs in the two proto-clusters. This low concentration is similar to BCGs in lower redshift clusters, and distinct from other massive proto-cluster galaxies. This suggests that the proto-cluster BCGs have already experienced a special merger history similar to their lower redshift counterparts. We compare these observations to the Hydrangea hydrodynamical galaxy cluster simulations. In contrast to semi-analytic models, they predict that intracluster stars are a generic feature of massive halos since at least $z = 2$. This implies that intracluster light is a natural consequence of hierarchical structure formation.

Over Chapter 4, I report on my work on the luminosity function and D_n4000 measurements of proto-cluster galaxies at $1.3 < z < 3.0$. Using *HST* grism data, I found that the luminosity function of proto-clusters differ from the field, such that proto-clusters have an excess of luminous galaxies. I also found that proto-cluster galaxies have higher values of D_n4000 compared to field galaxies. We interpret

that proto-cluster galaxies have older stellar populations than field galaxies.

In Chapter 5, I summarise my main findings on this work and plans for future work.

Acknowledgements

Before starting the acknowledgements, I would like to give the context in which the work of this thesis was developed. During these three years of PhD, most of the time was during a pandemic. We had to isolate, and all the meetings were virtual. We had to reinvent ourselves and the way we do science. During this time, a few people were essential and helped me immensely in many senses.

First of all, I want to acknowledge my family. My father, mother and grandmothers were always with me when I needed the most. Thank you for all the support and love you gave me.

My Brazilian friends helped me in many situations. Leonardo helped me a lot when I arrived here in Nottingham and during my PhD period. Thanks, Arthur, for all the help, advice and hangouts. Although we met later, Vitor was crucial to me during the period I was writing this thesis - thanks for the fun playing Mario Kart. Also, my Brazilian friends in Brazil/USA were the best during my PhD. Thank you, Roberta, Aline, Natasha and Karol, for everything. I cannot count how often you listened to me when I needed it.

When I arrived here, I made new friends that were really important to me during this phase. Thanks, Charutha, for being the best friend I could ask for during my time here. Thank you, Karel, Tomáš and CB, for being so receptive when I arrived and being so lovely all the time. Thanks, Mick, Roan, and Jacob for all the parties at the DA. Swagat and Agustin, thank you for the drinks together. Thanks for all the fun, Dan, Matt, Molly, Lizzie, Brad, Sergio, Sukhi, and Liza.

I was also involved with science outreach during this time, mainly on the internet. The support my followers gave me many times when I did not believe in myself was really important. Sometimes I thought I would be unable to do some tasks or I was feeling low due to something, and they gave me all the support. Thank you, everyone.

I also thank Anthony Gonzalez for his help and advice in many situations.

Finally, I would like to thank Nina Hatch for all her patience and support. I could not ask for better supervision for this work. I learned a lot from her; she helped me to improve and be a better researcher.

Published works

The content of two Chapters in this thesis has been published or submitted for publication in the following works:

I **Werner, S. V.**, Hatch N. A., Muzzin A., van der Burg R. F. J., Balogh M. L., Rudnick G. , Wilson G., 2021. *Satellite quenching was not important for z∼1 clusters: most quenching occurred during infall.* Monthly Notices of the Royal Astronomical Society, Volume 510, Issue 1, pp.674-686

II **Werner, S. V.**, Hatch N. A., Matharu J., Gonzalez A. H., Bahé Y. M., Mei S. , Noirot G., Wylezalek D., 2023. *Intracluster light in the core of z∼2 galaxy proto-clusters.* Submitted to Monthly Notices of the Royal Astronomical Society

Chapter 2 has a description of the work published in Paper I, Chapter 3 is based on the work submitted in Paper II. Chapter 4 is based on an ongoing work with preliminary results.

The major part of this thesis was carried out by me, with advice from collaborators and co-authors. Data products of other works and collaborations are explicitly described and detailed through the text.

Chapter 1

Introduction

1.1 A brief history of extragalactic research

Galaxies have been observed by humans since early times. The first documented observation and description of another galaxy was made by the Persian astronomer al-Sufi in his "Book of Fixed Stars" that was written around 903-986 (Fī, 903). He described the Andromeda galaxy as a "small cloud". The first observations of Andromeda by Persian astronomers were probably before 905. Later, galaxies were commonly described as 'nebulous' objects. Until the beginning of the XX century, we did not know their nature and whether they were inside or outside our Galaxy, the Milky Way. The famous debate between Curtis and Shapley about the existence of the 'island universes' ended when Edwin Hubble measured the distance of Andromeda galaxy using the period-luminosity relation for Cepheids stars. This relation was discovered by Henrietta Leavitt years before, who correlated the luminosity of these variable stars with their pulsation period (Leavitt & Pickering, 1912). Using these variable stars in the Andromeda galaxy, Hubble measured its distance and found that Andromeda was too far away to be inside the Milky Way,

and concluded it was a separate galaxy, like our Galaxy (Hubble, 1929).

This started a new era in astronomy and a new field arose: extragalactic astrophysics, which is the astrophysics of objects outside the Milky Way. Hubble also classified galaxies according to their morphologies, including ellipticals (E), lenticulars (S0), spirals (S) and irregulars (Irr) (Hubble, 1926, 1927), as can be seen in Figure 1.1. This classification later evolved and became more detailed and internal structures of galaxies were taken into account, such as bulges, bars, spiral arms and the surface brightness profile of the galaxy (Sérsic, 1963; de Vaucouleurs, 1959). Figure 1.1 shows an illustration of the different types of galaxies with different morphologies, number of spiral arms, and bulge and bar sizes.

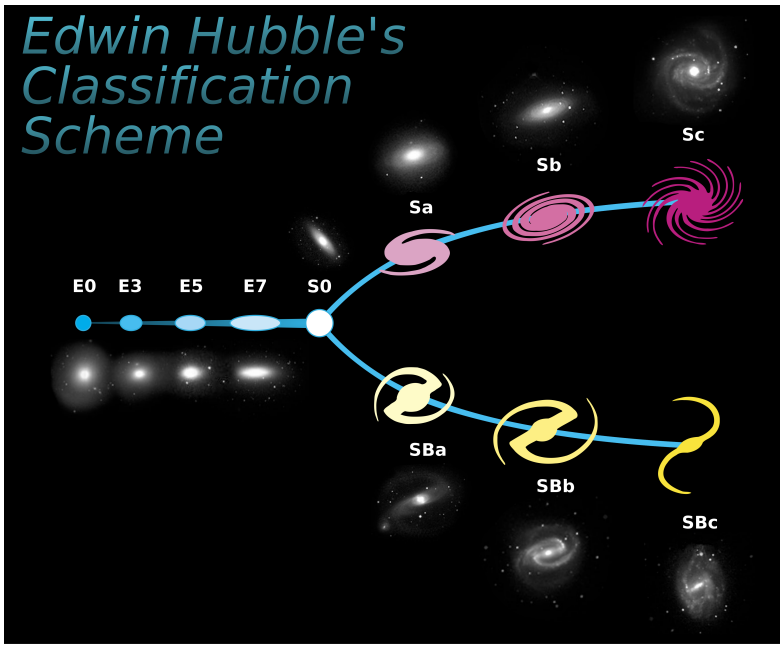

Figure 1.1: Illustration of the Hubble tuning-fork diagram. Elliptical galaxies are classified as E, lenticulars as S0, spirals as S. Spirals with bars are classified as Sb. This classification takes into account bulges and bar sizes, number of spiral arms and their apertures. Credit: NASA and ESA.

1.1.1 Formation of galaxies in Λ-CDM

The current most accepted cosmological model is the Λ-Cold Dark Matter model (Λ-CDM). It states that the Universe is made of $\sim 69\%$ of dark energy (Ω_Λ), $\sim 26\%$ of cold dark matter (Ω_m) and $\sim 5\%$ of baryonic matter (Ω_b) (Aghanim et al., 2020). This model is in agreement with most observations, such as the Cosmic Microwave Background (CMB) (Penzias & Wilson, 1965), large scale structures (Springel et al., 2006), and the expansion of the Universe (Riess, 2019). Although this is the best model we have until now, the model still cannot explain a few observations such as the number of satellites in our local Group (Mateo, 1998) and the amount of lithium in the Universe (Hou et al., 2017).

According to this model, small dark matter haloes merge to construct larger systems, and this is called the hierarchical formation of structures (White & Rees, 1978). In the context of galaxies through cosmic time, galaxies will merge and interact to form bigger galaxies and during these interactions they can can change their properties. We expect that in the early Universe there were fewer larger haloes compared to our Universe today, since the smaller haloes did not yet have enough time to merge.

Galaxies are formed by the collapse of a gas cloud due to gravitational force. When the gravitational force is larger than the internal pressure of the gas, this cloud will collapse and fragment, generating stars. Galaxies are mainly made of dark matter, stars, gas, dust, stellar remnants and a central supermassive black hole. In the context of the hierarchical structure formation, when such galaxies merge or interact, the collision will not only result in a more massive dark matter halo, but the gas will also interact, which can change the star-formation rate of the system.

1.1.2 Observed properties of galaxies

As shown in Figure 1.1, there are many types of galaxies in the Universe and they can have different shapes, colours and star-formation rates. Research has shown that there is a bimodality in galaxy properties, resulting two main sets of galaxies (Strateva et al., 2001; Blanton et al., 2003; Muzzin et al., 2012a; Wetzel et al., 2013). The analog of a colour-magnitude diagram (CMD) using stellar mass is shown in Figure 1.2 (Baldry et al., 2004; Mapelli, 2015). Early-type galaxies are often quiescent or passive galaxies, are redder, more elliptical and with lower star-formation rates compared to the other set of galaxies. These galaxies are located in the red sequence of the CMD (see Figure 1.2). Late-type galaxies are often star-forming galaxies with high star formation rates, have spiral arms and are disk dominated, these galaxies are located in the blue cloud of the CMD. There are also some galaxies that are in the middle of these two groups, they are in the CMD region called the green valley (Bell et al., 2004; Faber et al., 2007; Gonçalves et al., 2012). One of the primary goals of extragalactic research is to understand what physical processes lead to this diversity of galaxy properties, and what processes can change a galaxy's properties. Figure 1.2 shows two possible scenarios of how galaxies can change properties: the transformation of a spiral galaxy into an elliptical by quenching of star-formation or the rejuvenation scenario, in which an elliptical galaxy accretes gas from which it re-starts to form stars.

"Quenching" is the process of slowing or stopping star formation in a galaxy. This quenching process can be caused by galaxies' interactions (Gabor et al., 2010), interactions with an external medium (Roberts et al., 2019), AGN (Piotrowska et al., 2021) and stellar feedback (Chan et al., 2018), or the end of the gas supply within galaxies (Trussler et al., 2019). However, how much each process is relevant at different cosmic times is an open question and the focus of much active research.

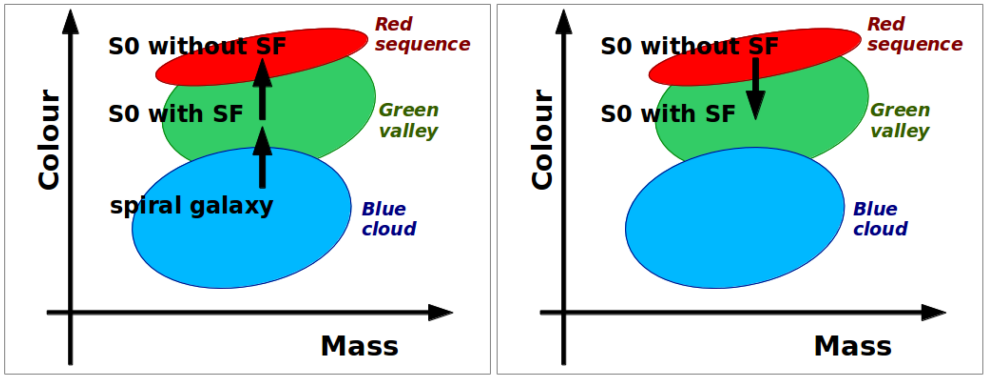

Figure 1.2: Analogous of colour-magnitude diagram. In blue is the blue cloud, in green the green valey and in red the red sequence. Figure credits: Mapelli (2015).

A useful way to quantitatively compare galaxies with different properties is to compare the luminosity function of each type of galaxy (Blanton et al., 2003; Faber et al., 2007; Wylezalek et al., 2014). The luminosity function is defined as the number of galaxies per volume in different luminosity bins. Schechter (1976) fitted a model using observed data and the equation is knows as Schechter Function, it is shown in Equation 1.1.

$$\Phi(L)dL = \Phi^* \left(\frac{L}{L^*}\right)^{\alpha} exp\left(\frac{-L}{L^*}\right)\frac{dL}{L^*} \tag{1.1}$$

$\Phi(L)$ is the luminosity function, Φ^* is a normalization parameter, α is the power slope and L^* is a characteristic galaxy luminosity. The Schechter function can also be written in terms of mass (Press & Schechter, 1974). Furthermore, luminous and massive galaxies can have very different properties compared to low mass and faint galaxies, and this may be due to different physical processes dominating the quenching of the galaxies. These are useful tools to quantitatively measure differences in galaxies, as I shall explore in Chapters 2 and 4.

1.1.3 Impact of the environment on galaxy properties

The relevance of internal and external processes to explain the observed properties of galaxies is commonly referred to as the 'nature vs nurture' debate. 'Nature' processes involve a secular process dominating the evolution of the galaxy, such as AGN (Silk & Rees, 1998) and stellar winds (Larson, 1974). This is also known as 'secular evolution' or 'mass quenching'. 'Nurture' processes are triggered by the environment where the galaxy resides, this is frequently referred to as 'environmental quenching'.

Many works since the 1930s have correlated galaxies' properties with their environment and stellar mass (Hubble & Humason, 1931; Abell, 1965; Oemler, 1974; Dressler, 1980; Poggianti et al., 2006). There are many works that prove the correlation of galaxy properties with environment at $z < 1$. These properties include colours (Balogh et al., 2004), ages (Cooper et al., 2010), morphologies (Dressler, 1980), SFRs (Gómez et al., 2003), metallicities (Cooper et al., 2010), and stellar masses (Baldry et al., 2006). Oemler (1974) found that the fraction of elliptical and lenticular galaxies increases with the mean density of the cluster while the fraction of spirals decreases. Later, Dressler (1980) found a similar result using the density around each galaxy, showing that different types of galaxies reside in different environments. In general, red ellipticals with low SFRs are found in the central regions of clusters of galaxies, which are the densest environments in the Universe. Blue spirals with high SFRs are found in the outskirts of clusters and in the field.

Of particular importance is the work of Peng et al. (2010). The authors investigated the fraction of red galaxies as a function of both mass and environment using 238,474 SDSS galaxies at $0.02 < z < 0.085$, and 10,644 zCOSMOS galaxies

at $0.1 < z < 1.4$. Peng et al. (2010) showed that the fraction of red galaxies depends on both the galaxies' masses and environment. Figure 1.3 is an extract from the paper and shows that the fraction of red galaxies increases with overdensity as well as mass. Their work shows that both environmental and mass quenching processes are relevant to explain the existence of red galaxies. A key point in their work is that the effects of stellar mass and environment are separable, i.e. do not depend on one-another. They gave the name "mass-quenching" to the processes that give rise to the correlation between galaxy colour and stellar mass, and "environment-quenching" to processes that give rise to the correlation between galaxy colour and galaxy overdensity.

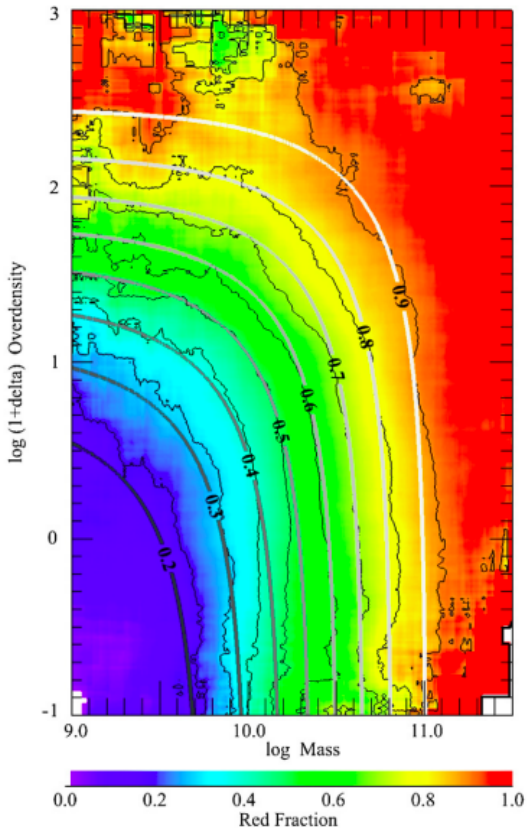

Figure 1.3: Red fraction as a function of overdensity and mass. Galaxies are from SDSS. Figure from Peng et al. (2010).

1.1.4 Mechanisms that impact star formation in galaxies

The main secular processes related to mass quenching are: the presence of a hot halo, disc instabilities, and stellar and AGN feedback, which I briefly explain here. Galaxies more massive than $\sim 10^{12} M_{\odot}$, can have a hot halo caused by shock heating of the infalling gas that turned the gravitational energy into heat (Dekel et al., 2009). The gas cools by thermal Bremstrahlung, which has a long cooling time if the gas is not dense enough. While there is this hot halo, if new gas arrives in the galaxy it is shock heated by the halo gas. During this process, the formation of stars is not possible since the gas is too hot to form stars (Birnboim & Dekel, 2003; Dekel & Birnboim, 2006). However, in some situations at high redshift ($z > 2$), cool gas can penetrate the hot halo, also known as cold streams, and provide direct cool gas to the galaxy to form stars (Dekel & Birnboim, 2006).

Very massive galaxies ($> 10^{11}\, M_{\odot}$) can have dynamical instabilities in their discs caused by streams of gas. This can cause a collapse in the rotational support of the galaxy and lead to a fast starburst phase, in which all the gas is used to form stars. After this starburst phase, the galaxy has no further gas to form new stars and so gradually becomes redder (Dekel et al., 2009).

The impact on star formation of the presence of an active galactic nucleus (AGN) in the host galaxy is actively discussed in the recent literature. Some works suggest that the presence of jets can warm the environment around the black hole and prevent star formation (Silk & Rees, 1998; Bower et al., 2006; Croton et al., 2006). However, other research found that the AGN can cause shock waves and trigger star-formation in the host galaxy (Zubovas et al., 2013). AGN feedback is more important in massive galaxies because the mass of the central black hole is correlated with the mass of the host galaxy (Li et al., 2020), and the feedback

energy from a black hole is proportional to the mass of the black hole.

Another secular mechanism is stellar feedback, which is caused by supernovae and stellar winds (Larson, 1974; White & Frenk, 1991; Diamond-Stanic et al., 2012). These two processes can heat the gas in the galaxy through shock-heating caused by winds from the massive stars and remnants. These processes have a larger impact on low mass galaxies, as the energy from the winds can be high enough to unbind the gas from low-mass galaxies.

The main environment-quenching mechanisms are: mergers, tidal interactions, ram-pressure stripping, strangulation and thermal evaporation. Mergers are caused by the collision of galaxies (Bekki, 1998; Conselice et al., 2003, 2022). If the galaxies have similar size, the collision is classified as a major merger. If one galaxy is significantly bigger than the other, it is classified as a minor merger. The merger can be described as 'wet' when there is a lot of gas present or 'dry' when there is no gas. In wet mergers a starburst can be triggered in the remnant galaxy, which results in fast gas consumption. After the starburst, there is no gas remaining and the galaxy gradually becomes redder.

Tidal interactions can occur when galaxies pass near each other, but not close enough to merge (Moore et al., 1996). This interaction can disrupt galaxies' morphologies and cause instabilities, such as tidal stripping. High speed encounters are known as galaxy harassment (Bialas et al., 2015). These encounters can induce a starburst in the galaxy. Both mergers and interactions become more important in the densest environments. In which mergers tend to be more relevant in groups since galaxies have lower velocities compared to clusters and have time to merge. In clusters, galaxies have higher velocities and other interactions tend to be more relevant. Galaxies can also interact with the gravitational potential well of the cluster (Henriksen & Byrd, 1996; Merritt, 1984). This generates tidal accelera-

tions on the galaxies and can cause collisions of gas clouds which can trigger star formation.

Ram-pressure stripping occurs when the gas within a galaxy is removed by an interaction between the interstellar medium of the galaxy and the plasma of the intracluster medium (ICM) (Gunn & Gott, 1972). The strength of this interaction depends on the velocity of the galaxy relative to the ICM, and the density of the ICM. Therefore, this process is most important in the densest regions of the most massive clusters, and not important in cluster outskirts. We also expect this process to be mass dependant, since the gravitational pull of the galaxy will counter the ram-pressure. Therefore, low-mass galaxies are expected to be more strongly influenced by this process than massive galaxies.

When this interaction between the ICM and ISM is not strong enough to remove all the gas in the galaxy, it may be strong enough to stop any further gas infalling into the galaxy. This is process is called 'strangulation' (Larson et al., 1980). In this case, the galaxy continues to form stars for a period, but at some point all the gas will be used up and no further star formation can occur. Moreover, the plasma can also interact with the galaxy in a way that it warms the galaxies' gas through shock heating (Cowie & Songaila, 1977).

Besides environment-quenching and mass-quenching, there is a third possible quenching mechanism known as 'pre-processing'. In the context of the hierarchical formation of structures, clusters reside in the densest regions of the Universe and they are constantly accreting matter, which includes groups of galaxies. Galaxies can be "pre-processed" in these groups before falling in the cluster's main halo. In this process, they lose or consume their gas inside groups or lower mass haloes while they are falling into the cluster. This consumption can be due to interactions with other galaxies in groups or other processes, such as AGN feedback and

hot haloes. Research shows that preprocessing is an important mechanism that quenches galaxies in the low redshift Universe (Haines et al., 2015; Bianconi et al., 2018), but has not yet been robustly studied at $z > 1$.

1.2 Clusters of galaxies

1.2.1 Historical introduction

The first documented observation of galaxy clusters was made by Charles Messier in 1784. He identified "nebulous objects" in the sky and noticed that some of them were grouped. In particular, he reported an overdensity of objects in the direction of the Virgo constellation – which now we know is the Virgo Cluster. William Herschel was also interested in these nebulous objects and reported an excess of nebulae in the direction of Coma, which is now known as the Coma cluster. Later, Hubble noticed that we were inside a group of galaxies and named it the "Local Group" (Hubble, 1936). Fritz Zwicky made some of the first measurements of the mass of a cluster. Using the virial theorem to estimate the mass of Coma, he found that the mass was much larger than the galaxies' masses summed (Zwicky, 1933a). The *Missing Mass Problem* was the first evidence of dark matter. In 1958, George Abell built the first large catalogue of galaxy clusters and revolutionized the field at that time (Abell, 1958). His catalogue is still broadly used today due to its quality in terms of richness estimates.

1.2.2 Definitions

Galaxy clusters are structures bound together by gravity (Voit, 2005). They are defined as groups of hundreds to thousands of galaxies. Typical masses range from

$10^{14} - 10^{15}\, M_{\odot}$ and virial radii of $1\, Mpc$. They have temperatures of $10^{7} - 10^{8}\, K$ (Mantz et al., 2017) and velocity dispersions of $500 - 1200$ km/s (Girardi et al., 1993; Lima Neto, 2016).

Galaxy clusters result from the evolution of matter overdensities through cosmic times. Due to temperature variations in the CMB observations (Fixsen et al., 1996), we know that when the Universe was young, the differences in density between different locations were small, but as the Universe got older, the contrast increased due to gravity and these structures formed. As the most massive objects in the Universe, galaxy clusters are still in the process of forming and growing.

In contemporary research, clusters are being used for both cosmological and galaxy evolution studies. As described in section 1.1.3, many works have shown that the large-scale environment of a galaxy impacts its evolution (Butcher & Oemler, 1978; Dressler, 1980; Peng et al., 2010; Costa-Duarte et al., 2018). Galaxies in denser environments have been shown to have different properties to galaxies in low density regions: cluster galaxies tend to be redder and elliptical, while field galaxies tend to be bluer. By exploring the differences between cluster and field galaxies, we can understand the physics behind the processes that impact galaxy evolution.

The growth rate of structures depends on cosmology, specifically the density of matter (Ω_m) and the variance of the density field (σ_8). Therefore, measuring the rate at which clusters grow in the Universe is a way to constrain these cosmological parameters. The primary way to do that is to measure cluster mass functions at different redshifts to measure their growth rate (Bahcall & Cen, 1992). The primary theme of this thesis concerns galaxy evolution in clusters, so I do not explore this further here. Further information on using clusters as cosmological tools can be found in Allen et al. (2011).

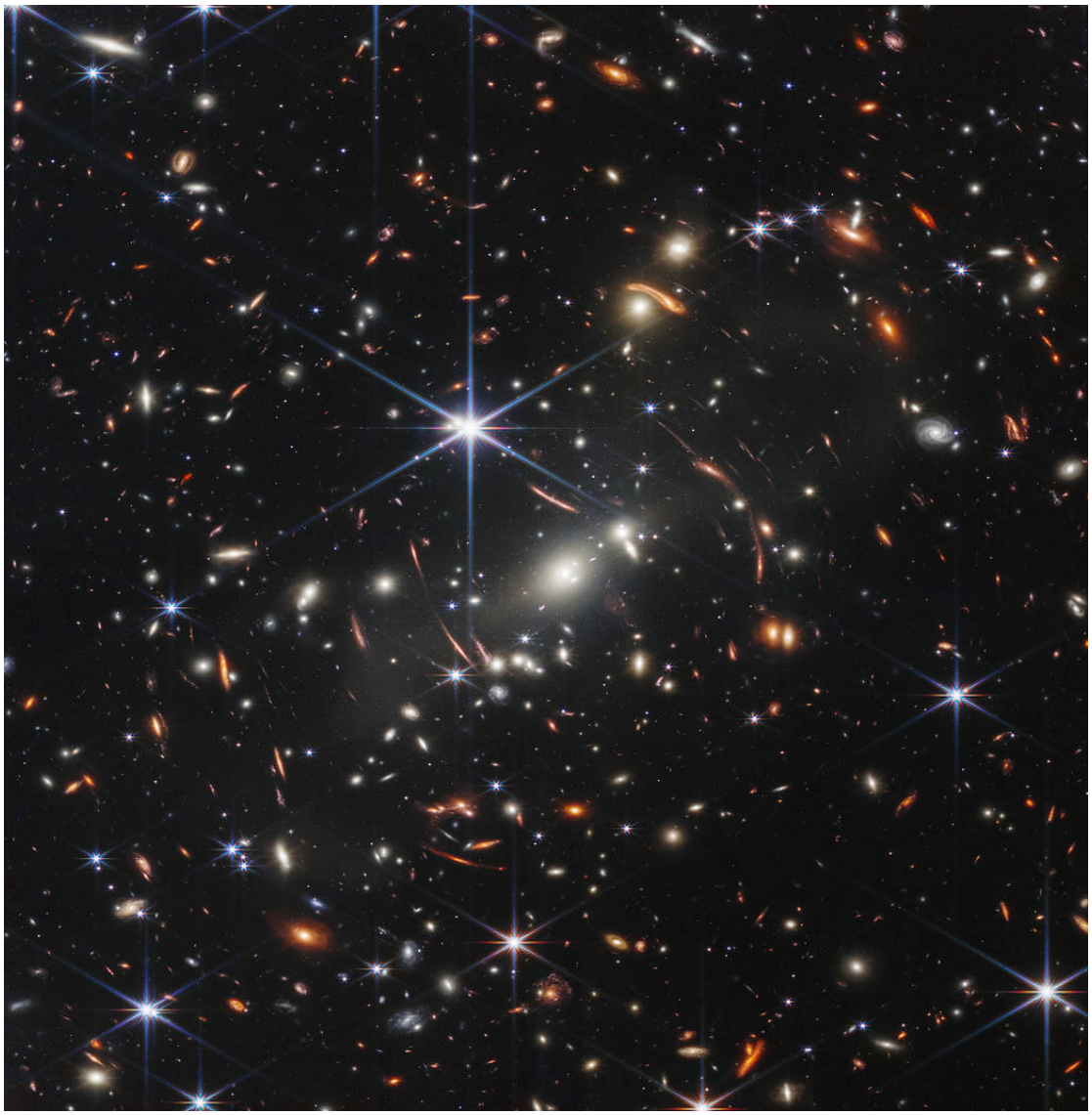

Figure 1.4: Galaxy cluster SMACS 0723 seen with JWST. In this image it is possible to see many characteristics that are typical of galaxy clusters. There is a dominant red ellipitical population in the centre. We can also see the gravitational lenses caused by the cluster mass, this is a way to measure the dark matter distribution of the cluster. In the centre, there is a giant ellipical galaxy, the brightest cluster galaxy of the cluster. Around it, there is a diffuse component that is the intracluster light. Image credit: NASA, ESA, CSA, and STScI.

1.2.3 Constituents and properties

Galaxy clusters are mainly made of dark matter, baryonic plasma, galaxies and intracluster light. Most of their mass is in the form of dark matter ($\sim 80-85\%$) and a small part in the form of baryons - $\sim 15-20\%$ (Lima Neto, 2016), of which, $\sim 13-16\%$ is a hot plasma that is called the intracluster medium and $\sim 2-3\%$ in the form of stars (Voit, 2005). These stars are mostly inside galaxies, but some of them are free-floating stars that are bound to the cluster potential.

Dark matter

The dark matter in clusters was first measured by Zwicky (Zwicky, 1933b) in 1933, when he analysed the Coma cluster. He measured the velocity of galaxies and found that they are faster than expected according to the Virial Theorem, given the total mass he observed in stars. He concluded that there must be additional matter that could not be seen.

More recently, the dark matter content of galaxy clusters has been estimated using gravitational lensing (Hoekstra et al., 2013). Clusters deform space-time as predicted by general relativity since they are a concentration of mass. The light that comes from objects in the background of the cluster can be distorted, amplified and/or appear multiple times. By measuring these distortions, it is possible to estimate the dark matter distribution within the cluster. The total amount of mass in these clusters is in excess of $10^{14}\,M_{\odot}$, which is much greater than the mass of the plasma.

Merging clusters give us important clues about the nature of dark matter: a classic example is the Bullet Cluster (Clowe et al., 2004; Markevitch et al., 2004). The Bullet Cluster is a system of two clusters that have recently passed through

one another. Their gas distribution was affected by the interaction causing the plasma in one of them to have a "bullet" shape. Most of the visible mass in clusters is in the form of plasma, and if dark matter did not exist, we would expect that the centre of mass of the Bullet Cluster system would be in the middle of the plasma distribution. However, the centre of mass measured by gravitational lensing is among the galaxies (Markevitch et al., 2004), and not in the plasma region. This fact is not easily explained by Modified Newtonian dynamics (MOND) theories. So the Bullet Cluster provides some of the strongest evidence for the existence of dark matter.

Intracluster medium

Low redshift clusters can be seen in X-rays as diffuse objects and they were first observed with the UHURU satellite (Gursky et al., 1971; Kellogg et al., 1971). The observed X-ray photons come from a hot plasma that is called the intracluster medium (ICM). We can observe the plasma due to the interaction of free electrons with the nucleus of atoms through a process known as thermal Bremsstrahlung. As an electron is accelerated around the nucleus, it emits a photon that is energetic enough to be an X-ray. Recently clusters have been observed with Chandra and XMM telescopes (Snowden et al., 2007; Santos-Lleo et al., 2009).

The presence of the plasma can also be observed in the radio, due to an effect called the Sunyaev-Zeldovich (SZ) effect (Sunyaev & Zeldovich, 1969, 1972). The light from the Cosmic Microwave Background (CMB) interacts with the electrons in the plasma within clusters and the CMB photons receive a boost of energy via inverse Compton scattering which can be observed at radio wavelengths.

This component is not possible to see in Figure 1.4, since it only emits in X-rays

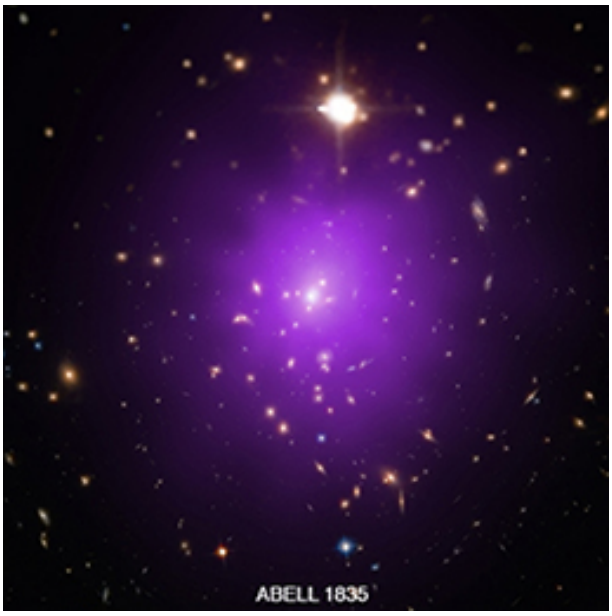

Figure 1.5: Galaxy clusters in X-rays and optical. The X-ray emission was observed by Chandra and it is shown in purple. The optical data is from the SDSS survey, in which we can see the galaxies. X-ray: NASA/CXC/Univ. of Alabama/A. Morandi et al; Optical: SDSS, NASA/STScI.

so it is not visible in the infrared or optical range of the electromagnetic spectrum shown in this image. Space telescopes that observe in X-rays, such as Chandra, XMM-Newton, and eRosita can capture the ICM of clusters. An example of a cluster observed by Chandra is shown in Figure 1.5. The plasma distribution can be seen in purple and the galaxies are shown in the SDSS image in red to blue.

Galaxies

Clusters of galaxies have hundreds to thousands of galaxies that are held together by gravity. The central regions of clusters are dominated by red elliptical galaxies and lenticulars, while spirals are more numerous in the outer regions. The impact of the cluster environment on the properties of galaxies has been discussed in section 1.1.3, and the physical mechanisms that can affect cluster galaxies was described in section 1.1.4.

Intracluster light

The intracluster light (ICL) is mainly made of stars that were stripped from galaxies during interactions between galaxies or with the tidal field of the cluster (Montes & Trujillo, 2018). The ICL fraction is defined as the ICL luminosity divided by the total luminosity of the cluster (ICL+galaxies). In low redshift clusters, the ICL fraction can reach $\sim 50\%$ of the total stellar mass of the cluster (Montes, 2019). The intracluster light component is discussed in detail in section 1.4.

1.2.4 Detection of Clusters

Clusters can be detected in many ways and in different ranges of the electromagnetic spectrum: radio, infrared, optical and X-rays. They can be found by locating the hot plasma in the intracluster medium via X-rays (Allen et al., 2011; Böhringer & Schartel, 2013; Burenin et al., 2007; Ebeling et al., 2010; Vikhlinin et al., 2006; Mehrtens et al., 2012; Takey et al., 2013, 2014, 2019; Liu et al., 2015), or in the radio due to the SZ effect (Staniszewski et al., 2009; Planck Collaboration et al., 2016; Hilton et al., 2018; Planck Collaboration et al., 2014). They can also be detected in optical/infrared wavelengths, by searching for overdensities of galaxies (Werner et al., 2022; Lopes et al., 2004; Rykoff et al., 2014; Wen et al., 2012; Durret et al., 2011).

1.3 Proto-clusters of galaxies

Galaxy proto-clusters are the progenitors of galaxy clusters. They are, therefore, collapsing structures in the high-redshift Universe that are made of dark matter,

gas and galaxies. They are dynamically young systems that span over $10-20$ cMpc and have typical masses of $10^{13}-10^{14}\,M_{\odot}$. They constitute of dark matter haloes with galaxies that are falling towards a dominant and most massive halo. A simple schematic of a galaxy proto-cluster can be seen in the right side of Figure 1.6. The dark matter distribution of proto-clusters occupy a larger volume compared to clusters and is spread across several halos, as can be seen in Figure 1.6. The illustration also shows that the galaxies' colours are expected to be different in clusters and proto-clusters and this will be discussed through this section.

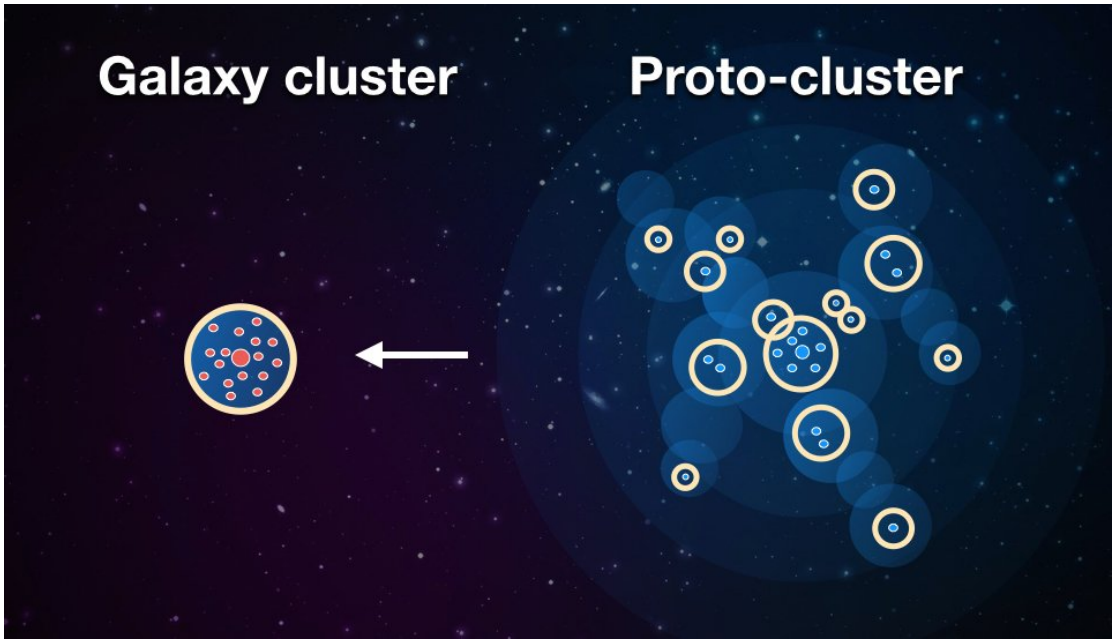

Figure 1.6: Illustration of dark matter haloes and galaxies in clusters and proto-clusters. Galaxy proto-clusters are made of several dark matter haloes, that span over ~ 10 cMpc. Credits: Yi-Kuan Chiang webpage on University of Texas Austin website (no longer available).

1.3.1 Definitions

There are different definitions of galaxy proto-clusters in the literature (see the debate in Overzier (2016)). Some works define the most massive haloes at $z > 2$

that will become clusters as proto-clusters, whilst others describe all haloes that will end up in clusters as being the proto-cluster. Therefore, one must be careful when comparing results in the literature to make sure a consistent definition is used. In this thesis, we define a proto-cluster to be all the galaxies and haloes that will end up in a cluster by $z = 0$.

Proto-clusters evolve in mass and volume over time. This is illustrated in Figure 1.7, which shows how the most massive progenitor haloes evolve in mass for different cluster masses. Statistically, the most massive systems at redshift 6 will grow to become the most massive $10^{15}\,M_{\odot}$ clusters. However, this should only be considered in a statistical sense, since cluster growth is stochastic and some of the most massive clusters today evolved from relatively low-mass haloes at $z > 2$ (Muldrew et al., 2015). The right panel shows the evolution of the effective radius with time. The most massive systems will occupy a greater volume compared to the least massive systems, independent of the cosmic time. Also, proto-clusters occupy a larger volume in the sky in early times compared to low redshift systems due to collapse. The evolution of proto-cluster properties is intrinsically related to the initial density fluctuations and their constituents.

1.3.2 Constituents and properties

Galaxy proto-clusters consist of a set of dark matter haloes containing galaxies which have been readily observed. However, the amount of plasma and ICL present in these structures is poorly constrained. In the case of the ICL, this is related to the fact that observing low surface brightness emission in high redshift structures can be challenging. The ICL is faint in general, and at high redshifts it is even fainter. This will be discussed in more detail in Section 1.4. Proto-clusters, by

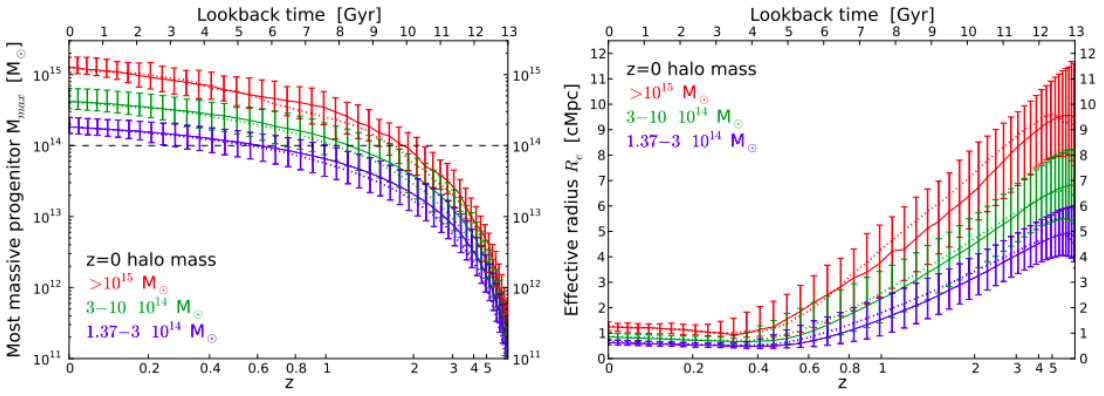

Figure 1.7: Evolution of proto-clusters' masses and radii through cosmic time. The colours relate to the halo mass at redshift 0. In red, it shows clusters with masses $> 10^{15}\,M_{\odot}$, in green $3 - 10 \times 10^{14}\,M_{\odot}$, and in blue $1.37 - 3 \times 10^{14}\,M_{\odot}$. The figure on the left shows how the mass of the most massive progenitor changes with redshift. The figure on the right shows how the proto-cluster effective radius changes with time for different final mass ranges. Credits: Chiang et al. (2013).

definition, do not have massive haloes and are still collapsing. Since the gas in clusters is heated during the gravitational collapse, the presence of an X-ray bright, hot plasma is only expected in more mature systems. The gas in proto-clusters may not be hot enough to be detected in X-rays via thermal Bremsstrahlung, so it is expected that at some point at high redshift the ICM fraction is null, but the limit of detection is still in debate.

The main component of proto-clusters that we can most easily observe are the galaxies. Recent works show that the star-formation rates in galaxies at high redshifts are larger than at lower redshifts (Madau et al., 1996; Madau & Dickinson, 2014). Since proto-clusters are at higher redshifts, it is expected therefore that their galaxies have higher levels of star formation compared to cluster galaxies. According to the hierarchical formation of structures, small galaxies will merge to build large galaxies. In early times, galaxies were less massive and in the process of formation, and we expect this formative stage in proto-clusters. This is illustrated in Figures 1.6 and 1.8. Figure 1.6 shows a simple scheme illustrating that galaxies

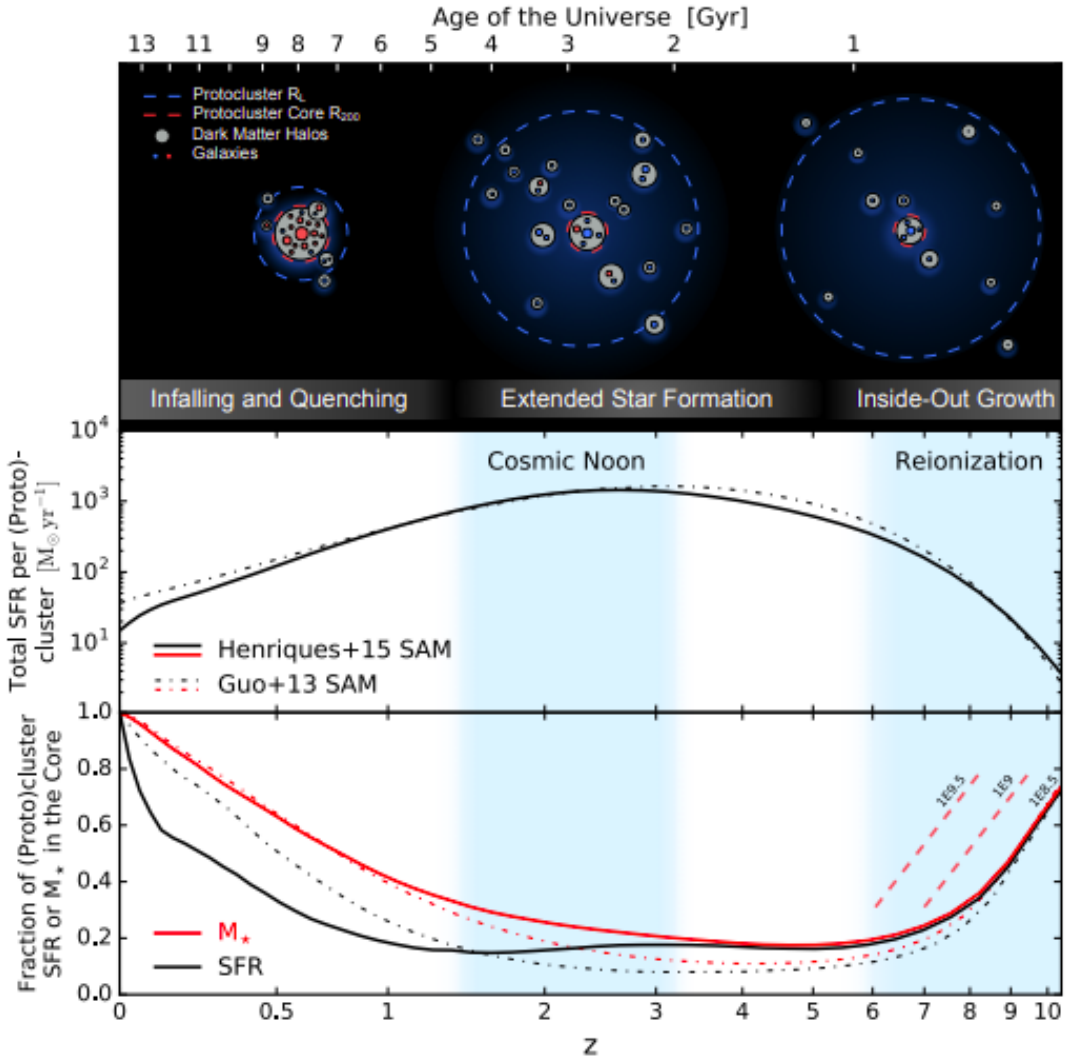

Figure 1.8: Proto-cluster star-formation rates through cosmic time. In the top panel, there are illustration of clusters in different redshifts. In the middle panel, they show the SFR per proto-cluster in different redshifts. In the bottom panel is shown the fraction of SFR and stellar mass in the main halo. The dashed lines are from Guo+13 semi-analytical model, while the standard line is from Henriques+15 semi-analytical model. In the bottom figure, in red is shown the stellar mass fraction evolution with redshift and in black the fraction of star-formation rate evolution. Credits: Chiang et al. (2017).

in high redshift proto-clusters are expected to be bluer than cluster galaxies due to having high star-formation rates (right image). Clusters are expected to have a more prominent dominant halo and with a redder and passive population. Figure 1.8 gives more details about the star-formation rates (SFRs) for different cosmic ages and the fractions of SFR and stellar mass in the main halo relative to the whole proto-cluster according to the L-galaxies SAM (Henriques et al., 2015). In this figure, we can see that at $z \sim 2$ there is a peak in the SFR in the proto-cluster galaxies that then decreases over time. At $z > 8$ most of the stellar mass and star formation is situated in the main halo as this galaxy forms first. But gradually more stellar mass is formed in other haloes. At $z \sim 2$, most of the stellar mass of the proto-cluster is expected to be in smaller haloes and not in the proto-cluster main halo as shown in the red line of Figure 1.8. The fraction of stellar mass and star-formation rate at $z \sim 2$ in the main halo is $\sim 20\%$. After $z = 2$, the proto-cluster begins to collapse rapidly and we see that the fraction of stellar mass and SF in the main halo rises. Figure 1.9 shows how the proto-cluster mass evolves with time from Muldrew et al. (2015). The dashed lines represent the total mass evolution, while the solid lines represent the cluster main halo mass evolution. The colours are related to different final masses. This figure shows that most of the mass in clusters were in smaller haloes in the past that were outside the cluster main halo. From these simulations, we see that the halo environment of proto-cluster galaxies is expected to evolve with time.

1.3.3 Star formation in proto-cluster galaxies

According to the models presented above, we expect that the SF properties of proto-cluster and cluster galaxies will change over time. This has been confirmed by some observations of high-redshift proto-clusters, which contain a predomi-

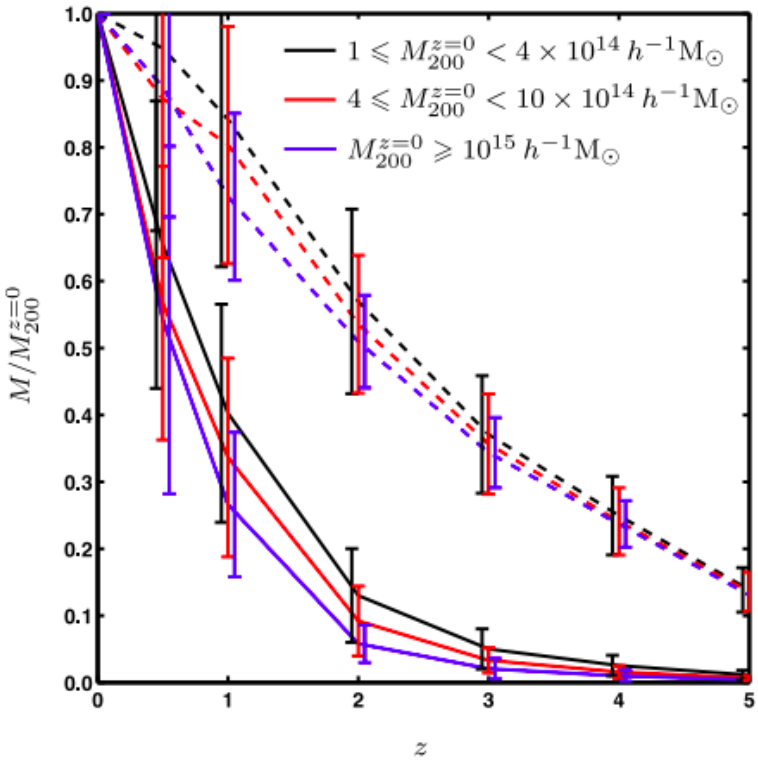

Figure 1.9: Proto-cluster mass evolution with redshift. Different colours are related to different final masses. The solid lines are the mass evolution of the proto-clusters main haloes and the dashed lines are the mass evolution of the total mass taking into account all the haloes that will form the final cluster. Credits: Muldrew et al. (2015).

nantly star-forming galaxy population (Chiang et al., 2017) and proto-clusters containing an excess of submm-bright galaxies (Casey, 2016), which are not present in low-redshift clusters. Hence whatever processes act to quench SF in clusters does not have as strong an influence in proto-clusters. Further evidence that SF quenching behaves differently in clusters and proto-clusters comes from van der Burg et al. (2020) who showed that the fraction of quenched galaxies (QFE) in high redshift clusters depends on stellar mass - which is not seen in low redshift clusters (this can be seen in Figure 1.10). The fact that at low redshifts, the quenching process does not depend on stellar mass, and that at high redshifts it is dependent on stellar mass, suggests that the main physical processes that quench

galaxies in high and low redshift clusters are different. van der Burg et al. (2018) estimating the QFE within 1 Mpc found a significant amount of quenched galaxies, giving a hint that some of the galaxies were quenched outside the cluster main halo, which means that pre-processing would be relevant at high redshifts. This agrees with what is expected by the hierarchical formation of structures, in which we expect more groups falling in the main halo at high redshifts.

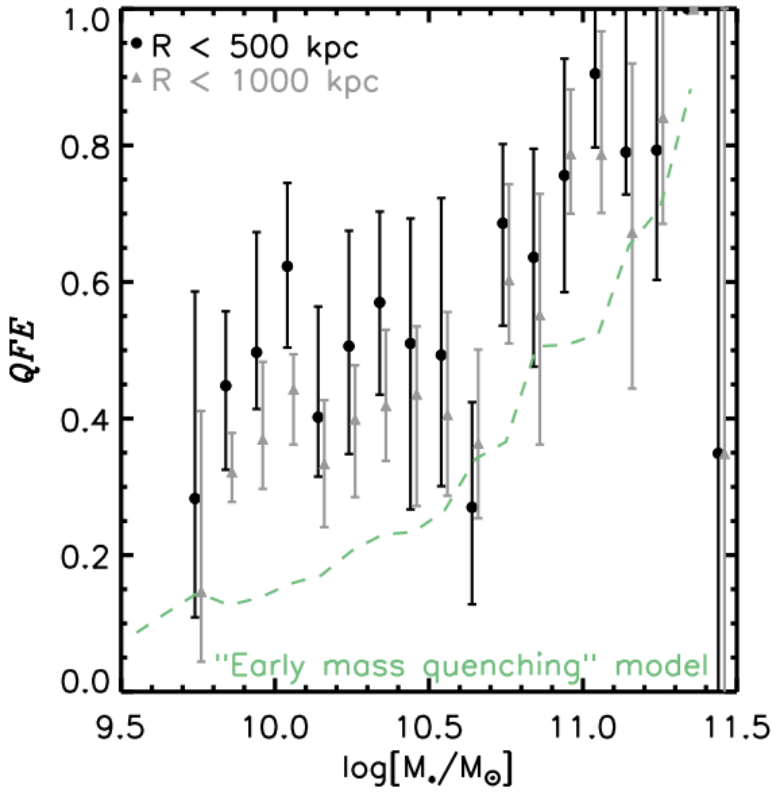

Figure 1.10: Quenched fraction excess as a funtion of stellar mass for clusters at high redshifts. The black dots represent cluster galaxies inside 500 *kpc* and the grey dots inside 1000 *kpc*. Credits: van der Burg et al. (2020).

Many of the massive galaxies in clusters and proto-clusters have already quenched so it is difficult to observe a difference in the quenched fraction. However, galaxies' ages can give us important clues on which galaxies formed first: field or cluster galaxies. Ages can be estimated by fitting stellar population models to photometric or spectroscopic data (Lee-Brown et al., 2017; Webb et al.,

2020; Rakos et al., 2007; Rettura et al., 2010; Gobat et al., 2008). One way to estimate the galaxy's age is to fit stellar templates, such as Bruzual & Charlot (2003a), to the data. By doing that, it is possible to find the most relevant stellar populations for the galaxy and with that estimate its age.

Alternatively, spectral features such as the $D_n 4000$ and Balmer breaks (Lee-Brown et al., 2017) can be used as proxies for a galaxy's age. The first break is caused by the presence of ionized metals in the atmosphere of stars: a break is caused because these metals absorb the light blueward of ~ 4000. The second one is caused by a hydrogen transition in which a free electron absorbs a photon and goes to the second orbital. This effect is particularly strong in A type stars, so the presence of this break is related to the existence of A stars in the galaxy. Due to the presence of metals and A stars, these breaks are related to a quenched galaxy population, i.e galaxies with few O and B-type stars.

The comparison of the stellar ages of cluster and field ages have not reached a conclusion on one hand. Rakos et al. (2007) estimated the ages of galaxies in A1185 and Coma and found that galaxies in the central regions of the clusters are older than galaxies in the outskirts of the clusters. This is similar to a study of a cluster at $z \sim 1.2$ by Gobat et al. (2008), who found that galaxies in clusters with $< 10^{11}\, M_{\odot}$ formed 0.5 Gyr before field galaxies. However, Lee-Brown et al. (2017) found no correlation between $D_n 4000$ and stellar mass for galaxies in a cluster at $z \sim 1.62$, and Webb et al. (2020) estimating the SFHs for 11 clusters at $z > 1.0$, found that galaxies in the field were only a few hundred Myrs older than cluster galaxies. We shall explore this topic further in chapters 2 and 4.

1.4 Intracluster Light

The ICL consists mainly of free-floating stars that are not bound to any galaxy, but rather are dominated by the potential of the cluster halo. It appears as a faint and diffuse component in the central region of galaxy clusters. Figure 1.11 shows the ICL in Abell S1063 seen with *HST*. In general, as mentioned in Montes (2022), this light is concentrated around the giant central galaxy of the cluster and can have different shapes, including substructures. The formation and growth of the ICL is a complex open question that is still hotly debated in the literature.

1.4.1 Definition

Theoretically, the ICL is defined as consisting of stars and their remnants, such as nebulae and black holes, that are not gravitationally bound to galaxies. Instead, these objects are bound to the cluster's potential. However, observationally, ICL can be defined and measured in different ways, as illustrated in Figure 1.12 (reproduced from Montes (2022)). Because the ICL definition varies in the literature, this can lead to different results and inconsistencies in its observed properties and evolution in different studies.

The physical processes that can result in the ejection of stars from galaxies include mergers (Krick & Bernstein, 2007; Lidman et al., 2013), galaxy stripping (DeMaio et al., 2017) and disruption of dwarf galaxies (Jiménez-Teja et al., 2019). Besides ejections, in-situ formation of intracluster stars can also occur (Puchwein et al., 2010). Although simulations suggest that this is the least relevant process in low redshift clusters (DeMaio et al., 2015), this has been observed in a high-redshift proto-cluster (Hatch et al., 2008). Furthermore, the stars that end up in the ICL may be stripped from galaxies somewhere else than in the cluster, such as when

Figure 1.11: Intracluster light of cluster Abell S1063 seen with HST. The intracluster light distribution around the most massive galaxy is shown in blue. The image also shows the light of background galaxies being deformed by the cluster potential. Credits: NASA, ESA, and M. Montes (University of New South Wales, Sydney, Australia).

the galaxies reside in a low-mass group, accreted later by the cluster. When stars joint the ICL through this process, it is called "pre-processing". It is plausible that several processes contribute to the ICL assembly, and it is possible that different physical processes cominate the ICL mass assembly at different cosmic ages.

From an observational point of view, the ICL is seen as a diffuse component centred around the brightest cluster galaxy (BCG), as can be seen in blue in Figure 1.11. Unlike simulations, what we see in observations is a 2D projection of the true stellar distribution and its detection has several observational issues.

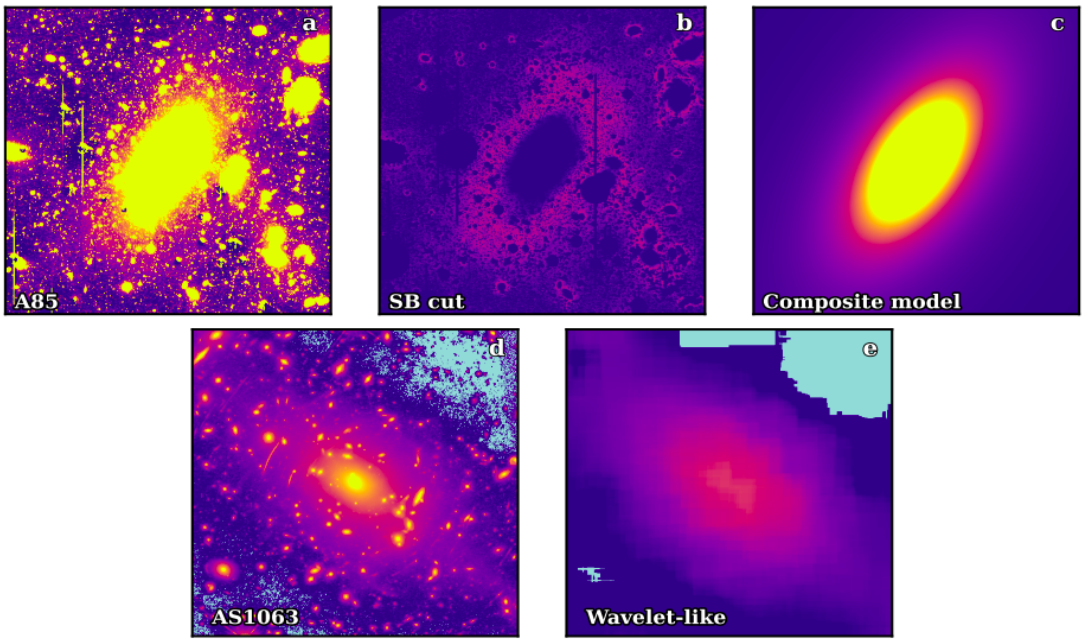

Figure 1.12: Different ICL definitions. Image from Montes (2022).

The first observational obstacle is the detection itself. This diffuse component is extremely faint. Its surface brightness can be fainter than 1% of the night-sky brightness (Guennou, L. et al., 2012). This means that careful image processing is an important step when it comes to studying ICL, since an inattentive sky subtraction can lead to incorrect results (Krick et al., 2012).

Another obstacle is projection effects, as part of the ICL can be lost due to the

presence of cluster galaxies or foreground galaxies along the line-of-sight. These objects must be masked or modelled and removed before estimating the ICL luminosity. However, masking galaxies is not a trivial task, since you will have to define the edges of the galaxies. This process can overestimate or underestimate the amount of ICL measured. An alternative to masking is to choose a surface brightness limit and separate bright objects from low-surface brightness emission (as shown in panel b of Figure 1.12).

The interactions of galaxies between each other and with the cluster not only build up the ICL, but also influence the formation of the BCG as it grows by accreting galaxies (Mihos et al., 2005; Gonzalez et al., 2005). To fully understand BCG evolution, it is necessary to take into account the ICL component.

This leads to another obstacle: how to separate the ICL from the BCG. When we observe the system BCG+ICL, it is not clear where the BCG ends and where the ICL starts. A common way to approach this issue is using a surface brightness cut, as shown in panel b of Figure 1.12. However, this method can make comparisons between studies challenging since studies can use different bands, depths and cuts to separate ICL from the BCG. Alternatively, some works fit two or more radial surface brightness profiles to the BCG and ICL to estimate the amount of light in each component. This method is also called "composite model" and it is shown in panel c of Figure 1.12 and Figure 1.13. The issue with this technique is that is does not take into account substructures when they are present. More recent approaches include wavelet-like methods (Ellien et al., 2021), as shown in panel e of Figure 1.12. In general, the dividing line between the BCG and ICL components is subjective, and so works using any of these methods will return different ICL fractions. With this in mind, many works treat the ICL+BCG as one component and do any analysis considering the light coming from both com-

ponents (e.g. DeMaio et al., 2020a).

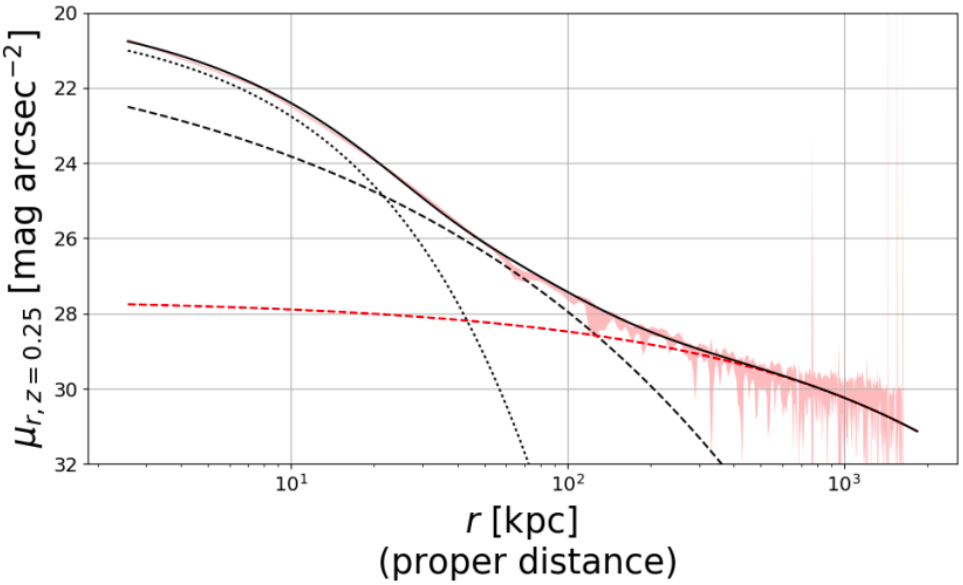

Figure 1.13: Surface brightness profile of ICL+BCG. The solid line represents the surface brightness profile of the system. The dotted and dashed lines are three Sérsic components. Credits: (Zhang et al., 2019).

Free-floating planetary nebulae and globular clusters can be used in low redshift clusters to study the kinematics of the ICL (Arnaboldi et al., 1996; Harris et al., 2020). These kinematics studies show that ICL stars are connected to the cluster dark matter halo and not to the BCG. However, this data is not available for clusters at high redshifts so this analysis can not be done yet.

1.4.2 The relation between ICL and its host cluster

The ICL fraction, defined as the fraction of stellar luminosity within the ICL component, can reach $\sim 50\%$ of the total optical luminosity of the cluster, but this value may depend on the cluster's redshift and mass. This possible dependence is hotly debated in the literature. Montes (2022) shows that clusters of $\sim 10^{14}\,M_{\odot}$ have an increase of ICL with time, so that there is almost none at $z \sim 1$ and

increases to 40% at $z \sim 0$. In the same paper, she shows that the ICL fraction can vary from almost none to 20% within simulations for the same redshift range and mass. Using observations, Montes (2022) argues that there is no correlation between the cluster mass and ICL fraction, but rather there is a correlation between the ICL fraction and the dynamical state of the system, in which more mature structures have a higher fraction of ICL. Jimé nez-Teja et al. (2018) showed that the ICL fraction is higher for merging clusters when compared to more dynamically mature systems. They also found that the ICL population in merging clusters are younger, they assume that this population of stars arrived there from galaxies during the merger event. Some simulation studies agree with this observational result (Dolag et al., 2010; Contini et al., 2018). On the other hand, these results are contradicted by other simulations that found increasing (Murante et al., 2004; Purcell et al., 2007) or decreasing trends of ICL fraction with mass (Cui et al., 2013). It is inconclusive whether there is a correlation of ICL fraction and cluster mass.

An interesting new development is the work of Montes (2019) which shows that the ICL can trace dark matter. Theoretically this is possible because the ICL is made of free-floating stars that are not connected to galaxies, but instead they are bound to the cluster due to gravity and their dynamics are dominated by the dark matter distribution. So the ICL can be used to study cluster assembly and dark matter.

1.4.3 Stellar properties

The stellar populations present in the ICL can give clues about how and when the ICL was formed as different physical processes build the ICL in different ways.

Therefore, identifying the types of stars within the ICL allows us to constrain the most relevant mechanisms in the formation and evolution of the ICL. The typical tracer used is the ICL colour, which reveals the stellar metallicities and ages.

Melnick et al. (2012) and Iodice et al. (2017) found that the ICL gets bluer with increasing radii from the BCG. Furthermore, there is evidence that the ICL colour is similar to the mean colour of the satellite galaxies. The cause of this correlation is debated in the literature but it might be related to the fact that part of the ICL was formed due to the stripping of satellite galaxies (Montes, 2022).

The ages of the ICL stellar population vary with different redshift and the dynamical state of the cluster. For low redshifts, in general, the ICL consists of an old stellar population, which indicates a secular evolution (Williams et al., 2007; Coccato et al., 2010). However, the BCG is 2-6 Gyr older than the ICL for clusters at $0.3 < z < 0.6$, meaning that the ICL was formed more recently than the BCG (Adami et al., 2016; Montes & Trujillo, 2017). Furthermore, merging clusters, which are dynamically immature, have bluer ICL than relaxed clusters (Jimé nez-Teja et al., 2018). These results show that the varying formation paths of clusters can result in different ICL properties.

1.4.4 Simulated ICL

The measurement of the ICL is a way to test models of galaxy evolution, as the formation of the ICL is a result of inefficient galaxy interactions. There are several attempts to model the formation of ICL, and most models predict a negligible amount of ICL at $z > 1.0$ (Contini et al., 2019). As a result of this, ICL in the high redshift Universe has not been explored ($z > 2.0$).

Contini et al. (2019) used N-body simulations with semi-analytical models of galaxy formation to explore the main physical processes that can form ICL: mergers and tidal stripping. Mergers would lead to no gradient in the ICL colour and metallicity, while stripping would form a system with gradients in these properties. Using simulations, they found a gradient in colour and metallicity, concluding that stellar stripping and violent relaxation are the most relevant processes to form ICL for $z < 1.0$.

1.4.5 Open questions

There are several open questions regarding ICL in clusters and proto-clusters of galaxies. In this thesis, I explore three main questions:

- When was the ICL first formed? In the literature, most observational studies observe ICL up to $z \sim 1.0$ only (Montes, 2022). However, it is not clear which is the maximum redshift that we can find it. Simulations suggest the ICL fraction above this redshift is minimal, therefore a measure of ICL at $z > 1$ would be a strong test of simulations.

- Can ICL be used to find high redshift proto-clusters? The ICL is associated to the dark matter halo of the cluster, and this is a clear sign of a massive halo. Hence, the detection of ICL at high redshifts can provide a new way to identify massive haloes in the distant Universe. This would be particularly useful for future surveys when only photometry is available to locate clusters, such as in Euclid and LSST.

- How do ICL observations compare to simulations at high redshift? It is not clear whether simulation predictions agree with observations at high

redshifts. This is caused by the fact that there are not measurements of ICL at $z > 2$, until the present moment. Also, most simulations only extend until $z \sim 1$. This comparison is important to test how well galaxy evolution models compare with observations.

Future surveys and telescopes, such as Euclid and Vera Rubin, will be useful for investigating more details about the ICL formation and evolution. JWST will have data that is deep enough in infrared filters to explore ICL in higher redshifts as demonstrated by Figure 1.14 which shows the ICL of SMACS 0723 at $z = 0.39$ seen with JWST.

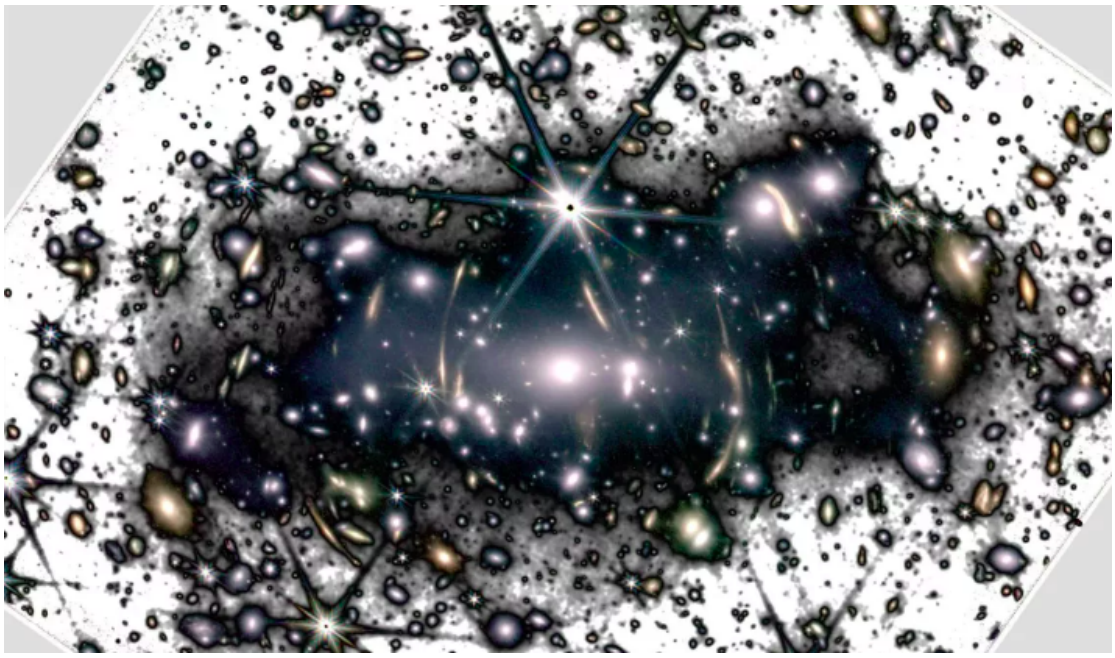

Figure 1.14: Intracluster light of SMACS 0723 seen with *JWST*. We can see a diffuse component around the brightest cluster galaxy. Image from Montes (2022).

1.5 Thesis format and outline

In this thesis, I will explore the properties of galaxy proto-clusters at $z > 1.0$. In particular, I use stellar mass functions and stellar luminosity functions to compare galaxies in different environments. The results of this work is shown in Chapters 2 and 4. I also measure the ICL around the central galaxies of proto-clusters and compare with models in Chapter 3.

The relevance of galaxy pre-processing at $z \sim 1.0$ was not estimated until now. So in Chapter 2, I want to answer the question: is pre-processing important in high redshift clusters? In this Chapter, I quantify the importance of pre-processing and environmental quenching. In section 2.1, I briefly introduce the topic and questions I want to answer. The data used in described in section 2.2. We separate galaxies according to their location: the cluster main halo, infall region and field, and the definitions of these environments are presented in section 2.2. In section 2.3, I show the results of this work using stellar mass functions, quiescent fractions and halo properties of massive galaxies in infall and field. Robustness tests are discussed in section 2.4. The implications of our findings are discussed in section 2.5. The summary and conclusion are presented in section 2.6.

In Chapter 3, I want to answer the question: is ICL present in galaxy proto-clusters? The detection of copious amounts of ICL in two proto-clusters at $z \sim 2$ is reported in this Chapter. In section 3.2, I describe the available data on these two proto-clusters and I describe in detail how the sky was subtracted from the images. How the ICL is measured in each proto-cluster is described in section 3.3. The ICL luminosities, masses and BCGs surface brightness profiles are shown in section 3.4. In the same section, we discuss the comparison of observations to the Hydrangea hydrodynamical galaxy cluster simulations, and argue that ICL is a

generic feature of $z \sim 2$ proto-clusters. In section 3.5, we discuss robustness tests that were done to check the results. There is a discussion about the results in section 3.6 and conclusion in section 3.7.

The third question I want to answer in this thesis is: when do the properties of proto-cluster galaxies and field start to differ? To answer this question, I partially extended the work done in Chapters 2 and 3 to 20 spectroscopically confirmed galaxy proto-clusters, the results are presented in Chapter 4. The grism data of these 20 proto-clusters are described in section 4.2. In section 4.3, I show how the redshifts and emission lines were estimated, I classify galaxies between member and field, I remove poor spectra, and estimate luminosity functions. In section 4.4 I present the proto-clusters and field luminosity functions and D_n4000 estimates to explore whether there are any differences in their properties. A discussion is done in section 4.5

In Chapter 5, I conclude what I found in the three projects described in Chapters 2, 3 and 4, and explain how this thesis has increased our understanding of galaxy evolution in proto-clusters.

Chapter 2

Satellite quenching was not important for z∼1 clusters: most quenching occurred during infall.

The content of this chapter has been published in (Werner et al., 2021), by Monthly Notices of the Royal Astronomical Society, Volume 510, Issue 1, February 2022, Pages 674–686. The authors of this work are S. V. Werner, N. A. Hatch, A. Muzzin, R. F. J. van der Burg, M. L. Balogh, G. Rudnick, G. Wilson.

2.1 Introduction

The presence of galaxy clusters at $z > 1.5$ that host quiescent galaxies with old stellar populations (e.g. Rudnick et al., 2012; Newman et al., 2014; Cooke et al., 2016; Nantais et al., 2016; Strazzullo et al., 2019) poses a challenge to our understanding of environmental quenching. It has long been recognised that galaxy colours (Balogh et al., 2004), ages (Cooper et al., 2010), morphologies (Dressler,

1980) and star-formation rates (SFRs) (Gómez et al., 2003) correlate with environment. Environmental quenching is an all-encompassing term used to describe any process that can cause these correlations by quenching star formation in a manner whose efficiency scales with galaxy density (Peng et al., 2010). Studies of local clusters have revealed several processes that may be responsible for this quenching: gas starvation, strangulation, ram-pressure, harassment, mergers and tidal stripping (Gunn & Gott, 1972; Dressler et al., 1997; Moore et al., 1996).

Clusters of galaxies, as hosts to hundreds of satellite galaxies, are the best places to investigate environmental quenching of satellite galaxies. An estimate of the timescale for satellite quenching comes from the SFRs of star-forming galaxies within clusters: cluster galaxies obey a similar SFR – stellar mass relation as non-cluster galaxies (Muzzin et al., 2012b; Old et al., 2021), therefore environmental quenching likely follows a delayed-then-rapid quenching timescale (Wetzel et al., 2013). In this theory cluster galaxies continue to form stars for a 'delay' time after falling into the cluster, but then quench so rapidly that few galaxies are observed in the quenching phase.

Wetzel et al. (2013) used the fraction of quenched galaxies in local clusters to estimate this delayed-then-rapid timescale, arriving at a value of $2-6$ Gyr, a value also corroborated by Fossati et al. (2017) based on modelling quenched fractions in 3DHST. Hence the presence of mature clusters at $z > 1.5$, less than 4.5 Gyr after the Big Bang, implies that this quenching timescale is likely to evolve. Assuming that infalling pre-cluster galaxies and field galaxies have similar quiescent fractions, Balogh et al. (2016) derived quenching timescales of 1.7 Gyr for $z = 1$ clusters, and Foltz et al. (2018) extends this to $z = 1.6$ to derive even shorter timescales of 1.1 Gyr. In all of these studies the quenching timescale has a mass dependency, with the most massive galaxies quenching quicker than the lower mass galaxies.

The high quenched fractions in $z \simeq 1$ clusters (Newman et al., 2014; Cooke et al., 2016; van der Burg et al., 2020), with their implied short quenching timescales, have important consequences for the predicted stellar ages of the quiescent cluster galaxies. If the high quenched galaxy fraction is caused primarily by assembly bias – where galaxy formation started earlier in the proto-cluster compared to the field – then the stellar ages of the quiescent cluster galaxies at $z \simeq 1$ are predicted to be approximately a Gyr older than coeval field galaxies (van der Burg et al., 2020; Webb et al., 2020). On the other hand, if the high quiescent fraction was caused by rapid environmental quenching of infalling star-forming galaxies then the average stellar age of the quenched cluster galaxies is predicted to be 1.5 Gyrs younger than coeval quiescent field galaxies (Webb et al., 2020), which quench over longer timescales.

It is the age dating studies of Gobat et al. (2008); Rettura et al. (2010); Lee-Brown et al. (2017); Webb et al. (2020) that causes a conundrum for mature high-redshift clusters, since $z \sim 1$ cluster galaxies are only marginally older than field quiescent galaxies. The stellar age difference is not large enough to account for the excess of quenched galaxies through assembly bias, but environmental quenching cannot be the dominant quenching mechanism since the derived short environmental quenching timescales are in direct contradiction to the older stellar ages of the cluster quiescent galaxies. Cluster-to-cluster variation cannot reconcile this problem as in some cases these contradicting results have been derived using the same clusters (c.f. van der Burg et al., 2020; Webb et al., 2020).

In this study we address this apparent contradiction by exploring one of the underlying assumptions made when deriving the environmental satellite quenching timescales: that galaxies which fall into clusters have similar properties to 'field' galaxies. Quenching timescales are usually calculated from the fraction of excess

quenched galaxies in clusters with respect to a control field, i.e. galaxies outside clusters or galaxies in the lowest density region of a survey. There are two reasons why this assumption may be unsound:

(i) The infalling galaxies may be 'pre-processed' by other environmental influences before they fall into the cluster. The standard cosmological paradigm predicts that galaxy clusters form hierarchically. Small groups form first in the early Universe, which then merge into progressively larger systems. So, before galaxies become satellites of a cluster they may travel through the modestly dense environments of groups and filaments (De Lucia et al., 2012), which may quench or alter the properties of the galaxies. This type of pre-processing is most commonly thought to act on galaxies which are satellites of another halo before they fall into the cluster. The prevalence of pre-processing at $z < 0.8$ has been established by numerous observations of quenching and morphological galaxy transformations occurring out to several virial radii of massive clusters (e.g. Lewis et al., 2002; Gómez et al., 2003; Patel et al., 2011; Oemler et al., 2013; Haines et al., 2015; Bianconi et al., 2018; Just et al., 2019), and probing the large scale structures around clusters for evidence of the effect of pre-processing and quenching has a long history (e.g. Kodama et al., 2004; Tanaka et al., 2006; Koyama et al., 2011). There is also tentative evidence that pre-processing occurs even at $z \sim 1.5$ (Nantais et al., 2016).

(ii) The progenitors of cluster galaxies form in proto-clusters: an environment that was several times denser than the mean density of the Universe (Chiang et al., 2013). This proto-cluster environment may alter the distributions of several properties of its member galaxies. Simulations predict that proto-cluster galaxies have a top heavy galaxy stellar mass function, started forming stars earlier, and are hosted by haloes that also have a top-heavy mass distribution (Chiang et al., 2017;

Muldrew et al., 2018). There is some observational evidence from $z > 2$ proto-clusters to back up these predictions (Cooke et al., 2014; Willis et al., 2020a), and high and intermediatery density environments at high-redshift appear to accelerate galaxy growth (Sobral et al., 2011; Hatch et al., 2011). Therefore, a higher fraction of proto-cluster galaxies may be quenched compared to field galaxies, even if they are centrals of their own haloes.

The aim of this work is to determine whether the galaxies in the infall region of $0.8 < z < 1.4$ clusters have similar masses and quenched fractions as field galaxies. If they differ, we will examine how this difference affects the determination of the environmental quenching efficiency, and whether pre-processing or biased galaxy formation in the infall region can resolve the discrepancy between the old stellar ages and the apparent rapid quenching times of massive galaxies in high-redshift clusters.

In Section 2.3 we introduce the $0.8 < z < 1.4$ clusters we use in this work and describe how we select infall, cluster and control galaxies from the data. In Section 2.4, we compare infall galaxies to cluster galaxies and control galaxies at the same redshift. We furthermore investigate the halo environment of the infall and control region by measuring the distribution of satellite galaxies around massive control and infall galaxies. We discuss our findings in Section 2.5 and outline our conclusions in Section 2.6. We use AB magnitudes throughout and a ΛCDM flat cosmology with $\Omega_M = 0.3$, $\Omega_\Lambda = 0.70$ and $H_0 = 70\,\mathrm{km\,s^{-1}\ Mpc^{-1}}$.

Name	RA (J2000)	Dec (J2000)	Redshift	σ (km/s)	R_{200} (Mpc)
SpARCS0034	8.675	-43.132	0.867	700	0.58
SpARCS0036	9.188	-44.181	0.869	750	1.06
SpARCS1613	243.311	56.825	0.871	1350	1.54
SpARCS1047	161.889	57.687	0.956	660	0.91
SpARCS0215	33.850	-3.726	1.004	640	0.88
SpARCS1051	162.797	58.301	1.035	689	0.84
SPT0546	86.640	-53.761	1.067	977	1.15
SPT2106	316.519	-58.741	1.131	1055	1.21
SpARCS1616	244.172	55.753	1.156	782	0.92
SpARCS1634	248.654	40.364	1.177	715	0.85
SpARCS1638	249.715	40.645	1.196	564	0.73
SPT0205	31.451	-58.480	1.323	678	0.85
SpARCS0219	34.931	-5.525	1.325	810	0.9*
SpARCS0035	8.957	-43.207	1.335	840	0.90
SpARCS0335	53.765	-29.482	1.368	542	0.69

Table 2.1: The 15 clusters from the GOGREEN and GCLASS samples that are used in this work. Column 4 provides the redshift of the cluster. Columns 5 and 6 provide the intrinsic velocity dispersion and radius in proper Mpc from Biviano et al. (2021), except for the cluster marked with * where we estimated the radius from σ provided by GOGREEN DR1.

2.2 Data and samples

2.2.1 The GOGREEN and GCLASS cluster surveys

We use data from the first public data release (DR1) of the Gemini Observations of Galaxies in Rich Early ENvironments (GOGREEN) and Gemini CLuster Astrophysics Spectroscopic Survey (GCLASS) surveys[1] (Muzzin et al., 2012b; Balogh et al., 2017, 2021), which contains photometric and spectroscopic data for 26 clusters and groups with redshifts between 0.85 and 1.50, and masses of at

[1]http://gogreensurvey.ca/data-releases/data-packages/gogreen-and-gclass-first-data-release

least $M_{200} \sim 10^{13} M_{\odot}$. Three of these clusters were discovered using the Sunyaev-Zeldovich effect (Sunyaev & Zeldovich, 1970) with the South Pole Telescope (SPT) (Foley et al., 2011; Stalder et al., 2013; Sifón et al., 2016), whilst 14 were discovered using the red-sequence galaxy selection method as part of the Spitzer Adaptation of the Red-Sequence Cluster Survey (SpARCS; Wilson et al. 2009a,b; Muzzin et al. 2009), and nine groups in the COSMOS field were selected based on diffuse X-ray emission implying a well established intragroup medium (Finoguenov et al., 2010, 2007; George et al., 2011).

In this work, we only use the most massive clusters in the sample with intrinsic velocity dispersions $\sigma > 500$km/s, which have dynamical masses of $> 10^{14}$M$_{\odot}$. We make this selection because the size of the infall region of high-redshift clusters depends on the $z = 0$ mass of the cluster (Muldrew et al., 2015), which correlates with cluster mass at the observed redshift. ΛCDM predicts that only 30% of today's cluster galaxies resided in the central cluster at z∼1; the vast majority of galaxies lived around the cluster in a region that we refer to as the infall region (Muldrew et al., 2015). The most massive clusters today, of $M_{z=0} > 10^{15}$ M$_{\odot}$, had infall volumes that stretched out over a radial distance of $3-4$ Mpc at $z = 1$. The infall radii of more typical $M_{z=0} \sim 10^{14}$ M$_{\odot}$ clusters only extended $1.5-2.5$ Mpc at $z = 1$ (Muldrew et al., 2015). Since we wish to select the galaxy sample that will accrete onto the cluster by the present day, we select only the most massive $z = 1$ clusters that are expected to have large infall surroundings. We list the 15 clusters used in this work in Table 2.1.

The GOGREEN photometric catalogues contain deep photometry from u to 4.5μm wavelengths. Descriptions of the photometric data and the image processing are described in van der Burg et al. (2013), van der Burg et al. (2020) and Balogh et al. (2021). Accurate relative colour measurements were obtained for

each source by van der Burg et al. (2020) using PSF-homogenised image stacks. These colours are used to identify stars using uJK colour criteria and we use the 'star' classification included in the data release and remove all sources classified as `star = 1`.

The DR1 photometric redshifts and rest-frame $U-V$, $V-J$ colours were estimated by van der Burg et al. (2020) using the `EAZY` code (Version May 2015; Brammer et al. (2008)), by fitting the photometry to spectral energy distribution (SED) templates from the PEGASE model library (Fioc & Rocca-Volmerange, 1997) with an additional red galaxy template from Maraston (2005). The photometric redshift uncertainty for galaxies with stellar masses greater than $10^{10}\mathrm{M}_{\odot}$ is $0.048(1+z)$ with 4.1% outliers.

Galaxy stellar masses provided by DR1 were obtained by fitting the photometry with stellar population synthesis models from Bruzual & Charlot (2003a) using the FAST code (Kriek et al., 2018), assuming solar metallicity, the Chabrier (2003a) initial mass function and using the Calzetti et al. (2000) dust law. The star-formation history of these models were limited to exponentially declining functions, which are known to underestimate the stellar mass by up to 0.3 dex compared to non-paramaterised models (Leja et al., 2019). Throughout this work we limit our analysis to galaxies with stellar masses $> 10^{10} M_{\odot}$, which is the 80% completeness limit as determined by van der Burg et al. (2020). Following Williams et al. (2009) we used the rest-frame $U-V$, $V-J$ colours to classify galaxies as star-forming or quiescent. We used the following criteria:

$$U-V > 1.3 \;\&\; V-J < 1.5 \;\&\; U-V > 0.88(V-J)+0.59, \tag{2.1}$$

as defined by Muzzin et al. (2013a).

The cluster centre is defined as the position of the brightest cluster galaxy (BCG) within each cluster, where the BCG is the most massive galaxy within 500 kpc of the main galaxy overdensity which has a redshift that is consistent with the cluster. We used the velocity dispersions, σ, and R_{200} calculated by Biviano et al. (2021), except for the one cluster not in their sample, SpARCS0219, where we estimated the radius through $R_{200} = \sqrt{3}\sigma/10H(z)$, where $H(z)$ is the Hubble parameter at the cluster's redshift (Schneider, 2006).

2.2.2 Classifying cluster, infall and control field galaxies

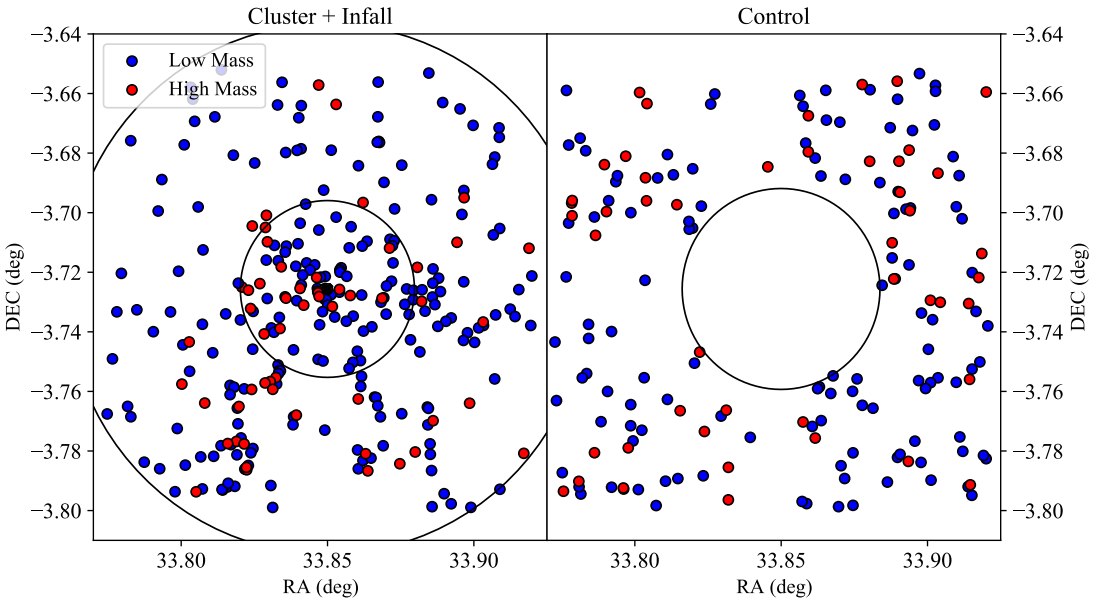

Figure 2.1: Positions of galaxies in our cluster and infall samples (left panel) and control sample (right panel) within the SpARCS215 field. Blue points mark the positions of lower mass galaxies with $9.75 < \log(M_*/M_\odot) < 10.8$. Red points locate galaxies with $\log(M_*/M_\odot) > 10.8$. In the left panel the inner circle marks the R_{200} boundary. Galaxies within the circle (and $|\Delta z|/(1+z) < 0.08$) are classified as cluster members. The outer circle marks $3R_{200}$: infall galaxies lie between the inner and outer circle (and $|\Delta z|/(1+z) < 0.08$). The circle in the right panel marks 1 Mpc from the BCG. The control galaxies are distributed outside this circle with redshifts in the range $0.15 < |\Delta z|/(1+z) < 0.3$.

We define three samples of galaxies: cluster members, infall members, and a

control sample containing galaxies in neither of these environments. We make a distinction between the cluster galaxies that are orbiting the potential and infall galaxies that are gravitationally bound, but not yet in stable orbits, but rather still lie on dominantly radially infalling paths. According to simulations, galaxies within a projected radius of approximately R_{200} are predominantly on orbital paths, whilst those at greater projected radii are predominantly on their first infall towards the cluster (Haines et al., 2015). However, a complication arises due to the presence of backsplash galaxies.

Backsplash galaxies refer to the galaxy population that have passed through the central region of the cluster and are about to turn around to make their second pass of the core (Diemer & Kravtsov, 2014). Although backsplash galaxies make up over half of the galaxies found between R_{200} and $2R_{200}$ around $z = 0$ massive clusters, only 10% of the galaxies between R_{200} and $2R_{200}$ of their progenitors at $z = 1$ are backsplash (Haggar et al., 2020). Thus R_{200} is an appropriate divide that relatively cleanly separates cluster galaxies from infall galaxies for massive clusters at $z = 1$.

We further limit the infall population to those galaxies within $3R_{200}$, which in most cases correspond to $3 - 4\,\mathrm{Mpc}$ (physical). This distance corresponds to the maximal radial extent of 90% of the galaxies that will fall into the cluster by $z = 0$ (Muldrew et al., 2015). We note that not all GOGREEN or GCLASS fields extend as far out as $3R_{200}$. This does not affect our results since will show (in Fig. 2.2) that the infall population looks similar in the two radial bins of $1 < R/R_{200} < 2$ and $2 < R/R_{200} < 3$.

We use photometric redshifts and projected radial distances to define our samples. We define cluster members as galaxies within a projected virial radius (hereafter, $\mathrm{R_{200}}$) of the cluster centre and photometric redshifts within $0.08(1 + z)$ of

the cluster's mean redshift, i.e. $|z_{\rm phot} - z_{\rm cl}|/(1 + z_{\rm phot}) < 0.08$. We define infall members as galaxies that lie between R_{200} and $3R_{200}$ from the cluster centre and have $|z_{\rm phot} - z_{\rm cl}|/(1 + z_{\rm phot}) < 0.08$. The $|\Delta z| = 0.08(1 + z)$ interval was chosen to allow us to directly compare our results with van der Burg et al. (2020).

The $|\Delta z|$ window of $0.08(1 + z)$ encompasses 39 cMpc at $z = 1$ so the cluster and infall regions only reside within a fraction of the volume selected. The galaxy overdensity is expected to be higher in the cluster than in the infall region, thus we expect a higher fraction of interloper contamination in the infall sample. Furthermore, the photometric redshift uncertainties lead to cluster and infall galaxies being scattered out of the cluster and infall samples. This can be corrected if a large and representative sample of the galaxies have a spectroscopic redshift (cf. van der Burg et al., 2020). The cluster sample have sufficient spectra to perform this correction, but the infall sample does not. Therefore, we do not apply corrections to either the cluster or the infall sample. We note that the typical size of the corrections performed by van der Burg et al. (2020) is of order of 20%, or 0.1 dex in the log-log plot of a stellar mass function. Therefore these corrections are relatively minor and are not expected to significantly affect our overall results. Nevertheless, we test the robustness of our results subject to variations in the $|\Delta z|$ membership selection in the discussion section.

In addition to the cluster and infall galaxies we also create a 'control' galaxy sample consisting of galaxies within the GOGREEN and GCLASS fields that lie close to the redshift of the cluster, but not within the cluster or infall volume. Galaxies in this control sample have not experienced the same environmental influences as the cluster and infall galaxies, but are subject to similar observational selection biases.

We define the control sample as those galaxies with photometric redshifts in

the redshift interval $0.15 < |z_{\rm phot} - z_{\rm cl}|/(1 + z_{\rm phot}) < 0.3$, and lie at least 1 Mpc away from the cluster centre, where $z_{\rm cl}$ is the redshift of the cluster in each field. The inner $|\Delta z|$ limit was chosen such that galaxies were at least three times the photometric redshift uncertainty away from the cluster's redshift, whilst the outer boundary was designed to limit the control galaxy sample to a similar redshift range as the cluster and infall samples. The spatial distribution of cluster, infall and control galaxies are displayed for an example cluster, SpARCS0215, in Figure 2.1. In total, the cluster galaxy sample contains 1113 members, the infall galaxy sample contains 1442 members, whilst the control sample contains 2632 members to a mass limit of $10^{10}\,{\rm M}_{\odot}$.

The importance of selecting a control sample with the same data as the environmentally processed galaxy sample has been emphasised by Papovich et al. (2018), however our resulting control sample is relatively small and therefore subject to Poisson noise. Furthermore, in the fields containing $z \sim 1.3$ clusters our control sample includes galaxies up to $z \sim 2$ due to the necessity of selecting control galaxies at a significantly different redshift range from the infall region. This means the completeness corrections we apply to the low mass control field galaxies (see next section) are larger than for the infall and cluster galaxies. This may influence our result so we test the robustness of our results subject to our control sample selection in the discussion section.

2.3 Results

2.3.1 Galaxy stellar mass functions

We begin our investigation of the galaxies in the infall regions surrounding $z \sim 1$ clusters by examining the galaxy stellar mass function (SMF). We combine all the galaxies in the 15 fields, splitting by cluster, infall and control regions, then count the number of galaxies in each sample in mass bins of 0.2 dex in the range $10 < \log[M/M_{\odot}] < 12$. We further divide the galaxies in each sample into star-forming and quiescent galaxy types and construct stellar mass functions for each type of galaxy.

We apply completeness correction factors for undetected sources in each mass bin. Each field has a slightly different detection limit, so we used the $\alpha = 1$ completeness curves given in Appendix A.1 of van der Burg et al. (2020), shifted to the Ks 80% limiting magnitude appropriate to the data the galaxy is extracted from (see Tables 1 in van der Burg et al. (2013) and van der Burg et al. (2020), in each paper respectively). We assign each cluster, infall and control galaxy a weight of 1/completeness(Ks) according to their Ks magnitude. These completeness corrections are relatively minor: $\sim 3\%$ in the lowest mass bin for the infall and cluster samples, and $\sim 16\%$ for the lowest mass bin of the control sample. We apply these weights in each mass bin to derive the corrected stellar mass functions, which are presented in Figure 2.2 with uncertainties assuming a Poisson distribution in each mass bin.

We fit the SMFs with Schechter functions (Schechter, 1976), using the python module `emcee` (Foreman-Mackey et al., 2013) that uses the Markov chain Monte Carlo (MCMC) technique to find the characteristic mass (M_*), low-mass slope (α)

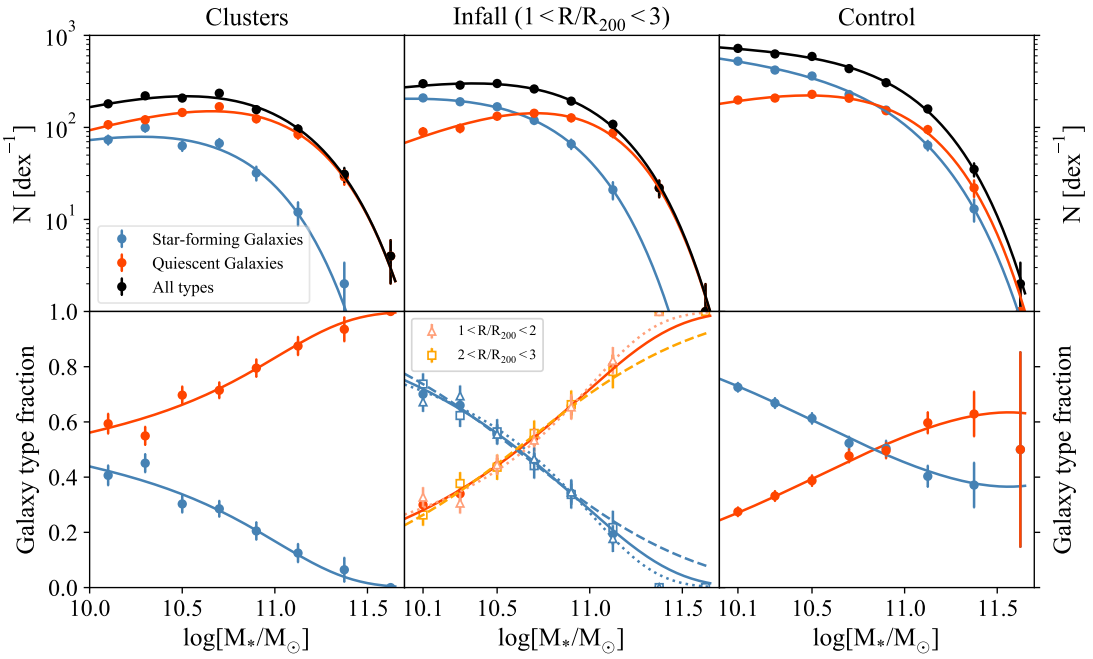

Figure 2.2: Galaxy stellar mass functions (top row) and (bottom) fractions of star-forming (blue) and quiescent (red) galaxies within the cluster sample (left panels), infall (middle panels) and control sample (right panels). Errors on the black points (for all galaxy types) are Poissonian, and binomial errors are used on the subclasses in red and blue. The solid lines are the most likely Schechter functions that fit the data. The dotted (dashed) line in the bottom middle panel displays the fraction of each galaxy type in the inner $1 < R/\mathrm{R}_{200} < 2$ (outer $2 < R/\mathrm{R}_{200} < 3$) regions of the infall. There is no significant difference in the quiescent fractions between these regions so backsplash galaxies do not impact these results.

and normalisation that maximises the likelihood of fitting the data. We overlay the Schechter fits on the raw data in Figure 2.2 showing that both the full population and the star-forming/quiescent subsets in all three samples are well fit by Schechter functions. The most likely values for α and M_* for all the galaxies in the cluster, infall, and control samples are displayed in Figure 2.3, which shows that the shape of the Schechter functions for each sample differ by more than 2σ.

We are unable to measure the volumes of the cluster and infall regions so a comparison of the normalisations of the stellar mass functions does not reveal anything physically meaningful. We are therefore limited to comparing the shapes

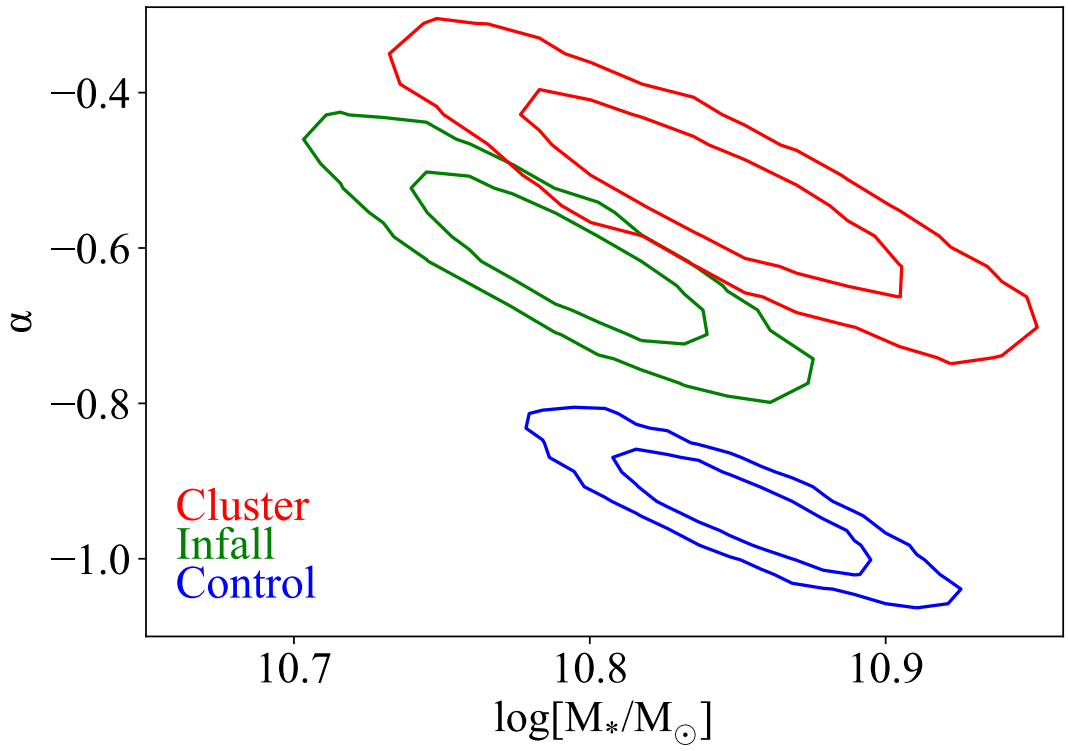

Figure 2.3: The most likely characteristic mass, M_*, and low mass slope, α for the cluster (red), infall (green) and control (bue) samples. The contours mark 1 and 2σ for each population. The low mass slope of the control sample differs by more than 2σ meaning both the cluster and infall samples have top-heavy stellar mass functions.

of the stellar mass functions. The characteristic mass in all 3 samples have similar values of $M \sim 10^{10.83}\,M_\odot$, but the low-mass slopes of the infall and cluster samples are shallower than the control sample. From Figure 2.1 we see that the cluster and infall samples contain higher ratios of massive to low mass galaxies than the control field. Hence the cluster and infall environments contain a relative excess of massive galaxies.

A comparison between the SMFs of our cluster and control sample agrees qualitatively with van der Burg et al. (2020)'s comparison of GOGREEN clusters and the UltraVISTA field. We obtain results that agree within 1σ for the cluster

sample, but the low mass slope of our control sample disagrees slightly with the UltraVISTA calculated in van der Burg et al. (2020) due to our choice of fitting large mass bins (to mitigate the uncertainty in stellar mass) rather than without binning the data (as is done in van der Burg et al. (2020)). We find the low mass slope of UltraVISTA matches our control sample when it is calculated using the same large mass bins we use in this work.

2.3.2 Quiescent galaxy fraction

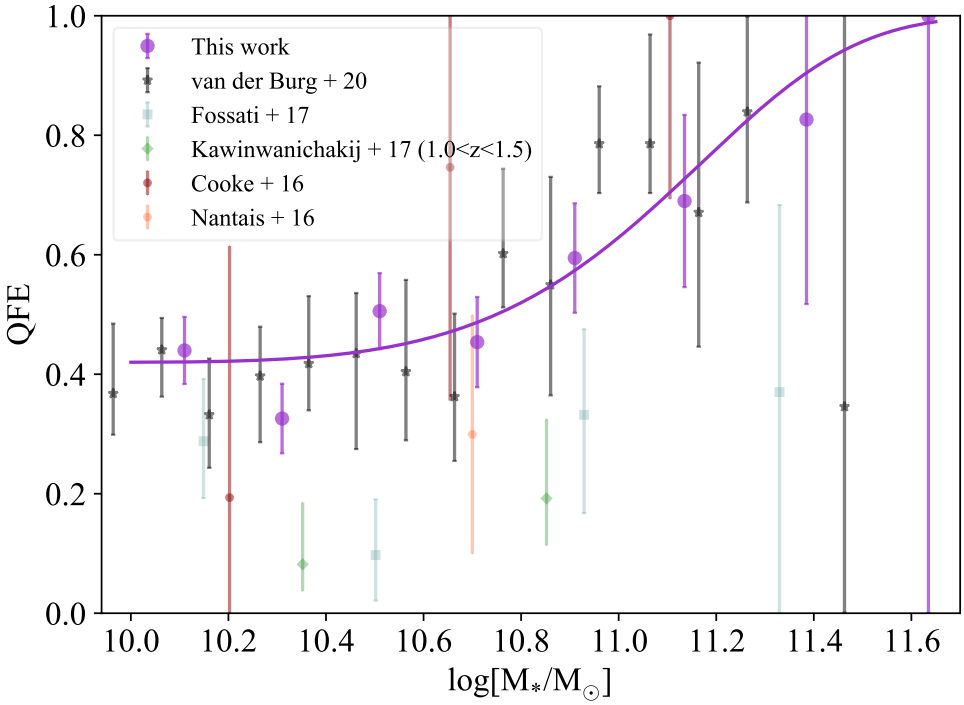

Figure 2.4: The excess of quiescent galaxies in the cluster compared to the control (purple points and solid line). We find a favourable comparison to literature results of a similar redshift and cluster mass: van der Burg et al. (2020) (black), Nantais et al. (2016) (pink) Fossati et al. (2017) (blue), Kawinwanichakij et al. (2017) (green), and Cooke et al. (2016) (dark pink) data. QFE = 0 occurs when there are no excess quenched galaxies in the cluster within the mass bin, whereas QFE = 1 occurs when all the star-forming galaxies in a mass bin are quenched in the cluster.

We calculate the fraction of galaxies in each mass bin that are quiescent and show the results in the bottom panels of Figure 2.2 with binomial uncertainties. To test whether the infall sample is contaminated by backsplash galaxies, we recalculate the quiescent fraction in two subregions: $1 < R/R_{200} < 2$ and $2 < R/R_{200} < 3$. As shown in bottom-middle panel of Figure 2.2, these quiescent fractions are consistent within uncertainties in all mass bins, even though the fraction of backsplash galaxies in the $2 < R_{200} < 3$ sample is predicted to be larger than in the $1 < R_{200} < 2$ sample. We argue, therefore, that backsplash galaxies are unlikely to significantly contaminate the infall sample.

All three galaxy samples present a clear trend of increasing quiescent fraction with increasing stellar mass, in agreement with studies at both low and high redshift (e.g. Peng et al., 2010). The gradient of this trend in the cluster sample is similar to the control sample, but the normalisation is higher. However, the infall sample has a steeper gradient with stellar mass than either cluster or control sample. The most massive infall galaxies share a similar high quiescent fraction as the massive cluster galaxies, but the lowest mass infall galaxies share a similar low quiescent fraction as the control field galaxies. Therefore, the quenching of infall galaxies has a different dependency with stellar mass than either the cluster or control galaxies.

In order to examine the mass dependency of the quiescent fractions in more detail we calculate the Quenched Fraction Excess (QFE) for each sample. The QFE is known in the recent literature by a variety of names, such as the conversion fraction or the quenching efficiency. First defined by van den Bosch et al. (2008), it calculates the excess fraction of quiescent galaxies in one sample relative to another. The samples can be galaxies within different mass bins, or within the same mass bin but in different environments (as in this work). We use the term

QFE rather than conversion factor since the environmental samples we compare may not be related to one another in a evolutionary sequence. For example, cluster galaxies do not evolve from the control field galaxies; the progenitors of the cluster galaxies are infall galaxies.

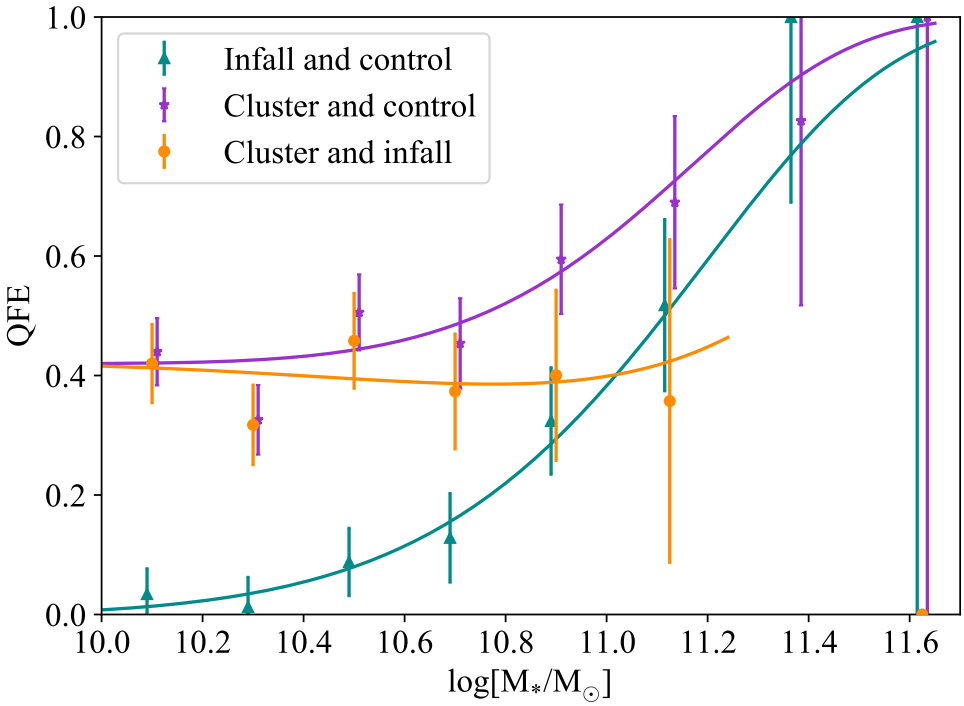

Figure 2.5: The orange data points show that the excess quiescent fraction in the cluster sample compared to the infall sample (QFE_{cl-inf}) is approximately constant across all stellar masses up to $10^{11.2}\,\mathrm{M}_{\odot}$. Above $10^{11.2}\,\mathrm{M}_{\odot}$ there are no excess of quiescent galaxies in the cluster compared to the infall therefore above this limit $\mathrm{QFE}_{cl-inf} = 0$. The aquamarine data points show the excess quiescent fraction in the infall sample compared to the control sample ($\mathrm{QFE}_{inf-con}$), which has a strong mass-dependency. The solid lines are obtained from the Schechter fits to the stellar mass functions rather than fits to the data points.

We define the QFE in each stellar mass bin through:

$$QFE_{2-1} = \frac{f_{\mathrm{q},2} - f_{\mathrm{q},1}}{1 - f_{\mathrm{q},1}}, \tag{2.2}$$

where $f_{q,1}$, $f_{q,2}$ is the quiescent fraction in a stellar mass bin in environment 1 and 2, respectively. A QFE of zero implies there is no excess of quenched galaxies in one environment compared to the other. A high QFE means that many of the star-forming galaxies observed in environment 1 must be quenched in environment 2. In the extreme case of QFE = 1, all of the galaxies that are star-forming in environment 1 would be quenched were they to reside in environment 2.

Figure 2.4 displays QFE_{cl-con}, which measures the excess quiescent fraction in the cluster sample compared to the control sample. We show that the QFE_{cl-con} we measure from our data is quantitatively similar to that of van der Burg et al. (2020), who use the COSMOS/UltraVISTA field as their control field. We take this as reassurance that although our control sample is smaller, and therefore more prone to Poisson noise, it is still sufficient to produce reliable results.

We also compared our results for the QFE with other results in the literature. All studies agree that the QFE of massive galaxies is larger than the lower mass galaxies, but there is significant variation in the absolute values. We obtain good agreement with studies that calculate the QFE using high-redshift clusters (Cooke et al., 2016; Nantais et al., 2016), but studies that divide a large field into density bins obtain systematically lower QFEs (Fossati et al., 2017; Kawinwanichakij et al., 2017). It is likely that the cluster QFE studies are a more direct probe of satellite quenching whereas the field studies have greater contamination by isolated galaxies and therefore the absolute values are not directly comparable.

Having shown our results for the cluster sample are consistent with the literature, we now turn to the main purpose of this work: the infall galaxies. We derive the QFE of the cluster sample compared to the infall sample (QFE_{cl-inf}) and show the results in Figure 2.5. In this case the QFE_{cl-inf} can be considered a conversion factor. The infall galaxies are the progenitors of the cluster galax-

ies, so QFE_{cl-inf} is the fraction of infall galaxies that must be quenched when they fall into the cluster. We also show the QFE of the infall sample compared to the control sample ($\mathrm{QFE}_{inf-con}$) in Figure 2.5. In this case, the QFE should not be considered a conversion factor: control galaxies are not in an evolutionary sequence with the infall galaxies. This is because we have selected the infall region such that it coincides with the region of the proto-cluster that will ultimately collapse to form the $z = 0$ cluster. Hence galaxies within the infall regions were formed within the large-scale overdensity of proto-clusters. The control galaxies lie outside this special overdense region and typically formed in a lower density large-scale environment. Furthermore, at $z \sim 1$, many of the galaxies in the infall region have only recently reached the turn-around point of collapse in the proto-cluster and so they are just starting their infalling orbits onto the cluster core (Muldrew et al., 2015). Therefore, the infall regions abutting $z \sim 1$ clusters are not fed by galaxies from the control environment at $z \sim 1$ and $\mathrm{QFE}_{inf-con}$ simply displays the difference in the quenched fraction between these galaxy samples.

Figure 2.5 shows that the cluster contains a relatively constant excess of quenched galaxies across the entire mass range probed ($\mathrm{M} > 10^{10}\,\mathrm{M}_{\odot}$) compared to the infalling sample. This implies that the process that quenches the infall galaxies when they fall into the cluster does not have a strong mass-dependency. By contrast, we observe a strong gradient in the $\mathrm{QFE}_{inf-con}$ with stellar mass. There is a large excess of massive quenched galaxies in the infall regions compared to the control. Whereas there is almost no excess of quenched galaxies with masses $< 10^{10.5}\,\mathrm{M}_{\odot}$.

We have already shown that any backsplash galaxies present do not affect the quiescent fraction of the infall sample (see middle panel of Figure 2.2), so they do not affect the QFEs displayed here. In the discussion, we show that the choice of

$|\Delta z|$ for selecting infall and cluster galaxies does not affect the QFEs presented here, and in the discussion section we show that the QFE are not sensitive to the selection criteria of the control sample.

The QFEs suggest that massive infall galaxies are quenched more efficiently than similar mass galaxies in the control sample. Since the stellar masses of these galaxies are similar, we hypothesise that the environments are different and a process that depends on environment is responsible for this enhanced quenching rate. In the following section we compare the environments of the massive infall and control galaxies.

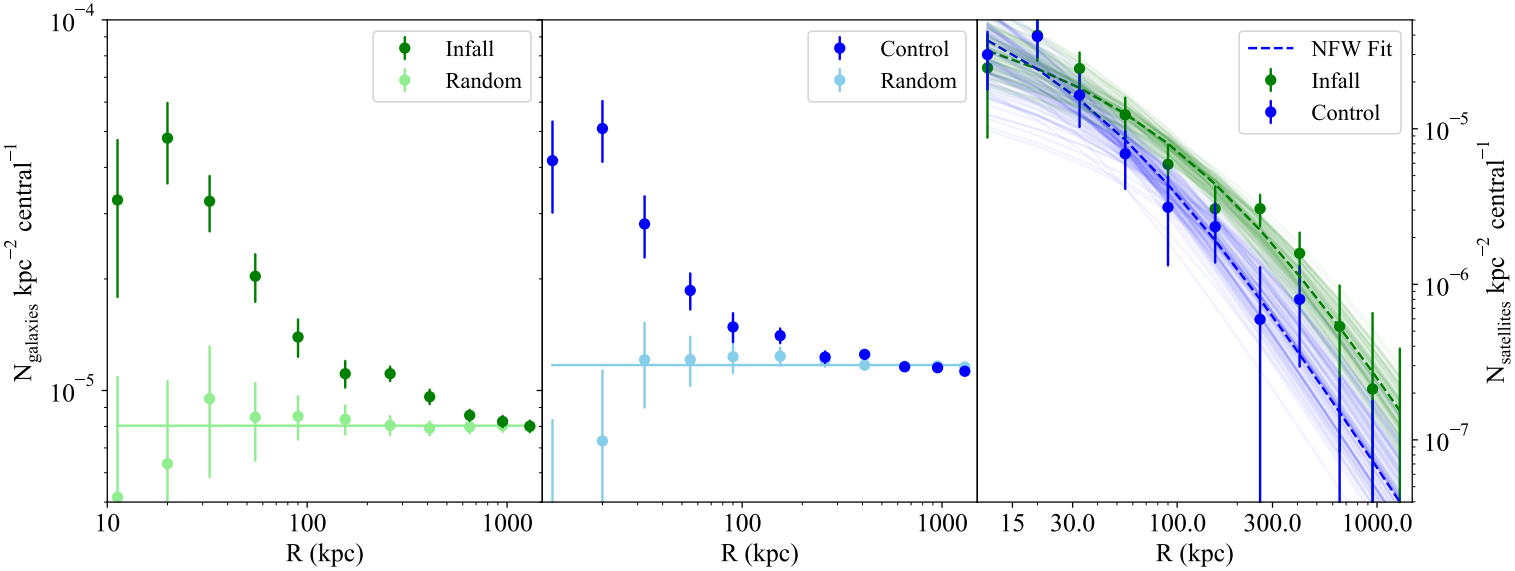

Figure 2.6: Number of (satellite) galaxies per area per central galaxy as a function of projected distance. The left panel displays, in dark green, the density of infall galaxies located in projected radial bins around $> 10^{10.8}\,M_\odot$ galaxies in the infall sample. In light green we display the galaxy density in radial bins around random position in the infall region to measure the expected level of contamination; the solid line is the median. The middle panel displays a similar analysis as the left panel, but using control galaxies of $> 10^{10.8}\,M_\odot$. Subtracting the contamination (straight solid lines) from the dark blue and green points results in the excess satellite galaxy density, which is shown in the right panel. The dashed lines are the most likely NFW fit to the satellite galaxy distributions, whilst the transparent lines are 2% of the samples from the MCMC chain selected by random.

2.3.3 Halo properties of massive infall galaxies

In ΛCDM cosmogonies, massive dark matter haloes grow by the assimilation of smaller haloes. Galaxies that reside in the smaller haloes at the time of accretion become satellite galaxies in the massive halo. Several studies have shown that these satellite galaxies settle into a distribution around the central galaxy according to an NFW (Navarro et al., 1996) profile (Nierenberg et al., 2011, 2012; Tal et al., 2012, 2013; Wang & White, 2012; Watson et al., 2012; Wang et al., 2014; Kawinwanichakij et al., 2014). Hence the number and distribution of satellites around massive infall and control galaxies provides a means to estimate the size and mass of their dark matter haloes.

For each $M > 10^{10.8}\,\mathrm{M}_{\odot}$ galaxy in the control and infall samples we measure the number of lower-mass neighbouring galaxies (to a mass limit of $10^{10}\,\mathrm{M}_{\odot}$) within projected radial bins from 7.5 kpc to 1.5 Mpc. We choose $M > 10^{10.8}\,\mathrm{M}_{\odot}$ since this is the intersection of quiescent and star-forming fractions, as can be seen in Figure 2.2. The $M > 10^{10.0}\,\mathrm{M}_{\odot}$ limit is used due to observational completeness of the sample. We exclude the area of $R < 1\,\mathrm{R}_{200}$ and $R > 3\,\mathrm{R}_{200}$ for infall galaxies and $R < 1$ Mpc for control galaxies, and account for bright stars in each field using the mask images. We apply completeness correction factors for undetected sources in each radial bin since each field has a slightly different detection limit. We assign each infall and control galaxy a weight of 1/completeness(Ks) according to their Ks magnitude, as described in Section 2.3.1, then apply these weights in each radial bin to derive the corrected radial distributions. We calculate uncertainties for the galaxy density in each radial bin by repeating the calculation 100 times using bootstrap with replacement of the galaxy samples and taking the standard deviation of each radial bin.

We also calculate the radial distribution of galaxies around a similar number of random points in each field. For the infalling population we ensure the random positions are distributed at similar distances from the cluster centre as the massive infalling galaxies. We assign each random point a mass $M > 10^{10.8}\,M_{\odot}$ from the stellar mass distribution. We then repeated the process 100 times to obtain the mean galaxy density and standard deviation in each radial bin surrounding these random positions. This provides the level of contamination due to non-associated galaxies that can be expected within each radial bin.

The density of galaxies surrounding the massive infall and control galaxies are shown in the left and central panels of Figure 2.6, respectively. We also show the density of infall and control galaxies around random positions, which is consistent with a constant across all radial bins. There is a strong excess of galaxies surrounding both massive infall and control galaxies out to 1 Mpc and 500 kpc, respectively.

We obtain the satellite galaxy density by subtracting the median density of galaxies around random positions from the number of neighbours around massive infall and control galaxies. We display the density of satellite galaxies in the right panel of Figure 2.6, which shows that massive infall galaxies host significantly more satellite galaxies than similar mass control galaxies in almost all radial bins. To quantify the excess of satellite galaxies we measure the total galaxy excess within $7.5 < R < 500$ kpc for each sample. We detect on average 1.3 ± 0.1 satellites per massive infall galaxy, whereas there are only 0.6 ± 0.1 satellites per massive control galaxy. Thus we find there are twice as many satellites around the infall galaxies than around the control galaxies (significant at a 4.7σ level).

To quantify how this difference in satellite density translates into a difference in dark matter halo mass we fit the radial distributions with projected NFW profiles.

We use the projected profiles from Bartelmann (1996):

$$\Sigma(x) = \begin{cases} n(x^2-1)^{-1}\left(1 - \frac{2}{\sqrt{x^2-1}} arctan\sqrt{\frac{x-1}{x+1}}\right) & (x > 1) \\ n/3 & (x = 1) \\ n(x^2-1)^{-1}\left(1 - \frac{2}{\sqrt{1-x^2}} arctanh\sqrt{\frac{1-x}{1+x}}\right) & (x < 1) \end{cases} \tag{2.3}$$

where $x = r/r_s$, r_s is the NFW scale radius and n is the normalization. We do not include the inner most data point in the fit as it is clear from Figure 2.6 that the density is reduced and therefore does not conform to an NFW fit. This may be due to the difficulty of identifying galaxies so close to the central or due to the effects of dynamical friction and satellite cannibalism.

We use the MCMC technique with the python module `emcee` (Foreman-Mackey et al., 2013) to find the r_s and normalisation that have the maximum likelihood to fit the observed profiles. We overlay the most likely NFW fits on the satellite distributions in the right-hand panel of Figure 2.6, which shows that both control and infall satellites conform to NFW profiles at projected radii > 30 kpc. The profile within 30 kpc is generally better fit by a power-law rather than the NFW-profile (e.g. Tal et al., 2012; Kawinwanichakij et al., 2014).

The 50 and 80% significance contours for r_s and the normalisation are displayed in Figure 2.7. The optimal NFW parameters for the infall sample differ from the control sample at 80% significance. Marginalising over the normalisation parameter, we find the scale radius for the haloes surrounding the massive infall galaxies is larger than the haloes hosting the control galaxies: $r_s = 150^{+75}_{-56}$ kpc for the infall galaxies and $r_s = 50^{+52}_{-22}$ kpc for the control galaxies (1σ uncertainties). However, the size difference is not significant given the errors.

We may lose some satellites of massive galaxies that have photometric redshifts

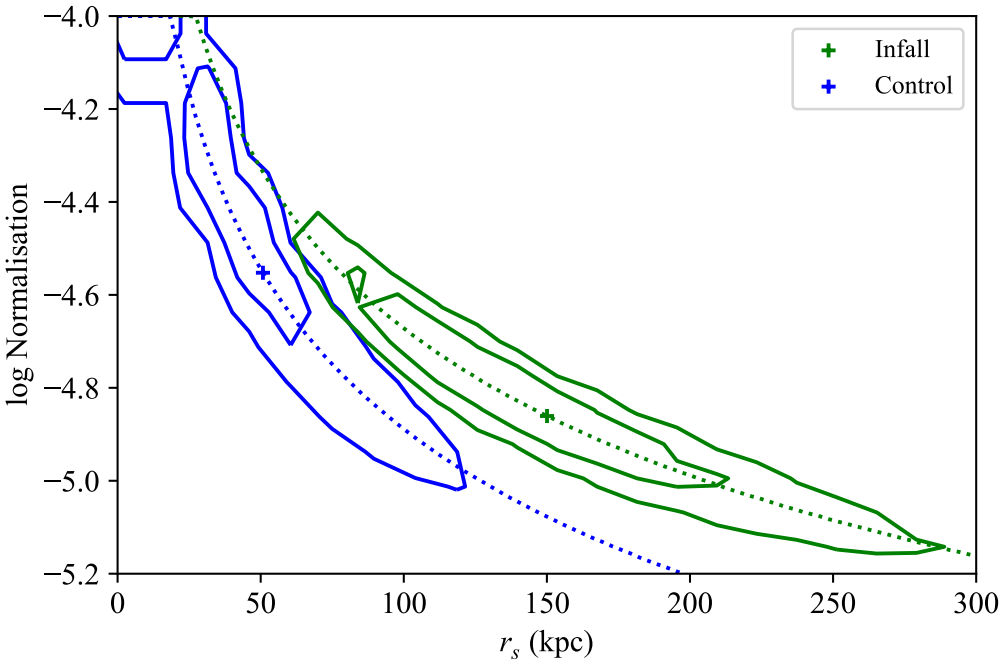

Figure 2.7: Distribution for the scale radius, r_s, and normalisation, n obtained from an MCMC analysis of the projected satellite galaxy distributions for the control sample (blue) and for the infall (green). Contours mark 50% and 80% significance and the dotted lines mark the region of constant integrated galaxy density consistent with the number of observed satellites in each sample.

close to the edges of our redshift intervals. We therefore repeated the above tests, but using infall and control galaxies within redshift intervals that are $0.05(1+z)$ wider than the massive galaxy redshift intervals in each sample. We find similar results: there are on average 1.6 ± 0.1 satellites per massive infall galaxy, whereas there are only 0.9 ± 0.1 satellites per massive control galaxy. Both sets of satellite galaxies are distributed in NFW-like profiles that are consistent with the scale radii presented above.

Both the number of satellites (or richness) within a halo and the scale radius of the halo are proxies for halo mass (Navarro et al., 1996; Papovich et al., 2016), therefore our results suggests that the massive infall galaxies typically occupy

higher mass haloes than control galaxies of the same stellar mass.

2.4 Robustness tests

2.4.1 Influence of cluster and infall sample selection on QFE

The cluster, infall and control samples of galaxies are selected using photometric redshifts. Galaxies which are classified as star-forming typically have weaker 4000Å breaks than the quiescent population, and hence have greater photometric redshift uncertainties. For the control sample, we expect the redshift intervals immediately below or above the chosen control field interval to contain similar number densities of galaxies and fractions of galaxy type. Therefore we expect a similar level of each type of galaxy is scattered into the control sample as are scattered out. Therefore this effect does not greatly influence the galaxy stellar mass functions or quiescent fractions measured in the control sample.

For the cluster and infall samples, however, the redshift interval spanning the cluster has a larger galaxy density than the intervals immediately above and below. Furthermore, the cluster and infall contain higher fractions of passive galaxies than the surrounding control field. Hence fewer galaxies are scattered into the cluster/infall compared to the number that are scattered out. This produces a bias in the galaxy SMFs and quiescent fractions measured in the cluster and infall samples relative to the control sample.

In Figure 2.8 we demonstrate how the photometric redshift errors affect the completeness (ratio of spectroscopic cluster members selected to all spectroscopic galaxies selected) and contamination (ratio of non-cluster spectroscopic members selected to all spectroscopic galaxies selected) of the cluster sample. We use the

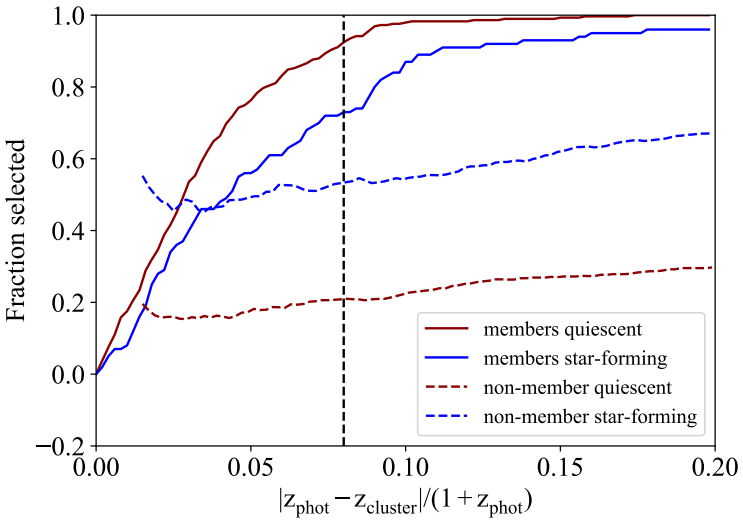

Figure 2.8: The completeness (solid lines) and contamination (dashed lines) fraction of the cluster sample selected using a redshift interval of $|z_{\rm phot} - z_{\rm cl}|/(1+z_{\rm phot})$. The dashed black line marks our fiducial sample selected with $|\Delta z|/(1+z) = 0.08$. Red and blue lines show quiescent and star-forming subclasses, respectively. Both completeness and contamination rates of the cluster sample increase with $|\Delta z|/(1+z)$.

cluster membership of the spectroscopic sample as defined in GOGREEN DR1 (Balogh et al., 2021).

Using the $|\Delta z|/(1+z) = 0.08$ interval we select a cluster sample that is greater than 90% complete in quiescent galaxies, but only 73% complete for star-forming galaxies since a larger fraction of the star forming galaxies have been scattered out of the redshift interval. On the other hand, 54% of the star forming cluster sample are contaminants, whereas only 21% of the quiescent galaxies are contaminants. Again, this is because the photometric redshifts of the star forming galaxies are more uncertain so a large fraction of the star forming galaxies in the adjacent intervals are scattered into the cluster sample than quiescent galaxies.

Figure 2.8 further demonstrates how the completeness and contamination fractions increase as the redshift interval is increased. Thus a different redshift interval can affect the quiescent fractions for the cluster and infall galaxies. In the two left

panels of Figure 2.9 we display the quiescent fraction for cluster and infall galaxies selected using the redshift intervals $|\Delta z|/(1+z) = 0.03,\ 0.05,\ 0.1$. For smaller intervals than the fiducial $|\Delta z|/(1+z) = 0.08$ we obtain larger quiescent fractions at all masses. For the higher interval than the fiducial we obtain lower quiescent fractions at all masses.

We also display the quiescent fraction of the GOGREEN cluster sample measured by van der Burg et al. (2020) in Figure 2.9. The cluster sample of van der Burg et al. (2020) is slightly different to our GOGREEN+GCLASS sample, and they make corrections to account for the fraction of quiescent and star-forming galaxies scattered out of the cluster sample using spectroscopic cluster members. Figure 2.9 demonstrates that our cluster quiescent fractions are consistent so these corrections are relatively minor.

In the two right panels of Figure 2.9 we display the quenched fraction excess, QFE_{cl-inf} and $\mathrm{QFE}_{inf-con}$ selected using the redshift intervals $|\Delta z|/(1+z) = 0.03,\ 0.05,\ 0.1$. Although the normalisation differs slightly, our results for the fiducial $|\Delta z|/(1+z) = 0.08$ case are consistent within uncertainties. Therefore our conclusions remain valid and are independent of our choice of $|\Delta z|$.

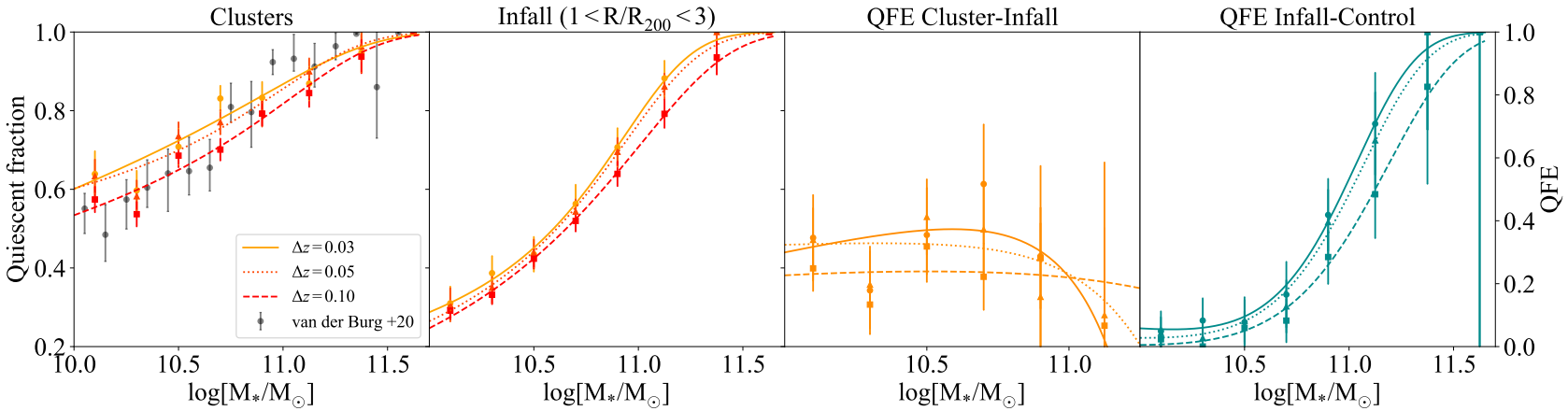

Figure 2.9: The quiescent fractions (two left-hand panels) and QFE (two right-hand panels) derived using infall and cluster samples selected with redshift intervals of $|\Delta z|/(1+z) = 0.03,\ 0.05,\ 0.1$. The quiescent fractions increase when using smaller redshift intervals, however the general trends of the QFE_{cl-pc} and QFE_{pc-con} are consistent with results using the fiducial redshift intervals of 0.08 in Figures 2.2 and 2.5. The grey circles in the left-most panel display the quiescent fraction of a subset of GOGREEN clusters measured by van der Burg et al. (2020), which are consistent with the quiescent fractions we measure.

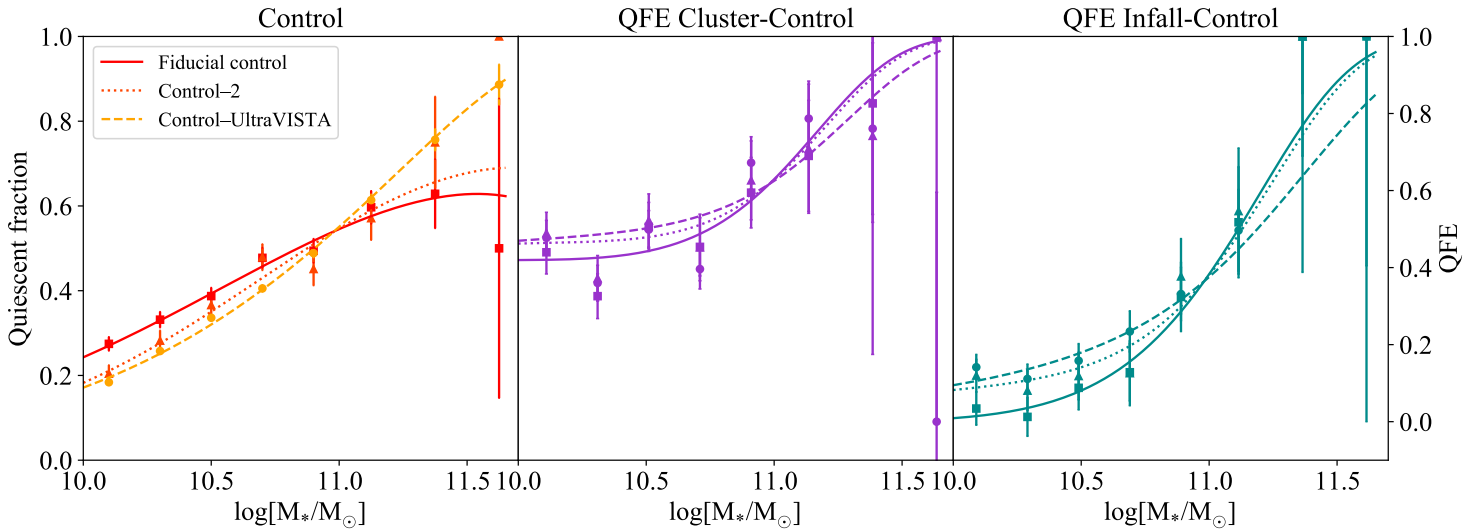

Figure 2.10: The quiescent fractions (left), QFE $_{cl-con}$ (middle) and QFE $_{inf-con}$ (right) derived using the fiducial, Control–2 and Control–UltraVISTA control galaxy samples. The trends are the consistent with that of the fiducial control field sample with only minor differences in the absolute numbers. We therefore surmise that our conclusions are robust against reasonable variations in the control field selection.

2.4.2 Influence of control sample selection on QFE

We select our control field sample from the same data as the cluster and infall sample in order to account for observational biases inherent in all data. We therefore select our control sample from each of the 15 cluster fields by selecting galaxies that lie at least 1 Mpc from the cluster centre and in a redshift range of $0.15 < |z_{\rm phot} - z_{\rm cl}|/(1 + z_{\rm phot}) < 0.3$. The GOGREEN and GCLASS data of each cluster only span approximately 10×10 arcmin^2, which means the area for which we can select control galaxies is limited (as shown in Fig 2.1). As a result the control sample is relatively small, consisting of only 2632 galaxies, and is therefore limited by large Poisson noise. Furthermore, due to the necessity of selecting control galaxies at a significantly different redshift range than the infall region, we include galaxies up to $z = 2.3$ and apply a larger level of completeness correction to the low mass control field galaxies than the infall and cluster galaxies.

To investigate how the above mentioned issues may affect our measurements of the QFE we construct two further control samples and recompute the QFEs. Our fiducial control sample, used in the main body of this work, is constructed from galaxies that lie at least 1 Mpc from the cluster centre and in a redshift range of $0.15 < |z_{\rm phot} - z_{\rm cl}|/(1 + z_{\rm phot}) < 0.3$ within each cluster field. To determine whether the selection of galaxies with redshifts as far as $|\Delta z| \sim 0.3/(1 + z_{\rm phot})$ from the cluster and infall samples affects our results we construct a control sample that is limited to the redshift range of our clusters, i.e. $0.8 < z < 1.5$. We select all galaxies within this redshift range that lie beyond 1 Mpc from the cluster centre. We then remove the infall and cluster members from the sample by removing all galaxies within the redshift limits $|z_{\rm phot} - z_{\rm cl}|/(1 + z_{\rm phot}) < 0.1$ within each field. This control sample, which we call 'Control–2,' consists of 1513 galaxies. Each of these galaxies is associated with a weight, $1/\text{completeness}(Ks)$, that allows us to

correct for incompleteness as done in Section 2.3.1.

Both our fiducial control and Control–2 samples consist of relatively few galaxies and so Poisson noise can have a significant impact on our results. To investigate the impact of Poisson noise we construct a further control sample from the UltraVISTA survey by selecting all galaxies with photometric redshifts in the range $0.8 < z < 1.5$ within the unmasked area of the $1.62\,\mathrm{deg}^2$ DR1 catalogue (Muzzin et al., 2013a). This 'Control–UltraVISTA' sample consists of 23,687 galaxies with $M > 10^{10}\,\mathrm{M}_{\odot}$. We do not apply any completeness corrections since the survey is 95% complete to our stellar mass limit of 10^{10} $\mathrm{M}_{\odot}$ up to $z = 1.5$ (Muzzin et al., 2013a). van der Burg et al. (2020) note that the rest-frame $U - V$ and $V - J$ colours of the GOGREEN and GCLASS data are offset by 0.05 with respect to UltraVISTA. We therefore apply shifts of +0.05 to both the $U - V$ and $V - J$ colours of each galaxy in the UltraVISTA control sample.

We classify galaxies in all control samples as star-forming or quiescent using the criteria in equation 2.1 and plot the quiescent fractions in the left panel of Fig. 2.10. Overall, the trends are qualitatively similar but the fraction of quiescent galaxies for higher (lower) masses is greater (smaller) for the Control-2 and UltraVISTA compared to the fiducial Control.

The Control-UltraVISTA sample contains a high fraction of quiescent massive galaxies relative to the the fiucial control sample we use, although comparible within the Poisson error bars. Although the Poisson noise is smaller for UltraVista, this field contains many galaxy groups that contaminate this control sample, even at $z = 1$ (Giodini et al., 2012). Quiescent galaxies in the highest density regions of such a control field dominates the shape of the SMF, particularly at the massive end (Papovich et al., 2018). Therefore the quiescent fraction of the highest mass bins in the UltraVISTA control sample contains the largest contamination by

galaxy cluster and group members, and therefore is less trustworthy than the small Poisson error bars imply.

In the middle and right panels of Fig. 2.10 we show the impact these different control samples have on the QFE_{cl-con} and $\mathrm{QFE}_{inf-con}$, respectively. The QFE trends are the same for all cases with only minor differences in the absolute numbers of the QFE. Since the use of alternative control samples result in similar QFEs as the fiducial control sample we surmise that Poison noise, cosmic variances and completeness corrections do not greatly affect our conclusions.

2.5 Discussion

An important finding of our study is that there are differences between the infall and control galaxies. The infall sample has a relative excess of massive galaxies (Figures 2.2 and 2.3) and its quiescent fraction has a steeper gradient with stellar mass than the control sample. This results in a higher fraction of massive infall galaxies being classified as quiescent compared to the control sample. However, we not only find that the galaxy population differs, but also the dark matter halo population.

The environmental difference between the infall and control region is revealed through the distributions of satellite galaxies around massive galaxies in both samples. Massive infall galaxies have twice as many satellite galaxies as similar mass control galaxies (4.7σ significance). Both distributions are well fit by projected NFW profiles, but the haloes surrounding the massive infall galaxies have larger scale radii than the haloes around the control galaxies, even though the galaxies have the same stellar masses[2]. Thus the massive infall galaxies are likely to be

[2]The characteristic mass is the same in the proto-cluster and control samples and a

hosted by more massive haloes than similar mass galaxies from a control field.

A small-scale density fluctuation collapses earlier if it lies within a region of large-scale overdensity such as a proto-cluster (Kaiser, 1984; Cole & Kaiser, 1989; Mo et al., 1996; Sheth et al., 2001). This is the basis of biased clustering, where more massive haloes are more biased tracers of the underlying dark matter. Proto-clusters are therefore expected to contain a relative abundance of massive collapsed objects, such as grouped-sized haloes, compared to lower mass haloes, that host galaxies of typical or low masses, with respect to the field. Our measurement of the difference in halo properties between proto-cluster and control galaxies of similar mass allows us to directly observe this bias within proto-clusters.

One important implication of this result is that the control sample is not an appropriate substitute for infall galaxies when calculating the efficiency and mass dependency of satellite quenching in $z \sim 1$ clusters. Using the infall population we calculate the QFE_{cl-inf}: the fraction of infalling galaxies that must be quenched once they fall into the cluster. Figure 2.5 shows that $\sim 40\%$ of the star-forming infall galaxies must be quenched in the cluster and that there is no evidence of a mass dependence in the quenching efficiency over the mass range probed ($10^{10} < M/\,\mathrm{M}_{\odot} < 10^{11.2}$). Above this mass, all infall and cluster masses are already quiescent so no further quenching is required when they become satellites. As the infall galaxies enter the denser environment of the cluster, slightly less than half of them have quenched by $z \sim 1$ due to a cluster-specific process, which our constant QFE_{cl-inf} suggests is independent of stellar mass.

Several recent studies have shown that the QFE at $z \sim 1$ is mass-dependent (Kawinwanichakij et al., 2017; Papovich et al., 2018; Pintos-Castro et al., 2019;

Kolmogorov-Smirnov test finds no significant difference in the stellar mass distribution of galaxies with $M > 10^{10.8}\,\mathrm{M}_{\odot}$ in the two samples ($p = 0.97$)

van der Burg et al., 2020). However, all of these studies calculate the QFE using the lowest density bin or an average/representative sample as their 'field' sample. Indeed, when we use our control sample as the low density sample we also find a mass-dependent QFE_{cl-con} (see Figure 2.4), in agreement with these works. However, the galaxies within the control sample are not the direct progenitors of the cluster galaxies, so this mass-dependent QFE_{cl-con} should not be used to infer the mass-dependency of the satellite quenching process within clusters. Instead, QFE_{cl-con} provides a measure of the galaxy quenching engendered by a combination of mass and environmental quenching processes that occurs in both the infall and cluster regions, as well as the consequence of the environmental dependence of the halo mass function.

A second implication of our results is that excess quenching of star formation occurs in the infall region relative to the control field. The $QFE_{inf-con}$ provides insight to the level and mass-dependency of the excess quenching that occurs in this infall/proto-cluster environment. In both the control and the infall sample we observe a strong mass dependence in the quiescent fraction (Fig. 2.2), which implies that the processes that quench galaxies in both environments are mass-dependent. But Figure 2.5 shows that $QFE_{inf-con}$ has a strong dependency with stellar mass suggesting that the mass-quenching processes have an environmental dependence (in agreement with the results from Pintos-Castro et al. 2019).

We note that the stellar mass to halo mass relation is relatively flat above $M_{\odot} > 10^{10.5}$ (Behroozi & Silk, 2015), so a sample of central galaxies with a narrow range of stellar mass above this limit will inhabit a wide range of dark matter halo masses. If the infall region has a higher density of high mass haloes or galaxy groups than the control region, as we hypothesise, then the same high stellar mass is picking up galaxies within different halo masses/environments in the two regions.

The excess of massive haloes in the infall region/proto-clusters may enhance the quenching rate of galaxies. Contenders for this mass-dependant process include the 'overconsumption' model of McGee et al. (2014) that affects satellite galaxies, or the 'halo-quenching' model of Dekel & Birnboim (2006) or 'AGN-quenching' models (e.g. Benson et al., 2003; Granato et al., 2004; Bower et al., 2006; Croton et al., 2006; Cattaneo & Best, 2009) that affects central galaxies. AGN-quenching is an attractive possibility since cosmological simulations of galaxy evolution show a correlation between black hole and halo mass (Booth & Schaye, 2010) and observations suggest an enhancement of the AGN fraction within proto-clusters (Krishnan et al., 2017). However, with the limited data available we are unable to postulate which physical mechanisms are the most relevant for quenching the massive infalling galaxies.

Because of the excess quenching in the infall region, our results suggest that some cluster galaxies were quenched long before they entered the cluster. We illustrate this in Figure 2.11 where we show the fraction of quiescent cluster galaxies that quenched *after* they fell into the cluster. This is calculated as $\frac{f_{\mathrm{q},cl}-f_{\mathrm{q},inf}}{f_{\mathrm{q,cl}}}$, where $f_{\mathrm{q},cl/inf}$ is the quiescent fraction in the cluster (cl) or infall (inf) region. We also plot the opposite of this fraction, which is the fraction of quiescent galaxies that were quenched *prior* to falling into the cluster. We find that almost all quiescent galaxies with $M > 10^{11}\,\mathrm{M}_{\odot}$ were quenched prior to entering the cluster, whilst up to half of the lower mass galaxies were environmentally quenched after they passed the virial radius. This means the majority of massive quiescent cluster galaxies at $z \sim 1$ were quenched not by satellite quenching in the cluster, but were self-quenched or pre-processed prior to infall.

The hypothesis sketched by this work agrees with the stellar age dating work of Webb et al. (2020), who measured the ages of field and GOGREEN cluster galaxies

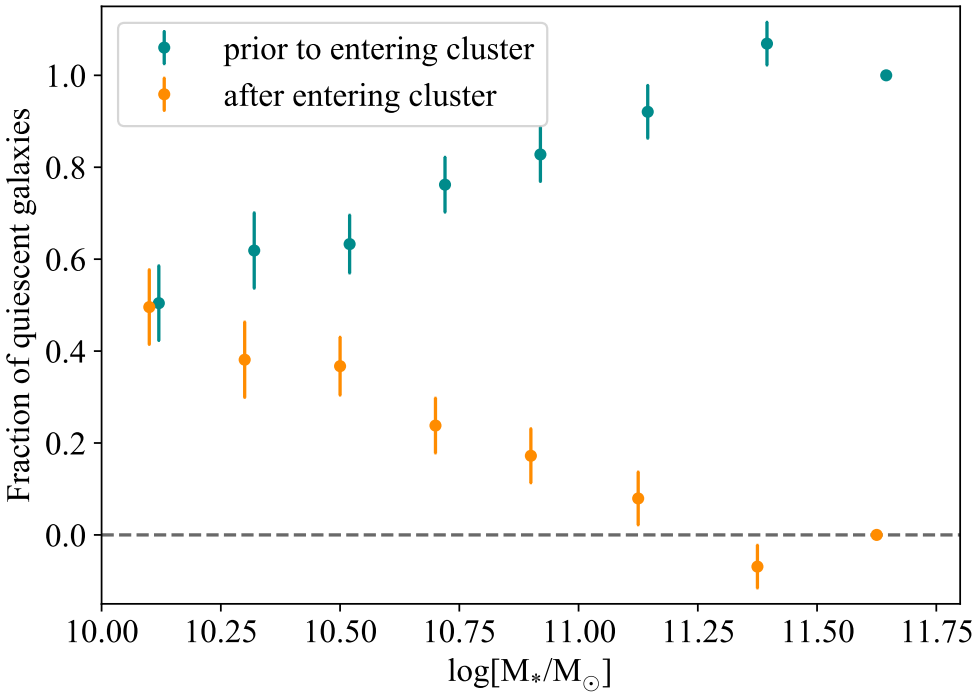

Figure 2.11: The fraction of quiescent cluster galaxies that were quenched *in* the cluster (orange) and *prior* to entering the cluster (blue). Half of the lowest mass galaxies were quenched in the cluster, almost all of the massive cluster galaxies were quenched before they fell into the cluster.

at $z \sim 1$ and found that there is, at most, only a small age difference between them. Since we find that most cluster galaxies were not quenched in the cluster but in the infall region, their ages will reflect the long quenching timescales of self-quenched galaxies rather than the short timescales due to satellite quenching.

We conclude that environmental quenching of satellites within the main halo is not the most important quenching process within the highest redshift clusters, particularly for the most massive cluster members. We therefore surmise that the excess quiescent galaxies observed in these early clusters was a consequence of the proto-cluster environment in which these cluster galaxies formed and evolved.

2.6 Summary and Conclusions

We have analysed the galaxies in the outskirt regions of fifteen $0.8 < z < 1.4$ clusters from the GOGREEN and GCLASS surveys. We compared the masses and quiescent fractions of these infalling galaxies to cluster galaxies and a control sample of field galaxies.

We find that infall galaxies differ significantly from the control and cluster galaxies in terms of their stellar mass distribution and quiescent fraction. The infall regions contain an excess of massive quiescent galaxies with respect to the control sample, and lack low-mass quiescent galaxies compared to the cluster sample. We find that massive infall galaxies are surrounded by twice as many satellites as control galaxies. These infalling satellites are distributed according to an NFW profile with a larger scale radius than the control field. Both of these results suggest that the dark matter haloes surrounding infall galaxies are larger than those surrounding similar mass galaxies in the control field. We infer that the infall region contains a top-heavy halo mass function compared to the control. This different halo environment may be responsible for the excess quenching seen in the infall region compared to the control field via halo-quenching of central galaxies, or increased pre-processing of satellites.

We calculate the excess of quiescent galaxies caused by environmental quenching in the cluster by comparing the infalling galaxies to the cluster galaxies. We find that quenching of satellites in high-redshift clusters is independent of stellar mass. Furthermore, whilst satellite quenching is responsible for $\sim 50\%$ of the low-mass quenched galaxies in the cluster, almost all of the quiescent $> 10^{11}\,\mathrm{M}_{\odot}$ galaxies are quenched before entering the cluster. Thus, most of the excess quiescent galaxies present in high redshift clusters were quenched at an earlier phase

when galaxies evolved in the proto-cluster/infall environment.

We caveat that these results are limited to only $M > 10^{10}\,\mathrm{M}_{\odot}$ galaxies. Furthermore, the presence of backsplash galaxies and photometric redshift errors may impact our results in ways that are not apparent in the robustness checks we have performed.

Chapter 3

Intracluster light in the core of z∼2 galaxy proto-clusters

The content of this chapter has been submitted for publication in the Monthly Notices of the Royal Astronomical Society.

3.1 Introduction

In the standard cosmological paradigm small density fluctuations of dark matter in the early Universe rapidly collapsed into triaxial structures called haloes, which provided a gravitational well deep enough to trap gas and produce the first stars. Over the following 13 billion years, these haloes merge to produce progressively larger haloes. What happens to the stars in these merging haloes is a matter of debate that is pivotal to our understanding of the evolution of galaxies.

Clusters of galaxies are the most massive haloes in the Universe and are therefore the most extreme examples of hierarchical merging. As such, their cen-

tral galaxies, known as brightest cluster galaxies (BCGs), are uniquely suited to study the process of hierarchical galaxy formation. Early galaxy formation models (De Lucia & Blaizot, 2007) predicted that BCGs would undergo protracted growth, in step with the growth of their dark matter haloes. But observations of distant BCGs conflicted with these predictions and demanded only modest growth in both size and mass since z∼1 (Collins et al., 2009; Whiley et al., 2008; Chu et al., 2021). To account for this lack of growth, some models were updated to remove a fraction of the stars from the central galaxies of the merging haloes and deposit them as free-floating stars in the merged halo which is visible as diffuse, intracluster light (Contini et al., 2013). These new models produce modest BCG growth since z∼1 and a corresponding rapid increase in intracluster light over the same period. As a result, these models predict negligible amounts of intracluster light in z∼2 proto-clusters (Contini & Gu, 2021). On the other hand, intracluster stars have been observed in massive clusters up to $z = 1.75$ (DeMaio et al., 2020b) and diffuse UV light has been observed in a proto-cluster at $z = 2.2$ (Hatch et al., 2008). intracluster light appears to be a generic feature of halo assembly, even early on, and not just a low-redshift phenomenon. Recent reviews of intracluster light observations and theory can be found in Montes (2022) and Contini (2021).

To test these models we investigate the amount of intracluster light present within the core of two galaxy proto-clusters at z∼2. CARLA J1018 + 053 (hereafter CARLA J1018) was discovered to be an over-density of galaxies around a radio-loud quasar at z∼1.95 (Noirot et al., 2018; Wylezalek et al., 2013), with potential intracluster light associated with the over-density (Noirot et al., 2018). XLSSC-122 was first identified as a faint X-ray source by the XMM Large Scale Structure survey (Willis et al., 2013), which was subsequently discovered to belong to a $M_{500} = 6.3 \pm 1.5 \times 10^{13}$ $M_\odot$ halo (Mantz et al., 2018) and spectroscopically

confirmed to be a large galaxy over-density at $z = 1.98$ using *HST* grism spectra (Willis et al., 2020b; Noordeh et al., 2021). Both proto-clusters contain similar amounts of stars ($\sim 10^{12}$ $M_\odot$), indicating that the two regions may contain a similar amount of dark matter. However, XLSSC-122 has a large mass gap between its first and second most massive galaxies, unlike CARLA J1018, whose three most massive galaxies have comparable masses. This suggests that XLSSC-122 has already assembled much of its dark matter into a common halo, while CARLA J1018 is still a sprawling proto-cluster consisting of several lower-mass haloes (Golden-Marx et al., 2022).

In Section 3.2 we describe the data we used in this work. The methodology is described in section 3.3.The results are shown in section 3.4 and we present a discussion in section 3.5. We conclude and summarize our findings in section 3.6. Throughout this chapter, we assume a flat, $\Lambda-$cold dark matter cosmological model, parameterized by Ω_M=0.315, Ω_Λ=0.685,H_0=67.4 km s^{-1}Mpc^{-1} (Aghanim et al., 2020), and all magnitudes are based on the AB system.

3.2 Data

3.2.1 Proto-cluster sample

The proto-clusters for this study were selected from a sample of four z$\sim$2 spectroscopically confirmed proto-clusters: XLSSC-122 at $z = 1.98$ (Willis et al., 2020b), CARLA J1018 + 053 at $z = 1.96$, CARLA J0800 + 4029 and CARLA J2039 − 2514 both at $z = 2.00$ (Wylezalek et al., 2014; Noirot et al., 2018). CARLA J0800+4029 and CARLA J20392514 were deemed unsuitable for this study due to contamination of the BCG and the surrounding intracluster light: a large foreground galaxy

and bright star lies along the line of sight to the BCG of CARLA J2039 − 2514, and the most massive galaxy in CARLA J0800 + 4029 is likely to be the luminous $[F140W] = 19.7$ radio-loud quasar, SDSS J0800 + 4029.

3.2.2 Hubble Space Telescope Data

High resolution images for XLSSC 122 were harvested from the *HST* archive (programme ID 15267). The WFC3 images were taken through the $F140W$ filter at four different orientations (across 12 orbits), with a total exposure time of 5,171 seconds, and one orbit of data was taken through the $F105W$ filter, observed at a single orientation, that resulted in a total exposure time of 2,611 seconds. High resolution images and grism spectra were harvested for CARLA J1018 from programme ID 13740. The $F140W$ images were taken in two orbits, each at a different orientation, for a total of 973 seconds. The remaining time of each orbit was used to observe through the G141 grism, details of which are provided in Noirot et al. (2016, 2018).

We performed full end-to-end processing of the *HST* images and grism data using the grism redshift & line analysis software for space-based slitless spectroscopy (Brammer, 2019). The images were flat-fielded using both pixel to pixel flat fields and a delta correction. The sky background is fit during the cosmic ray correction step by computing a linear fit to the accumulated signal from each readout. The astrometric registration uses eDR3 data to perform a fine alignment and a final combined mosaic of all orientations for each filter was achieved using Astrodrizzle and the default distortion correction tables. The output images have a pixel scale of 0.06 arcsec. The *HST* images were masked to remove bad pixels and pixels with less than 66% of the median image weight (measured from the drizzled weight

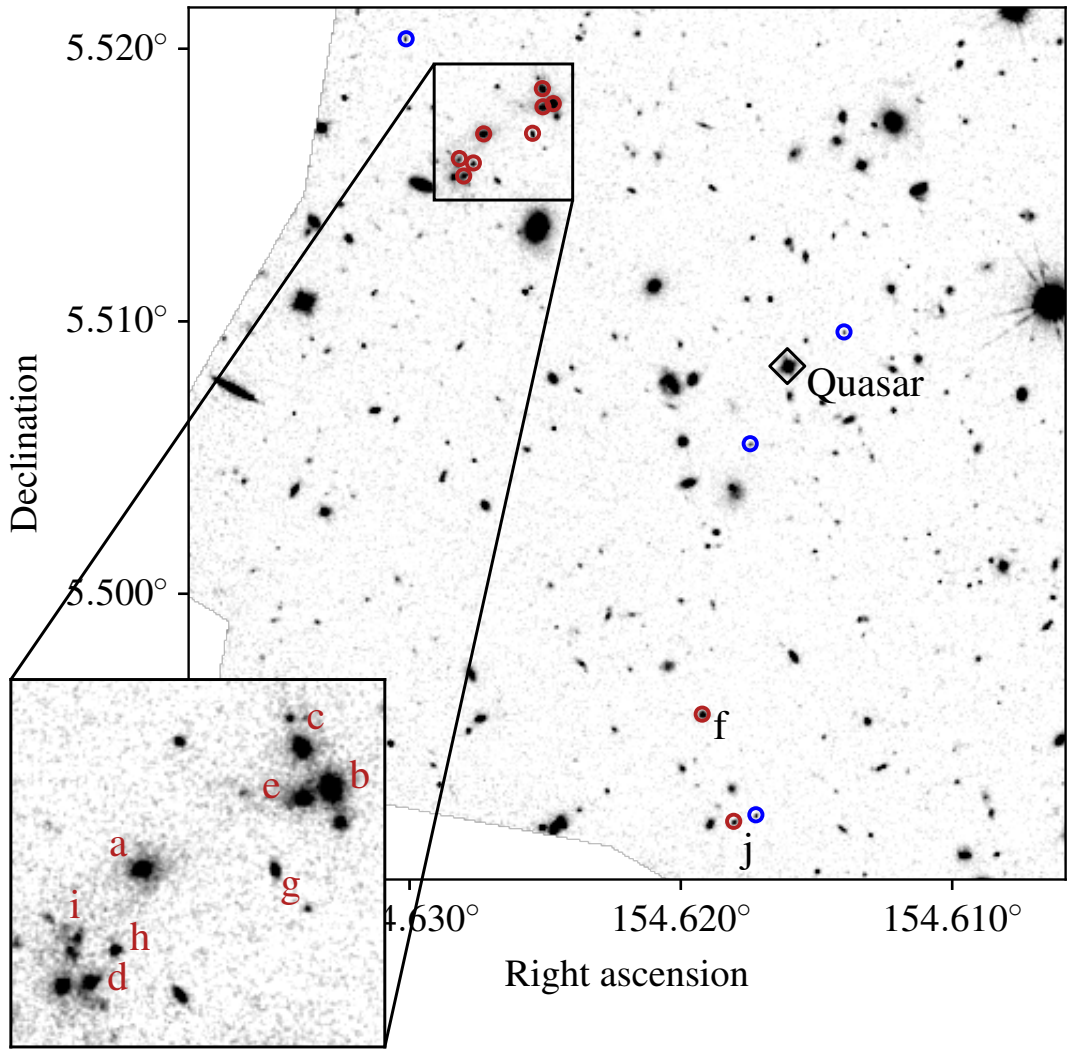

Figure 3.1: The *HST F*140*W* image of CARLA J1018 with marked proto-cluster galaxies. Red circles mark proto-cluster galaxies with strong continuum emission; blue circles mark emission-line galaxies that do not have enough continuum to allow us to measure their mass. The radio-loud quasar is marked by a black diamond. The insert details the region with the highest galaxy density that we take to be the proto-cluster core, with galaxy *a* chosen as the BCG.

images). Furthermore, the $F105W$ image of XLSSC 122 exhibited a defect which was masked using a rectangular aperture of 10.8 by 40 arcsec, centred on [34.4286, −3.7694] and angled by 20°.

We then extracted the grism spectra from the CARLA J1018 data. A source model was constructed from the science image, which was then used to produce a contamination model for the G141 grism spectra. The contamination model was subtracted and finally the clean G141 grism spectra were extracted.

3.2.3 Ground-Based Images

Images of CARLA J1018 at broad wavebands of z, J, H, Ks and two narrow-bands at 1.06 and 1.19µm were obtained using *FORS* and *HAWK-I* instruments on the Very Large Telescope, *ESO* via programmes 094.A-0343 and 096.A-0317. The 1.06 and 1.19µm narrow-band images were obtained because they tightly bracket the 4000Å and Balmer breaks of galaxies at z∼2, so greatly improve the photometric redshift, age and mass measurements of the proto-cluster galaxies. The near-infrared *HAWK-I* data were reduced using standard near-infrared reduction techniques with the *ESO MVM* software (Vandame, 2004). The *FORS* $z-$band data were reduced using the `theli` data reduction pipeline (Schirmer, 2013). We added an archival $i-$band image of this field taken on the William Herschel Telescope (Cooke et al., 2015).

Since the $z-$band image is used to measure the colour of the intracluster light, we ensured the sky background is as flat as possible through the following processes. Each exposure was first flat-fielded using dome flats. Then a single static background model was created from all the exposures taken in each night. The sources were first masked, then exposures were median combined without any as-

Table 3.1: Properties of the ground-based images of CARLA J1018 used to construct the proto-cluster galaxy catalogue in Table 3.3. Image depths were measured in 2 arcsec diameter apertures.

Filter	3σ image depth (mag)	PSF FWHM (arcsec)
i	25.59	0.80
z	25.14	0.64
NB 1.06	23.69	0.75
NB 1.19	23.68	0.60
J	24.58	0.64
H	23.47	0.44
K	23.48	0.64

trometric correction (to correct for the dithering) to produce a sky background model. The structure in the model included low-level fringing and gradients. Each exposure was then corrected for this background model. Finally, we eye-balled each exposure for satellite trails, anomalous reflected light, and poor chip regions and masked these regions on the individual exposures before they were coadded together to produce the final science-grade image.

Flux and astrometric calibration for J, H and Ks images was achieved using *2MASS* catalogues (Skrutskie et al., 2006). For the other ground-based images, relative flux calibration is done based on the universal properties of the stellar locus using stellar libraries (Pickles, 1998; Ivanov et al., 2004) and applying offsets to the instrumental magnitudes so that colours of stars in the images match the reference locus. Finally, we applied Galactic extinction corrections (Schlegel et al., 1998). Properties of these ground-based data are presented in Table 3.1.

The J, H and Ks images were combined to create a deep image from which we detected sources using SExtractor (Bertin & Arnouts, 1996). Since the resolution of the images varied, we Gaussian-smoothed each to match the image with the poorest resolution (the $i-$band image) before fluxes were measured within 2-arcsec-diameter circular apertures. Total fluxes were obtained by applying an

Table 3.2: Surface brightness limits. Limiting surface brightness limits for CARLA J1018 and XLSSC-122 images defined as the 3σ limit derived over a 100 arcsec^2 area.

Cluster	Filter	$\mu_{\rm lim}$(mag/arcsec^{-2})
CARLA J1018	$F140W$	29.2
CARLA J1018	z	27.1
XLSSC-122	$F140W$	30.3
XLSSC-122	$F105W$	30.1

aperture correction determined from the growth curves of unsaturated stars. Uncertainties on the fluxes were taken to be the square root of the photon counts in the apertures plus the standard deviation of the total photon counts within 2-arcsec-diameter apertures placed in empty regions of the images. The final object catalogue was cleaned by removing any source that was located within the regions with less than 30% of the total observing time in each of the seven ground-based images.

3.2.4 Sky subtraction and surface brightness limits

Intracluster light has a low surface brightness and therefore is particularly sensitive to errors in the measurement and subtraction of the background light. It is therefore important to robustly measure the sky background and estimate the uncertainty in the four images we use to calculate the luminosity and colour of the intracluster light. The *HST* images will not be affected by atmospheric emission, and neither target is in a region contaminated by significant amounts of Galactic cirrus, so we expect the background light of these images to be dominated by Zodiacal light and exhibit a smooth distribution over the whole image. However, the $z-$band image comes from a ground-based instrument and is therefore subject to a variable atmospheric sky background, whilst the $F105W$ can be affected by a time varying background due to 1.083 μm He I emission line from the Earth's

atmosphere.

We first measure and subtract a global background from the images. To do this, we detected all sources using SExtractor. We used the default SEXTRACTOR parameters but change the following: DETECT_MINAREA=5, DETEC_THRESH=1.9, ANALYSIS_THRESHOLD=1.9, DEBLEND_MINCONT=0.005 for CARLA J1018, and further updated DETECT_THRESH=1.7, and ANALYSIS_THRESHOLD = 1.7 to detect the fainter sources in the deeper XLSSC image. We then masked all sources to 8 times their semi-major and minor axes to ensure no source light was visible. Finally, we masked the entire 150 kpc region around the BCG to ensure our background measurement was not affected by any potential intracluster light.

We fit a Gaussian to the pixel flux distribution from these masked images. The mean of the distribution is taken as the global background and subtracted from the original images. The standard deviation of the pixel flux distribution is used to derive the limiting magnitudes through $\mu_{\rm lim}(\sigma_\Omega) = {\rm Z_p} - 2.5 \times \log\frac{\sigma(\Omega)}{{\rm pix}\Omega}$, where $\rm Z_p$ is the zero point of the image, pix is the pixel scale, Ω^2 is the area in arcsec^2 over which the limiting magnitude is defined, and the standard deviation of the flux distribution over the area Ω^2 is defined as $\sigma(\Omega^2) = \sigma\sqrt{\frac{\rm pix^2}{\Omega^2}}$, where σ is the standard deviation of the pixel-to-pixel flux distribution. The limiting surface brightness at 3σ over 100 arcsec^2 are listed in Table 3.2.

We quantify whether any large-scale variations in the background are present in the four images we use to measure the intracluster light flux and colour. To do this we placed 5.8 arcsec-radius apertures (corresponding to 50 kpcat the redshift of the proto-clusters) in random locations over the masked images. The distribution of this background measurement conforms to a Gaussian for the *HST* images, which implies that the background noise is uncorrelated and does not contain large variations on this scale. The background in the ground-based z-band image

is well matched to a Gaussian but has a tail to low fluxes. Only 6% of the apertures had anomalously low fluxes. An investigation into the $z-$band image showed that these low fluxes were caused by a clustering of individual low-value pixels in a certain region of the image (far from the BCG of the proto-cluster). Thus, there is no evidence that there are large-scale variations in the background of the $z-$band image. Clustered low-valued pixels were not observed near the BCG and so this should not affect the measured colour of the intracluster light.

3.3 Methodology

3.3.1 Identifying the BCG of CARLA J1018

Table 3.3: Properties of 15 members of CARLA J1018 identified through template fits to the combined grism spectroscopy and photometry. I_{mem} is the probablity of the galaxy being in the redshift of the quasar. A map of their locations in the proto-cluster is shown in Figure 3.1.

Label	Position (J2000)	$Log(M_*/M_\odot)$	I_{mem}	F140W (mag)	Observed M/L
Quasar	10h18m27.8s +05d30m29.9s	-	1.0	19.47	-
a	10h18m30.5s +05d31m00.6s	11.59	0.83	21.50	1.73
b	10h18m29.9s +05d31m04.6s	11.41	0.98	21.27	0.93
c	10h18m30.0s +05d31m06.6s	11.24	0.53	21.48	0.76
d	10h18m30.7s +05d30m55.0s	11.08	0.95	21.49	0.53
e	10h18m30.0s +05d31m04.1s	11.03	0.37	21.50	0.48
f	10h18m28.6s +05d29m43.9s	11.00	0.79	22.09	0.77
g	10h18m30.1s +05d31m00.6s	10.77	0.40	23.27	1.34
h	10h18m30.6s +05d30m56.6s	10.71	0.16	23.14	1.04
i	10h18m30.7s +05d30m57.2s	10.57	0.10	22.55	0.44
j	10h18m28.3s +05d29m29.8s	9.76	0.95	23.19	0.12
#162	10h18m28.1 +05d29m30.68s	-	1.0	24.20	–
#446	10h18m28.2 +05d30m19.71s	-	0.55	24.23	–
#354	10h18m27.4 +05d30m34.47s	-	0.99	24.63	–
#336	10h18m31.2s +05d31m13.2s	–	1.0	24.11	–

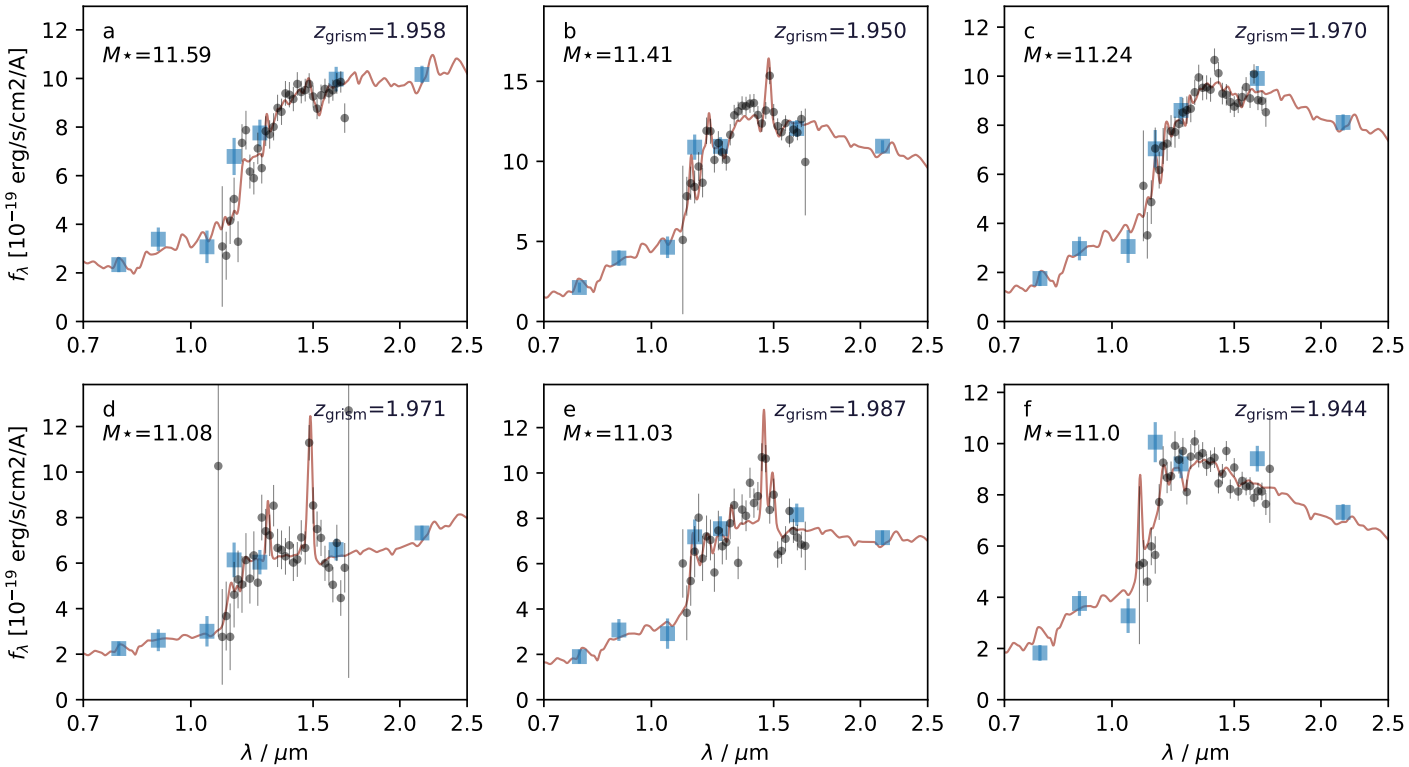

Figure 3.2: Spectral energy distributions of the six most massive galaxies in CARLA J1018. The black circles show the grism spectral data while the blue squares show the photometry from the ground-based images. The galaxy template that best fits the spectral energy distribution is shown in red.

To identify the BCG of CARLA J1018 we first construct a galaxy member catalogue using both photometric and grism data. We used a two-step process to identify the members of the CARLA J1018 proto-cluster within the *HST* field-of-view. We first fitted the ground-based photometry with a suite of galaxy templates using EAZY version 0.5.2 (Brammer et al., 2008) using no redshift prior. The templates were stepped in redshift from 0.01 to 6 over a grid of $\Delta z/(1+z) = 0.01$. During this fitting we iteratively adjusted the zeropoints of the photometry to minimize the template fit residuals. We then combined the zeropoint-adjusted photometric data and grism spectroscopy for the 169 sources that were detected in both data sets.

We then fitted these data with a suite of galaxy templates known as Flexible Stellar Population Synthesis models (Conroy et al., 2009; Conroy & Gunn, 2010) using the software GRIZLI version 1.3.2 (Brammer, 2019). The templates were stepped in redshift over a coarse grid of $\Delta z = 0.004$ between the 68% confidence redshift intervals determined by the EAZY fitting procedure. Finally, the templates were stepped in redshift over a fine grid of $\Delta z = 0.001$ around the peaks in the redshift probability distribution.

There are 275 sources which are detected in the *HST* image that are too faint to have counterparts in the ground-based images. These sources have low levels of continua but can be strong line emitters, so we fit their grism spectra with galaxy templates stepped in redshift from 0.01 to 6 over the same coarse and fine grids as before. We visually inspected each of the fits and removed any spectral extractions that were unreliable due to poor modelling of the contamination by nearby sources.

The best-fit redshifts from the template fitting had uncertainties of typically $\Delta z = 0.006$ for emission line galaxies with strong continuum (e.g. galaxy j in

Figure 3.1) or with extremely strong continuum and strong Balmer/4000Å breaks (e.g. galaxy *a*). However, for galaxies without strong emission lines the typical uncertainty was much larger at $\Delta z = 0.05$. Therefore, selecting proto-cluster members by their best-fit redshifts could introduce a bias against locating passive proto-cluster galaxies. We therefore identified proto-cluster members using two criteria.

We first selected galaxies with a best-fit redshift within a broad window of $z_{\rm cl} \pm 0.05$, then removed those galaxies that did not have a highly peaked redshift probability distribution function over the redshift interval $z_{\rm cl} \pm 0.02$. This interval corresponds to ±2000 km/s, which is three times the typical velocity dispersion of massive clusters at this redshift (Willis et al., 2020b). We defined $\rm I_{mem}$ as the integral of the redshift probability distribution function over the redshift interval $z_{\rm cl} \pm 0.02$, and calculated this for each galaxy. We start with an initial guess of the cluster's redshift at $z_{\rm cl} = 1.95$, determined by previous work (Noirot et al., 2018), then iteratively redefine the cluster's redshift as the mean redshift of galaxies with $\rm I_{mem} > 0.5$ resulting in $z_{\rm cl} = 1.96$. $\rm I_{mem}$ is strongly dependent on the signal-to-noise of the data so galaxies with strong line emission or continuum have larger $\rm I_{mem}$ than lower luminosity members. We therefore eye-balled the redshift probability distribution functions and settled on the choice of $\rm I_{mem} > 0.1$ as defining the redshift probability distribution function as being 'highly peaked.' This value is low enough that it did not rule out low luminosity galaxies with Balmer/4000Å breaks that were distinguishable by eye (such as galaxy *i*), but high enough that it removed galaxies without any clear features in the observed spectral energy distribution or the redshift probability distribution function. Using the criteria of $\rm I_{mem} > 0.1$ and having a best-fit redshift within $z_{\rm cl} \pm 0.05$ resulting in 15 proto-cluster members, which we show in Figure 3.1 and list in Table 3.3.

The photometry and best-fit stellar population templates for the six most massive proto-cluster members are provided in Figure 3.2.

To obtain stellar masses we fit the ground-based photometry with stellar population templates using FAST (Kriek et al., 2009). The stellar population templates are based on Bruzual & Charlot models (Bruzual & Charlot, 2003b) with exponentially declining star formation histories, dust attenuation and a Chabrier initial mass function (Chabrier, 2003b). The redshift of the cluster members is fixed at $z_{\rm cl} = 1.96$, but the masses do not change significantly if the redshift is fixed to the most probable grism redshift. Table 3.3 lists the properties of the 15 proto-cluster members, including the radio-loud quasar SDSSJ101827+0530 that was first used to identify this cluster. We estimate the observed $F140W$ mass-to-light for each galaxy using their stellar masses and observed-frame $F140W$ luminosities.

We identify 6 common members with the original membership catalogue from Noirot et al. (2018): the quasar, galaxy *j* (labelled *#138* in Noirot et al. 2018), and all numbered galaxies in Table 3.3. All numbered galaxies copy the labels given in Noirot et al. (2018). The addition of the ground-based photometry allowed us to reclassify two possible members selected by Noirot et al. (2018), their *#127* and *#647*, as being Hα emitters at a lower redshift. Galaxies labelled a – i are new detections enabled by the additional photometry and the grizli software used to reanalyse the grism data. These new detections have weaker emission lines but stronger Balmer and 4000Å breaks than the galaxies in the original catalogue.

The selection of a BCG for the proto-cluster from Table 3.3 is not straightforward as the galaxies labelled *a* to *d*, as well as the quasar, could all be contenders for the most massive galaxy in the proto-cluster. To differentiate between these galaxies, we consider each galaxy's local density because the barycentre of the proto-cluster is likely to be the region with the highest galaxy density. We rule

out the quasar based on its relative isolation compared to the high-density region around galaxies $a - d$ shown within the insert of Figure 3.1. Out of galaxies $a - d$, we select galaxy a as the BCG because it is the most massive and has the highest galaxy density on the scale of 100 kpc out of all galaxies in the proto-cluster.

3.3.2 Identifying the BCG of XLSSC-122

We use the XLSSC-122 proto-cluster membership catalogue presented in Noordeh et al. (2021) and stellar masses of the XLSSC-122 galaxies that were derived from 2-band photometry in Willis et al. (2020b). However, to compare them with the stellar masses we derive for the CARLA J1018 galaxies, we convert the stellar masses from a Salpeter IMF to Chabrier IMF by multiply the masses by 0.61. From this galaxy catalogue, we select the most massive galaxy as the BCG, which is galaxy *#529* at RA = 34.4342, Dec = −3.7588, with $[F140W] = 20.64$ and a stellar mass of $5 \times 10^{11}\,M_{\odot}$. This galaxy lies near the centre of the X-ray contours (Willis et al., 2020b), and therefore is likely to lie close to the centre of the gravitational well of the most massive dark matter halo in the proto-cluster. Due to the longer wavelength coverage of the data on the CARLA J1018 field, the masses of the CARLA J1018 galaxies are likely to be more accurate compared to those of the XLSSC 122 catalogue, which were derived from only 2-band photometry ($F105W$ and $F140W$).

3.4 Results

3.4.1 Quantifying the intracluster light in z∼2 proto-clusters

To isolate the diffuse light, we mask all the high surface brightness sources except for the BCG. We use the SEXTRACTOR-derived source catalogue described in section 3.2.4 and mask all objects, except the BCG, to four times the semimajor and semi-minor axes of objects using the SEXTRACTOR parameters (A_IMAGE and B_IMAGE). We checked the resulting masked images by eye and increased the mask size, by up to 10 times the semi-major and semi-minor axis, for large galaxies and very bright stars for which the smaller mask was insufficient. The masked galaxies in the 100 kpc surrounding the BCGs can be seen in Figure 3.3. In this figure we also see diffuse low surface brightness emission extending up to 100 kpc from the BCG which resembles intracluster light.

We quantify the amount of intracluster light in the proto-cluster cores by measuring the luminosity of the BCG and intracluster light within three projected annuli of <10 kpc, 10 to 50 kpc and 50 to 100 kpc around each BCG (marked on Figure 3.3) and list them in Table 3.4. The inner-most aperture is dominated by light from the BCG whilst the outer annulus is dominated by intracluster light. The uncertainty in the background within each of these apertures was estimated by placing apertures, of the same size and shape, at random locations over the fully masked image described in the section above on sky subtraction and image depth. The standard deviation of the fluxes (within the ∼1000 apertures which have a comparable unmasked area as the regions of interest) is taken as the uncertainty in the sky background.

Table 3.4: The luminosity and stellar mass of the BCG & intracluster light within the z∼2 proto-clusters. The luminosities were measured inside circular apertures and annuli centered on the BCG. The uncertainties account for any residual variations in the background as they are measured from the standard deviation of flux measured in ∼1000 randomly distributed apertures across each image. Note that the stellar mass uncertainties are purely statistical and do not account for systematic uncertainties due to the uncertain mass-to-light ratio.

	$F140W$ observed luminosity ($10^{11}L_{\odot}$)			Stellar mass ($10^{11}M_{\odot}$)		
Aperture range (kpc)	<10	10 – 50	50 – 100	<10	10 – 50	50 – 100
CARLA J1018	1.8 ± 0.1	2.4 ± 0.2	53.2 ± 0.4	1.5 ± 0.1	0.8 ± 0.1	1.0 ± 0.1
XLSSC 122	2.2 ± 0.1	2.6 ± 0.1	2.8 ± 0.4	1.2 ± 0.1	1.4 ± 0.1	1.6 ± 0.2

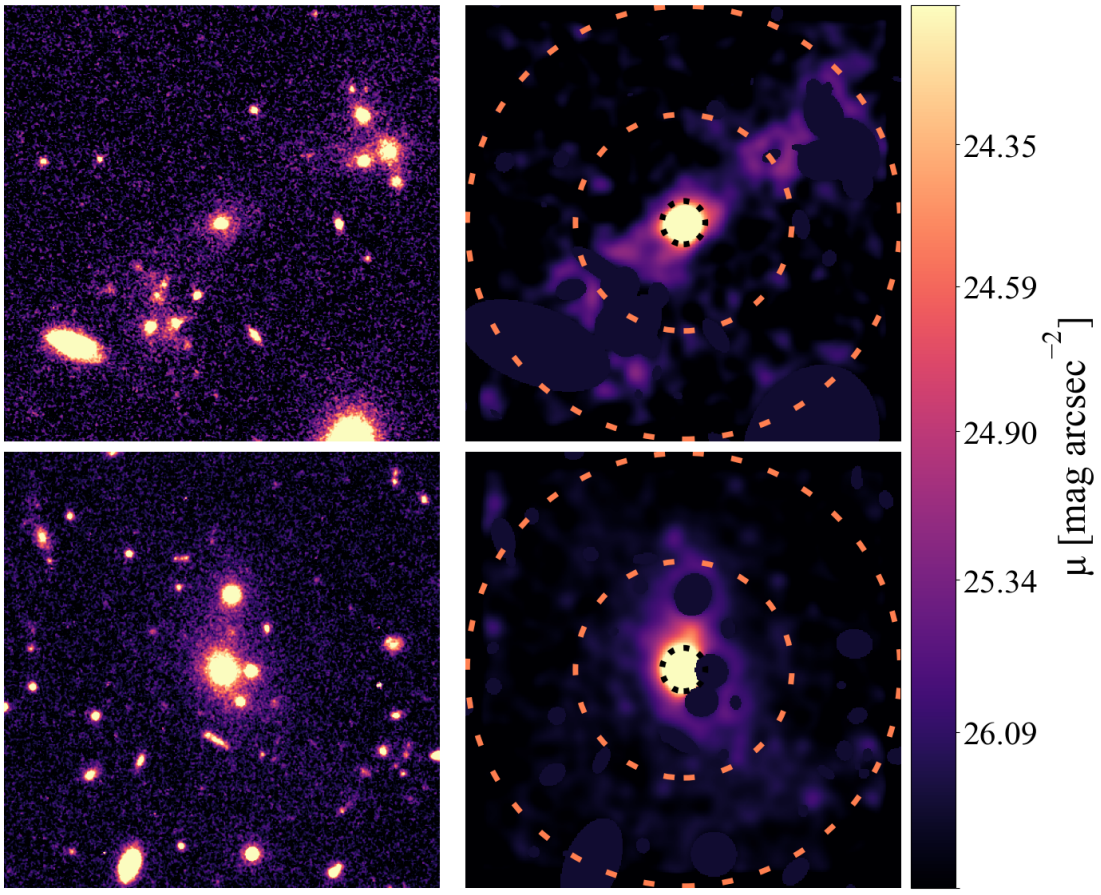

Figure 3.3: *HST* images of the core of the CARLA J1018+0530 (upper panels) and XLSSC 122 (lower panels) proto-clusters (F140W band). The left images show the BCG, intracluster light and surrounding galaxies at the native resolution of the *HST* images. On the right, we highlight the light from the intracluster stars by masking all galaxies, except for the BCG, then smoothing the remaining pixels with a Gaussian 2D kernel of $\sigma = 0.12$ arcsec. The dashed circles mark a radial distance from the BCG centre of 10, 50 and 100 kpc.

We find that both proto-clusters contain at least two times more light in the region beyond 10 kpc than within 10 kpc of their central galaxies, demonstrating that these proto-clusters host significant amounts of intracluster light. We also measure the total light within a 100 kpc-radius circular aperture, and defined the concentration of the light as the luminosity within 10 kpc compared to the luminosity within a 100 kpc radius, with uncertainties resulting from the fractional errors in the 10 and 100kpc apertures added in quadrature. We find the light concentration in the centre of the XLSSC 122 proto-cluster is 0.29±0.03, and 0.23±0.02 in the CARLA J1018 proto-cluster.

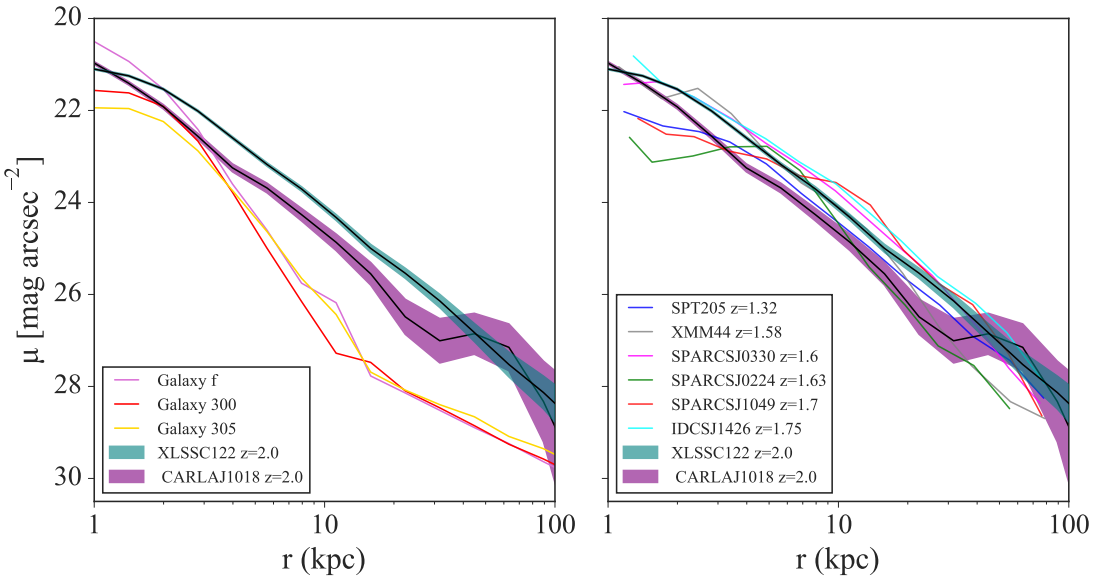

Figure 3.4: Radial surface brightness profiles for the BCG within the CARLA J1018 (purple) and XLSSC 122 (blue) proto-clusters. All other galaxies were masked from the $F140W$ *HST* images. In the left panel, we compare the surface brightness profiles of the BCGs to the three most massive galaxies within the proto-clusters that lie far outside the cores (*300* and *305* from XLSSC 122 (Noordeh et al., 2021) and galaxy *f* within CARLA J1018). The BCGs have a uniquely extended morphology that is not shared by other proto-cluster galaxies. In the right panel, the surface brightness profiles are compared to BCGs at lower redshifts (DeMaio et al., 2020b); redshift-corrected to $z = 2$ to enable a direct comparison with the two proto-clusters at z∼2.

We check whether the presence of diffuse light is unique to the BCGs or is a generic feature of massive proto-cluster galaxies by comparing the projected circular radial profiles of the BCGs to other proto-cluster galaxies with similar stellar masses of more than 10^{11} $M_{\odot}$. We only find three galaxies with such high masses outside the central 100 kpc of the proto-clusters (galaxies labelled *#300* and *#305* in XLSSC 122 by Noordeh et al. 2021 and galaxy *f* from CARLA J1018). The surface brightness profiles of these three galaxies, shown in the left panel of Figure 3.4, are much steeper than the BCGs, and the light concentration of these galaxies are all greater than 0.89 which is three times higher than either of the BCGs. The BCGs, therefore, have a distinct light profile that is more extended than other massive proto-cluster galaxies. In the right panel of Figure 3.4, we compare the light profile of the $z \sim 2$ BCGs to BCGs at lower redshifts that are known to be surrounded by intracluster light (DeMaio et al., 2019). The surface brightness profiles of the proto-cluster BCGs have remarkably similar profiles to the cluster BCGs, providing clear evidence that intracluster light is already present in these proto-clusters.

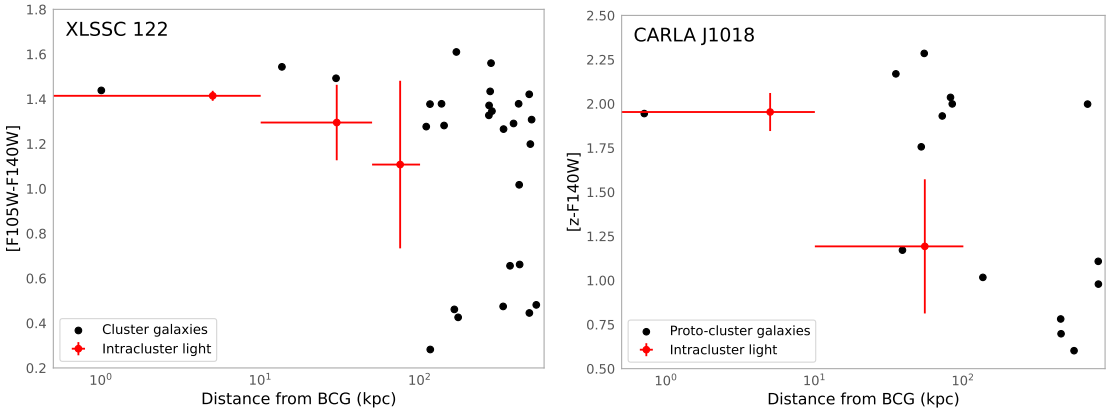

Figure 3.5: The colour of the BCG and intracluster light (red) compared to the proto-cluster galaxies (black dots) in XLSSC 122 (left) and CARLA J1018 (right). The intracluster light in XLSSC 122 has a similar colour to the red proto-cluster galaxies and we assume that the intracluster stars have the mass-weighted mass-to-light ratio of proto-cluster galaxies with colours of $[F105W - F140W] > 1.1$. The colour of the intracluster light in CARLA J1018 is significantly bluer in the outskirts than in the core region. We therefore calculate the mass of the stars within 10 kpc using the mass-weighted mass-to-light ratio of proto-cluster galaxies with colours of $[z - F140W] > 1.5$, whilst the mass of the stars beyond 10 kpc are calculated using the mass-weighted mass-to-light ratio of proto-cluster galaxies with colours of $[z - F140W] < 1.3$.

3.4.2 Stellar mass of the intracluster light

To compare our discovery of intracluster light within proto-clusters to the predictions of simulations, such as Contini & Gu (2021), we need to convert the luminosity to an estimate of the stellar mass. We use the colour of the intracluster light to estimate the mass-to-light ratio in each annulus. We combine the *HST* $F140W$ images with images of light from below the Balmer break in the rest-frame of the proto-cluster galaxies. For XLSSC 122 we use an *HST* image taken through the $F105W$ filter, whilst for CARLAJ1018 we use a $z-$band image taken from the ground (from VLT). We estimate the colour of the light in three radial bins for XLSSC 122 and two wider bins for the shallower CARLA J1018 images and compare them to the colours of the proto-cluster galaxies in Figure 3.5. Although

we measure the colours, it is important to note that these colours are difficult to assess since the data come from different telescopes (HST and VLT) and have different bands, and then had different data reductions.

The intracluster light within XLSSC 122 has a similar $[F105W] - [F140W]$ colour as the proto-cluster members that reside on the red sequence ($[F105W] - [F140W] > 1.1$). We assume that the intracluster light is produced by the stripping and destruction of proto-cluster galaxies, and that all galaxies are stripped equally. Under these assumptions the appropriate mass-to-light ratio for the intracluster light is the mass-weighted mass-to-light ratio of all the XLSSC-122 proto-cluster galaxies with $[F105W] - [F140W] > 1.1$. Using the stellar masses (renormalised to a Chabrier IMF) listed by Noordeh et al. (2021), we find that such red galaxies contain a total mass of 10^{12} $M_{\odot}$. We transform the observed fluxes into absolute magnitudes to derive a total $F140W$ luminosity of $1.8{\times}10^{12} L_{\odot}$. Thus, the observed mass-to-light ratio through the $F140W$ filter is 0.56 for the intracluster light in XLSSC 122.

The colour of the intracluster light within CARLA J1018 varies with radius. To compare the intracluster light colour with the colour of the galaxies, we perform aperture photometry on the $F140W$ and $z-$band images using four times the semi-major and semi-minor axis of the catalogues detected by SExtractor for the masking. These large apertures are chosen to ensure we have all the galaxies' light, even in the ground-based $z-$band image, which has a higher PSF than the space-based $F140W$ image.

In the inner 10 kpc, the light matches the colour of the red sequence galaxies with $[z - F140W] > 1.7$. The mass-weighted mass-to-light ratio for these galaxies is 0.89, which we adopt for the light within this aperture. This ratio is larger than that found for XLSSC 122 because the XLSSC 122 contains several bright, low

mass galaxies which bring down the mass-average mass-to-light ratio of the red galaxies. The CARLA J1018 $F140W$ and grism data is shallower than the XLSSC 122 data which results in fewer detections of low-mass red galaxies. However, any undetected low-mass galaxies are unlikely to greatly influence the mass-averaged mass-to-light ratios: the core region of CARLA J1018 contains several 10^{11} $M_{\odot}$ galaxies which negates the impact of any (undetected) low-mass galaxies on the mass-averaged mass-to-light ratios.

Beyond 10 kpc, the intracluster light of CARLA J1018 is significantly bluer and is similar to galaxies i and j. The other five blue galaxies do not have measurable masses as they are not detected in the images taken by the VLT, and therefore they cannot be included in this calculation. The mass-weighted mass-to-light ratio of galaxies i and j is 0.32.

We convert the light measured in each aperture to stellar mass using these mass-to-light ratios and list them in Table 3.4. The main limitation of these results is the strong dependence of the stellar concentration on the assumed mass-to-light ratios for each radial bin. Simulations suggest that the intracluster light comes from stripping of the massive galaxies in the forming cluster (Merritt, 1984; Rudick et al., 2006), which justifies our using the mass-weighted mass-to-light ratios of the galaxies to estimate the mass-to-light ratio of the intracluster stars. However, to be cautious we explore how alternative mass-to-light ratios affect our conclusions in section 3.5.1.

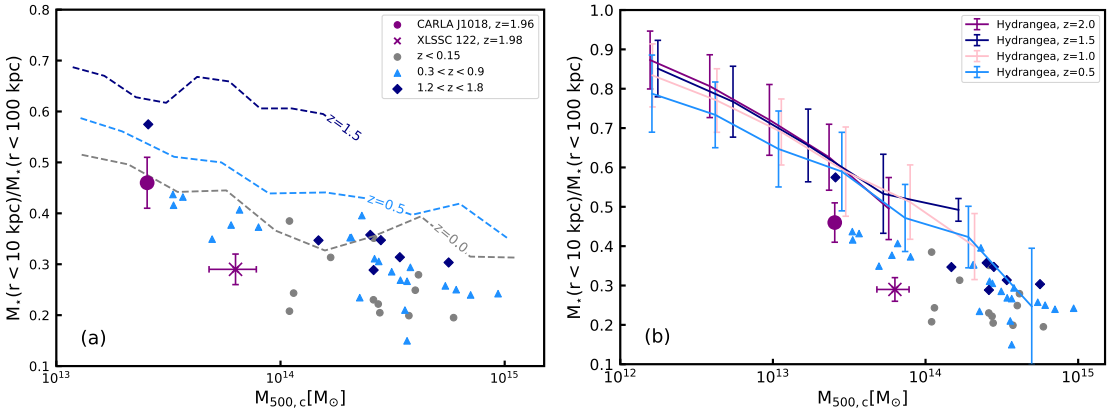

Figure 3.6: The concentration of stellar mass within the z∼2 proto-clusters (purple symbols), defined as the ratio of stellar mass within 10 kpc to the stellar mass within 100 kpc, versus the total halo mass ($M_{500,c}$). Grey and blue symbols show lower redshift clusters gathered from the literature (DeMaio et al., 2020b), which suggests an inverse relationship between the stellar mass concentration of the core and the total cluster mass ($M_{500,c}$). In the left panel, the dashed lines display the predicted concentrations from the semi-analytic models of Contini & Gu (2021), whilst in the right panel the solid lines display the predicted concentrations from the Hydrangea hydrodynamical simulations (Bahé et al., 2017).

3.4.3 Comparing the proto-cluster stellar mass concentration to simulations

We define the concentration of stellar mass as the fraction of stellar mass within 100 kpc that lies within the central 10 kpc, $\frac{M_*(<10\,\mathrm{kpc})}{M_*(<100\,\mathrm{kpc})}$, and find that the stellar mass is more centrally concentrated in CARLA J1018, with $\frac{M_*(<10\,\mathrm{kpc})}{M_*(<100\,\mathrm{kpc})} = 0.46 \pm 0.05$, compared to XLSSC 122, with $\frac{M_*(<10\,\mathrm{kpc})}{M_*(<100\,\mathrm{kpc})} = 0.29 \pm 0.03$. The quoted uncertainties are only from uncertainties in the light measurement within each aperture and do not include any systematic uncertainty from the assumed mass-to-light ratio. In Figure 3.6, we compare these stellar mass concentrations of the proto-cluster cores to lower redshift clusters from the sample of DeMaio et al. (2020b).

The stellar mass concentration of the lower redshift clusters exhibits a mild trend with halo mass and no dependency on redshift. XLSSC 122 lies on the same relation of concentration-halo mass as the lower redshift clusters, and we use this relation to estimate a halo mass of CARLA J1018 based on its stellar mass concentration. To find a relation between $\frac{M_*(<10\,\mathrm{kpc})}{M_*(<100\,\mathrm{kpc})}$ and $M_{500,c}$, where $M_{500,c}$ is the mass within the radius at which the density is 500 times the critical density of the Universe, we applied a least-squares algorithm to all clusters in the sample of DeMaio et al. (2020b), regardless of their redshift. We derive the following relation: $\frac{M_*(<10\,\mathrm{kpc})}{M_*(<100\,\mathrm{kpc})} = 2.57 - 0.16\log\frac{M_{500,c}}{10^{14}}$. The stellar concentration of 0.46 within CARLA J1018 implies an approximate total cluster mass of $M_{500,c} \sim 10^{13.4} M_\odot$. We note this is within a factor of five of the halo mass estimate of Mei et al. (2022) based on the galaxy overdensity, but both estimates should be considered unreliable as they have been derived through methods that have not been well tested.

In Figure 3.6a we compare our data to the predictions of intracluster light from the semi-analytic model of Contini & Gu (2021). The intracluster stars in this model are produced from an analytic model that takes a fraction of the stars from satellite galaxies as they orbit the BCG, as well as harvesting a fraction of the stars from galaxies merging with the BCG. Full details of the model are provided in Contini et al. (2013). Once stripped, the intracluster stars are assumed to follow an NFW profile (Navarro et al., 1997) modulated by a concentration parameter, $\gamma(z)$, so that the simulations reproduce the observed relation between the stellar mass within 100 kpc and the total mass, M_{500}, at each redshift. By varying the stellar concentration parameter, these simulations can reproduce the observed stellar mass within 100 kpc of the centre of clusters at $0 < z < 1.5$ (Contini et al., 2020). We use the optimal concentrations derived by Contini et al.

(2020): $\gamma(0) = 3$, and $\gamma(> 0) = 5$, for the lines shown in Figure 3.6a.

These models are designed to match the observed slow growth rate of the BCG, so in this simulation the BCG has mostly assembled by $z \sim 1$ and the surrounding intracluster light builds up around it over the following 7 Gyr. The stellar concentrations therefore decrease with decreasing redshift as stars from mergers and stripping preferentially accumulate beyond the outskirts of the BCG. The highest redshift model predictions are at $z \sim 1.5$, since above this redshift the intracluster light is predicted to be negligible and the stellar concentrations tend towards unity.

The stellar mass concentrations from the Contini & Gu (2021) model agree with the observed concentrations at $z = 0$, but the model prediction at $z \sim 1.5$ is much higher (which means less intracluster light) than both $z \sim 2$ proto-clusters as well as other clusters at $z \sim$1.5. This remains true regardless of the assumed halo mass of CARLA J1018. Our discovery of intracluster light at $z \sim 2$ implies that the formation of the intracluster light began earlier than predicted by this model. A possible way to bring the model into agreement with the observations is to limit the growth of the BCG at $z > 2$ by diverting some stars from early mergers to form the intracluster light.

We explore how intracluster stars can be produced in such abundance by $z \sim 2$ by analysing the formation of intracluster stars within the Hydrangea hydrodynamical simulations (Bahé et al., 2017). These are a suite of 24 zoom-in simulations of massive galaxy clusters within which the equations of gravity are solved for collisionless dark matter and stellar particles, with additional hydrodynamical equations solved for gas particles. Numerical subgrid algorithms are used to solve for the other ingredients of galaxy formation, such as cooling, star formation, stellar feedback and black hole growth (see see Schaye et al. (2014) and Bahé et al.

(2017) for details). The positions of star particles are traced throughout the simulation so the stellar distribution can be used to test the fidelity of the model. Using these simulations, Alonso Asensio et al. (2020) showed that the distribution of the intracluster stars closely follows that of the total mass distribution at $z \sim 0$. This agrees with recent observations that showed the intracluster light followed the mass distribution within the central 140 kpc (Montes & Trujillo, 2018). To create the data shown in Figure 3.6b we extracted the stellar mass concentration within four snapshots of the simulations: $z = 0.47$, $z = 1.02$, $z = 1.49$ and $z = 1.99$. Within each snapshot, we identified the central galaxy (the BCG) of each dark matter halo with a mass greater than 10^{12} $M_{\odot}$. The stellar mass concentration is calculated as the ratio of stellar mass within 10 kpc to the stellar mass within 100 kpc, excluding any stars within these 3D apertures that are gravitationally bound to satellite galaxies. We separated the data from each snapshot into halo mass bins, then calculated the average stellar mass concentration and the standard deviation of the concentration for the haloes in each halo mass bin, which are displayed in Figure 3.6b.

In these hydrodynamical simulations the redistribution of stars during mergers and stripping depends only on gravity and the position of stars within galaxies. Hence the distribution of intracluster stars in this simulation is a direct prediction of hierarchical merging, modulated only by the galaxy evolution model. We find that the concentrations from these simulations are in good agreement with the observations. The simulations reproduce the dependence of the stellar concentration on the halo's total mass and its lack of dependence on redshift, although the predictions are slightly above the observed concentrations at all redshifts. These simulations correctly identify a large amount of intracluster light at $z \sim 2$ in massive haloes, and hence the early intracluster light growth in principle can be

explained as a natural consequence of hierarchical merging occurring in the first 3 billion years. However, we caution that these simulations produce too many stars in the centres of clusters and the BCGs end up three times too massive by the present day (Bahé et al., 2017). This means that the galaxy model has not yet solved the issue of restraining the BCG stellar growth. We therefore still lack a solution that both restrains BCG growth and allows large amounts of intracluster light to be present at $z > 2$.

3.5 Robustness Tests

3.5.1 The impact of the mass-to-light ratio on the stellar mass concentration

The uncertainties on the colour, and hence mass-to-light ratio, of the intracluster light beyond 10 kpc within CARLA J1018, and beyond 50 kpc in XLSSC 122 can significantly affect our conclusions of a low stellar mass concentration, so it is worth investigating how different mass-to-light ratios will affect our conclusions. First, we consider an extreme case in which the mass-to-light ratio beyond 50 kpc of XLSSC 122 is extremely low such that the mass in this region is negligible. Even in this extreme case, the mass concentration would increase to only 0.46 ± 0.04, which is still compatible with the trend for other clusters seen in Figure 3.6 and lies far below the model predictions of Contini & Gu (2021).

Next, we consider the lowest plausible value of the mass-to-light ratio for the ICL beyond 10 kpc in CARLA J1018. We start by examining colour variations in the ICL. We place four rectangular apertures across the brightest region of the ICL in the $F140W$ image, but not covering the central 10 kpc from the BCG. The

centres of the apertures were at [154.6255, 5.5183], [154.6264, 5.5175], [154.6279, 5.5161], [154.6288, 5.5152], each of 39×93 kpc and at an 45° angle. All apertures had measurable $F140W$ and $z-$band fluxes at more than a 1.5σ level. The colours of the four regions were $[z - F140W] = 0.9$, 1.1, 1.0 and 1.6 from South-east to North-west, which means there is colour variation in the intracluster light and a single mass-to-light ratio does not capture the complexity of this system. Nonetheless, we can use a single mass-to-light ratio to estimate a minimum mass in this outer region and take that as a lower limit to the true mass. The colour of the intracluster light in the annulus of 10 to 100 kpc is $[z-F140W] = 1.2 \pm 0.4$. Thus, the minimum colour of the intracluster light, assuming maximal measurement uncertainties is $[z - F140W] = 0.8$. The intracluster light in all smaller regions have a redder colour that this, reassuring us that this is the bluest possible colour of the intracluster light.

We compare this colour to a set of stellar population models in Figure 3.7. Such a blue colour can only be achieved with a stellar population model that is actively forming new stars, such as a constant star formation history or a very young (0.5 Gyr), exponentially declining model with a long timescale for the decay of the star formation rate. The mass-to-light ratio also depends on the assumed IMF, with a Salpeter IMF producing a higher mass-to-light ratio than the Chabrier IMF. Throughout this work we assume a Chabrier IMF, however, evidence points to a peculiar stellar IMF in clusters (Friedmann & Maoz, 2018). By assuming a Chabrier IMF, we therefore take the minimum plausible mass-to-light ratio for the intracluster light. For a Chabrier IMF, a colour of $[z-F140W] = 0.8$ corresponds to a minimum mass-to-light ratio of 0.14. Applying this minimum mass-to-light ratio to the intracluster light beyond 10 kpc, the luminosity concentration of 0.23 implies a mass concentration of 0.66. This value is still compatible with the ob-

served trend for lower-redshift cluster BCGs, and below the measurements for other massive galaxies in the proto-cluster.

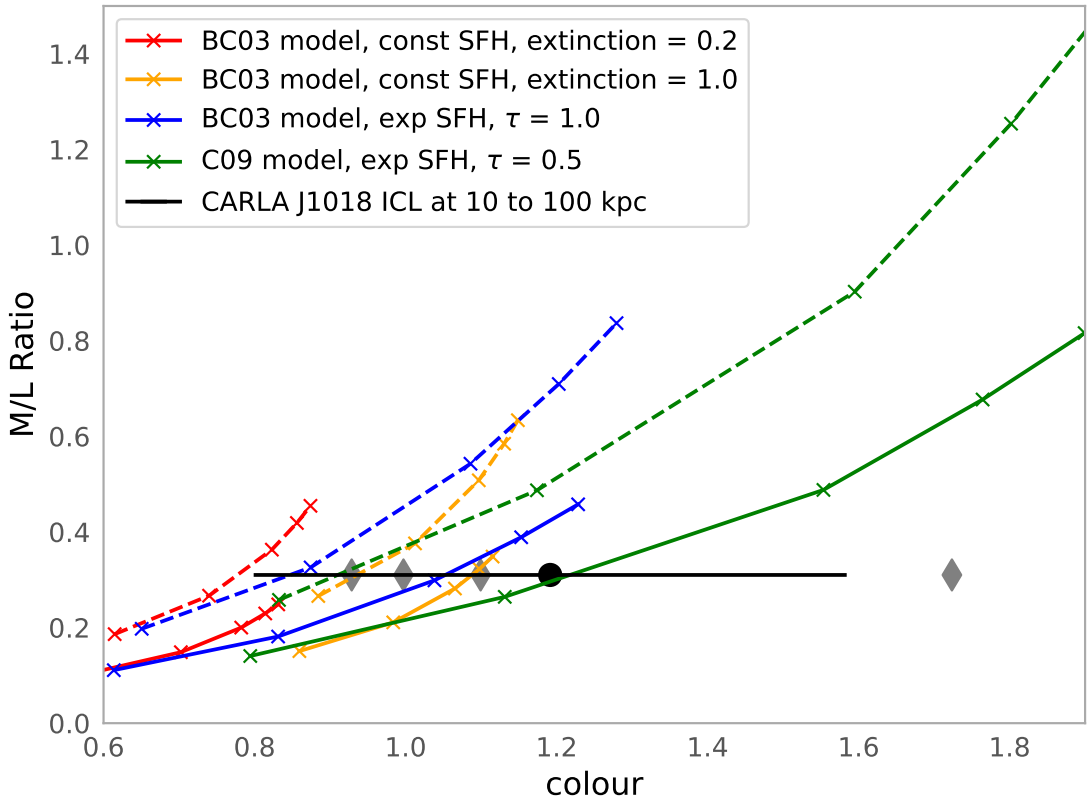

Figure 3.7: The relationship between the $[z - F140W]$ colour and mass-to-light ratio for galaxies at $z = 1.96$. The colour of the intracluster light in CARLA J1018 between 10 and 100 kpc is shown as the black point with 1σ uncertainties. The grey diamonds display the variety of intracluster light colour in the four rectangular regions described in the text. The coloured lines show the mass-to-light ratio from galaxies simulated with different star formation histories and Chabrier (solid) or Salpeter (dashed) IMFs. The crosses from the bottom left to top right of each line mark the colour of galaxies formed at $z = 2.5$, 3, 4, 5 and 6 and observed at $z = 1.96$. The lowest possible colour of the intracluster corresponds to a minimum mass-to-light ratio of 0.14. We take this to be the minimum possible mass-to-light ratio for the intracluster light in CARLA J1018.

3.5.2 Defining the BCGs in the proto-clusters

The selection of the BCG can also affect our conclusions of a low stellar mass concentration. Whilst there is no other plausible candidate for the BCG in XLSSC 122, the selection of galaxy a as the BCG of CARLA J1018 is not certain as galaxies b, c, d, as well as the quasar, could all be the most massive galaxy in the proto-cluster. We therefore used the local surface density of galaxies to determine which of these galaxies is most likely to be at the barycentre of the proto-cluster. We selected galaxy a because it is the most massive and has the highest galaxy density on the scale of 100 kpc out of all galaxies in the proto-cluster. However, our results do not qualitatively change if we chose galaxies b, c or d to be the BCG: we still find significant intracluster light regardless of which galaxy is chosen to be the BCG. Quantitatively, the amount of light within 100 kpc radius would be reduced if the BCG was chosen to lie at the edge of the high-density region shown in the insert of Figure 3.1, and the amount of intracluster light that would be classified as residing beyond 100 kpc would increase. Therefore the exact values of the mass and light concentrations will increase, although they are still low compared to other massive galaxies, both within and beyond the proto-cluster. Thus, our conclusion remains valid as long as the dense region in the insert of Figure 3.1 is the barycentre of the proto-cluster.

The argument given above only holds if we can use the surface density of galaxies as a proxy for the true 3D density; if the dense core region in the insert of Figure 3.1 is only due to the projection of unrelated galaxies, then this region may not be the barycentre of the proto-cluster. We therefore compare the probability that the galaxy overdensity is due to a chance line-of-sight distribution to the probability that these galaxies are in close proximity and are interacting with each other.

The area of the region depicted in the insert of Figure 3.1 is 0.31×0.32 co-moving Mpc^2 (16.8×17.1arcsec^2) and the line-of-sight co-moving radial distance spanned by the interval $\Delta z = 0.04$ is 60.4 Mpc, so the volume is 6.1 Mpc^3. The number density of $> 10^{11}$ M$_\odot$ galaxies at $z \sim 2$ is 10^{-4} Mpc^{-3} (Muzzin et al., 2013b) so the probability of observing any galaxy more massive than 10^{11} M$_\odot$ in this volume is 0.06%. The probability of detecting five unrelated galaxies, of more than 10^{11} M$_\odot$, within this volume is vanishingly small at less than one in a trillion.

On the other hand, the chance of observing two massive galaxies that are in the process of merging is much higher. Simulations predict that a 10^{11} M$_\odot$ galaxy at $z = 2$ will merge with another galaxy, of at least a quarter of its mass, at a rate of 0.15 Gyr^{-1} (Rodriguez-Gomez et al., 2015). Galaxy mergers can be identified as close pairs of galaxies, and the length of time a merger is visible depends on the projected separation and mass ratio of the pair. For galaxies within a 1 : 4 mass ratio this timescale varies from a few hundred Myr to 1.5 Gyr depending on the projected separation (Lotz et al., 2011). The projected separations of the galaxies in the core region range between 12 and 36 kpc (proper) so these mergers will be visible for an average of 0.6 – 1 Gyr. Thus, the probability of observing a massive galaxy undergoing a merger with another nearby galaxy is 10 to 15%. Since there are five galaxies more massive than 10^{11} M$_\odot$ in the core, and hence 10 unique pairs, there is a 60 to 80% chance that we would observe these galaxies undergoing a merger. Assuming each merger is mutually exclusive and treating the closer merger pair as a single entity, the probability of observing five massive galaxies merging at the same time is 0.01 – 0.05%. This is much higher than the chance of observing 5 unrelated massive galaxies distributed across the 60.4 cMpc line-of-sight, hence it is more likely that the dense galaxy group we have observed in CARLA J1018 is the barycentre of the proto-cluster than a chance line of sight

alignment.

The space density of $> 10^{11}\,\mathrm{M}_{\odot}$ galaxies is $10^{-4}\,\mathrm{Mpc}^{-3}$ (Muzzin et al., 2013b), and we have calculated that between one in a hundred to one in twenty of these will be undergoing extreme merging events such as that seen in the core of the CARLA J1018 proto-cluster. This means the space density of such extreme merging events is $10^{-6}\,\mathrm{Mpc}^{-3}$. This is the same space density as galaxy clusters with masses greater than $10^{14.3}\,\mathrm{M}_{\odot}$ in the nearby Universe (Vikhlinin et al., 2009). It is therefore plausible that such extreme merging events signpost the formation of a galaxy cluster's core.

3.6 Discussion

3.6.1 The implications of finding intracluster light in proto-clusters

Our work extends the baseline over which intracluster light has been investigated to some of the most massive haloes at $z \sim 2$. At this epoch, typically less than 20% of the matter that will end up in the cluster has assembled into the main halo (Muldrew et al., 2015), and the haloes that we have observed are below the general limit of a cluster-sized halo and more akin to galaxy groups. But our images show that the central 100 kpc of these proto-clusters already contain intracluster stars.

The Hydrangea simulations agree that intracluster light can exist at such a high redshift, and go further to suggest that intra-halo stars, i.e. stars that are in haloes but gravitationally unbound from any galaxy, are present in massive haloes up to at least $z \sim 2$. As these massive haloes merge to form larger groups and accrete onto clusters their intra-halo stars will combine. Stars that were already

unbound from galaxies when they accrete onto the cluster are defined as having been 'pre-processed'. Since the Hydrangea simulations suggest that all massive haloes contain intra-halo stars, it is likely that pre-processed stars are a significant source of intracluster stars. Therefore semi-analytic simulations should take care to include intra-halo stars at $z > 1$, even in haloes of masses as low as $10^{12}\,\mathrm{M}_{\odot}$.

Our findings also argue against a significant contribution of intracluster stars coming from the stripping of satellite galaxies as they orbit in the cluster, at least near the centre. Such a stripping mechanism would build up intracluster light over time regardless of whether the halo grows significantly in mass. Thus, if stripping of orbiting satellites were a dominant contributor to intracluster stars we would expect the stellar mass concentration to strongly depend on redshift and only weakly depend on halo mass. Such evolution in the stellar mass concentration can be seen in the models of Contini & Gu (2021) displayed in Figure 3.6a, but these do not match the trends seen when combining our data with the larger sample from DeMaio et al. (2020b).

Our observational data find the opposite trends: a strong dependence on halo mass and little (or no) dependence on redshift. The stellar mass concentration in the $z \sim 2$ proto-clusters is comparable to group-sized haloes at $0.1 < z < 0.9$ which have similar masses. The groups at $z < 0.9$ have had much more time to strip stars from satellites than the $z \sim 2$ proto-clusters, thus such stars cannot be a major source of intracluster stars within the central 100 kpc. It is plausible, however, that such stars contribute much more to the intracluster light at larger radii.

Our results should be interpreted in the context of the inside-out growth of stellar mass in clusters proposed by DeMaio et al. (2020b). These authors showed that the amount of stellar mass within the central 100 kpc of clusters continued

growing until $z \sim 0.4$; the intracluster light beyond 100 kpc will likely continue growing to the present day. Furthermore, the mass growth rate of intracluster stars exceeded that of the halo. Therefore, the diffuse light we see in the proto-clusters comes from their nascent intracluster stellar population, which will extend both in size and mass over the following 10 Gyr.

3.6.2 Prospects for detecting proto-cluster intracluster light with ESA's Euclid Mission

Our discovery of intracluster light at $z \sim 2$ means that it is possible to use the signature of diffuse low-surface-brightness light and low stellar mass concentrations to identify clusters and proto-clusters from high-resolution images, such as will be provided by ESA's *Euclid* mission. This is particularly useful at $z > 1.5$, where the photometric redshifts that *Euclid*'s cluster finders use are not precise enough to identify galaxy clusters. The presence, or lack, of intracluster light can be used to remove contaminants from the cluster catalogues based on photometric redshifts. Furthermore, since the presence of diffuse light is unique to the central galaxies in proto-clusters, this is an excellent way to identify the dominant halo within a proto-cluster.

The *Euclid* Wide Survey is predicted to reach a surface brightness of 29.1 mag/arcsec^2 in VIS (3σ over 100 arcsec^2) and 27.7 mag/arcsec^2 for Y, J, and H−band NISP images (Scaramella et al., 2022; Borlaff et al., 2022), whilst the Deep Survey will reach 2 magnitudes fainter. This means that the Deep Survey will reach similar depths to the *HST* $F140W$ images we use in this work (29.2 and 30.3arcsec^2 in CARLA J1018 and XLSSC-122, respectively) but over a much larger area.

It is also likely that intracluster light will be detected in the Wide Survey of *Euclid*. The surface brightness of the intracluster light in the region between 10 and 50 kpc ($\sim$100 arcsec^2) in both proto-clusters presented in this work is $[F140W] \sim 26.5$ mag/arcsec^2, and $[F140W] \sim 27.1$ mag/arcsec^2 averaged over the larger region between 10 and 100 kpc (~ 430 arcsec^2). Thus, we predict that the intracluster light in both proto-clusters would be detected in the near-infrared images of *Euclid*'s Wide Survey.

Whether the intracluster light is also detected in the VIS images depends on the colour of the light. The reddest colour of the intracluster light that we measure is $[z - F140W] \sim 2$, which means the surface brightness could be as low as $z = 29.1$ mag/arcsec^2. The VIS instrument covers the wavelength range 550 to 900 nm, so it covers light blueward of the $z-$band image we use in this work. Hence, intracluster light at $z \sim 2$ is likely to be detected in VIS images of the Deep Survey, but we are unlikely to detect intracluster light in the Wide Survey unless the intracluster stars are young and blue. We conclude that the NISP images are better suited to search for intracluster light in distance clusters and proto-clusters.

Additionally, the intracluster light maps in Figure 3.3 show that the light is not uniform and brighter regions of diffuse emission will appear well above *Euclid*'s detection limits. This will allow detailed measurements of the morphology and colours of the intracluster light.

3.7 Conclusions

We report on the detection of intracluster light within two proto-clusters at $z \sim 2$ using deep *HST* near-infrared images. This extends our understanding of intracluster light to the numerous group-sized haloes that exist at this redshift; previ-

ous measurements focused on the most extreme (and rare) cluster-sized haloes at $z \sim 1.7$ which may not be typical cluster progenitors.

We identified the BCGs of the proto-clusters as the most massive galaxies within the densest regions of the proto-clusters, and measure the amount of diffuse light surrounding these galaxies. We found that the flux of diffuse light between $10-100$ kpc is more than double the flux from within 10 kpc. We showed that this extended morphology is similar to the profiles of BCGs within massive clusters at $1.24 < z < 1.75$ which are known to host intracluster light. Furthermore, this profile differs from the other massive galaxies in the proto-cluster, whose light profiles are at least a factor of 3 more concentrated than the BCGs. Based on these observations, we conclude that the proto-clusters contain significant intracluster light.

We used the colour of the intracluster light to estimate its mass-to-light ratio and calculate the concentration of stellar mass in the core of the proto-clusters. We found that only a quarter to a half of the stellar mass within 100 kpc is located within the central 10 kpc. We combine our data with that of DeMaio et al. (2020b) to show that this low concentration is comparable to that found in similar-sized haloes at lower redshifts, and such low concentrations at $z \sim 2$ are in disagreement with the semi-analytic models of intracluster light by Contini & Gu (2021). Our discovery implies that the formation of the intracluster light began earlier than the $z \sim 1-1.5$ period predicted by these models.

To investigate how this intracluster light could form so early, we compared the stellar mass concentrations in clusters and proto-clusters to that of central galaxies of massive haloes in the Hydrangea hydrodynamical simulations (Bahé et al., 2017). We found that these simulations agree with the trend in the observations: the stellar mass concentration depends on the halo mass, but does not depend on

redshift. Hydrangea also predicts that intra-halo stars are ubiquitous in massive haloes at all redshifts, and even found in haloes with masses as low as $10^{12}\,\mathrm{M}_{\odot}$. We interpret these findings as evidence that pre-processed free-floating stars from accreted haloes is a major contributor to the intracluster light within 100 kpc of clusters and proto-clusters, whilst few of the stars in this region were stripped from orbiting satellite galaxies.

Chapter 4

The luminosity function of spectroscopic confirmed proto-cluster members at $1.3 < z < 2.8$

4.1 Introduction

Galaxy clusters' are of interest to galaxy evolution and cosmology studies. Their properties are related to how structures assemble through time and by studying them we can investigate how galaxies were formed and evolved. Their properties have been extensively studied in the last 100 years (Zwicky, 1933b; Hubble, 1936; Dressler, 1980), but their formation is not fully understood. To know how these structures formed, it is necessary to look at their assembly stages, or their proto-cluster phase because information about their assembly is lost once the structure is virialized. However, deep observations of high redshift proto-clusters is challenging since a large amount of telescope time is needed. This is due to cosmological dimming, in which the surface brightness of sources decreases with redshift. More-

over, proto-clusters occupy a larger area in the sky compared to clusters since they still are in an expanding phase as turnaround is typically reached at about $z \sim 1$ (Muldrew et al., 2015).

In the last years, there has been an effort to detect these structures at high redshifts (Foley et al., 2011; Wylezalek et al., 2013; Gonzalez et al., 2019). The detection of proto-cluster galaxies can be done efficiently using emission lines such as $H\alpha$ and $Ly\alpha$. However, this can bias the selection since these characteristics are found in young galaxies with ongoing star formation. The detection of more evolved systems is more challenging since they have different spectral features compared to star-forming galaxies. Quiescent galaxies usually do not have strong emission lines and their spectra are marked by absorption lines and spectral breaks, such as the Balmer and 4000 Å breaks, as discussed in Chapter 1. Quiescent proto-cluster galaxies can be selected using deep images and photometric redshifts. However, such a selection biases the detection of proto-clusters to more mature systems as star-forming galaxies typically have larger photometric redshift uncertainties than quiescent galaxies. Therefore, the selection method to detect proto-clusters biases the detection of proto-clusters with particular properties. For example, it is unsurprising that proto-clusters detected by Planck contain large excesses of highly star-forming, dusty galaxies, whereas proto-clusters detected through the excess of massive, quiescent galaxies have a high quiescent fraction of galaxies, with a top-heavy stellar mass function. To robustly explore the galaxy properties of proto-clusters, and compare to field galaxies, we need to explore a sample of proto-clusters that were not selected based on their galaxy properties.

Since 1960, people have been investigating the relation of overdensities and radio-sources (Minkowski, 1960; Rogstad et al., 1965). It is now known that radio-loud active galactic nuclei (RLAGN) commonly reside in over-dense environments

(Pentericci et al., 2000; Kurk et al., 2004; Galametz et al., 2012). This led to a new proto-cluster survey that searched for proto-cluster candidates around RLAGN, the *Clusters around radio-loud AGN* (CARLA) survey (Wylezalek et al., 2013). Since the proto-cluster selection was only performed on the basis of a RLAGN, and not an overdensity of galaxies with certain colours, this sample is not bias toward a particular type of proto-cluster system. Therefore, this is the perfect sample to explore the general properties of galaxies within proto-clusters.

The luminosity and mass functions are useful tools to compare groups of galaxies in different environments as it contains information about how the density of galaxies changes with time. The environment of galaxies affects the shape of the luminosity function. This is known from a comparison of the mass/luminosity functions of field and cluster galaxies (van der Burg et al., 2013, 2020). The shape of the luminosity function varies for different types of galaxies (Binggeli et al., 1988), and the relative proportion of different types of galaxies in clusters and field result in different total luminosity/mass functions. Clusters also have an excess of very massive galaxies compared to the field.

What is not clear from the literature is where the causality of these differences come from. For example, does environmental quenching of a subset of galaxies within the main halo of the cluster cause the mass/luminosity function to change? Or does the denser proto-cluster environment in which the galaxies formed cause the mass/luminosity functions to deviate from the field, which then leads to a different quenched fraction through enhanced mass-quenching?

In this work, we explore this knowledge gap by measuring the luminosity function and stellar ages of galaxies in proto-clusters and comparing them to field galaxies selected by the same method. We re-analyze 20 CARLA proto-clusters at $1.3 < z < 3.0$ from Noirot et al. (2018). Our initial task is to identify all proto-

cluster galaxies, both star-forming and passive galaxies and use them to calculate the luminosity functions. Although we use the same sample as described in Noirot et al. (2018) and Wylezalek et al. (2014), a different methodology is used to locate proto-cluster members. In Wylezalek et al. (2014), the proto-cluster membership selection was done using Spitzer IRAC colours. Specifically, they defined members as galaxies detected in IRAC2 above 95% of completeness limit and have colours of $[3.6] - [4.5] > -0.1$. Noirot et al. (2018) used HST grism data and selected by eye proto-cluster galaxies with strong emission lines that placed them at the same redshift as the RLAGN. This method excludes continuum galaxies from the sample. Here we do a different membership selection. By using the *Grism redshift & line analysis software for space-based slitless spectroscopy* (Brammer, 2019), also known as `Grizli`, we perform SEDs fits for all galaxies in the field of view. This means we select not only emission line galaxies, but quiescent galaxies within the proto-cluster.

In Section 4.2, we describe the data, and how it was processed. In Section 4.3, we explain how we classified galaxies as proto-cluster galaxies and created luminosity functions. The RA and DEC maps, tables with memberships and luminosity functions are shown in Section 4.4. We discuss our findings in Section 4.5.

4.2 Data

The proto-clusters used in this work were found as galaxy overdensities around RLAGN that were observed with *Spitzer* (Wylezalek et al., 2013; Wylezalek et al., 2014). We use the HST photometry and grism spectroscopy follow-up from this parent sample of 20 galaxy proto-clusters candidates at $1.3 < z < 3.0$, previously

described in Noirot et al. (2018), see Table 4.1. These are some of the proto-cluster candidates with the largest Spitzer galaxies overdensities within the CARLA survey. In all the observations there is a radio-loud AGN, in which 10 are quasars and the other 10 are radio galaxies. Throughout the paper we use WFC3/F140W images for photometry and WFC3/G141 grism spectra observed between 2014 and 2016. Each field was observed twice with different orientations, with a total exposure time of $0.5\,ksec$ for the images and $2.0\,ksec$ for spectra (HST proposal ID: 13740).

Table 4.1: 20 CARLA cluster candidates. The positions correspond to the RLAGN RA and DEC. We show the redshifts for the RLAGN and for the mean of member galaxies. The significance of the IRAC overdensity is shown as σ_{IRAC}. N_n is the number of member galaxies estimated by Noirot et al. (2018) and N is the number of members estimated by this work. Galaxy proto-clusters with * have overdensity> 1 and only galaxies in these clusters are considered as members.

Cluster	RA (deg)	DEC (deg)	z_{RLAGN}	z_{cl}	σ_{IRAC}	N_n	N
CARLA J01162052*	19.214	-20.868	1.417	1.425	5.14	13	13
CARLA J0800+4029	120.067	40.498	2.004	1.986	6.38	10	8
CARLA J09582904	149.520	-29.068	1.411	1.392	5.00	8	10
CARLA J1017+6116	154.357	61.274	2.80	2.801	6.67	7	1
CARLA J1018+0530*	154.616	5.508	1.949	1.952	5.00	8	10
CARLA J1052+0806	163.132	8.102	1.641	1.646	4.71	6	5
CARLA J1103+3449	165.859	34.829	1.444	1.442	6.38	8	12
CARLA J1129+0951*	172.308	9.866	1.520	1.528	6.33	12	11
CARLA J11312705*	172.765	-27.088	1.444	1.446	4.38	9	15
CARLA J1300+4009*	195.138	40.152	1.669	1.675	4.86	8	10
CARLA J1358+5752*	209.573	57.867	1.370	1.368	6.24	14	24
CARLA J1510+5958	227.524	59.981	1.719	1.725	5.62	6	8
CARLA J1753+6310*	268.397	63.180	1.576	1.582	4.52	5	8
CARLA J20392514*	309.851	-25.241	1.997	1.999	8.00	9	12
CARLA J22272705*	336.930	-27.083	1.684	1.692	5.29	7	8
CARLA J23550002*	358.904	-0.049	1.487	1.490	5.62	12	20
6CSS1054+4459	162.133	44.741	2.573	2.566	4.67	2	3
J1317+3925	199.329	39.424	1.569	1.574	4.86	3	3
J1515+2133	228.787	21.563	2.249	2.262	4.24	2	4
TNR 2254+1857	343.725	18.951	2.164	2.159	5.62	3	6

Unlike in Noirot et al. (2016), the data were processed using the *Grism redshift & line analysis software for space-based slitless spectroscopy* (Brammer, 2019), also known as `Grizli`, using the method described in Matharu et al. (2021), which we describe briefly here. `Grizli` was used to obtain information of all objects in each CARLA field with $F140W < 26$ and $S/N > 7$. For all frames, the sky was estimated and subtracted, cosmic rays and hot pixels removed, and divided by the master flat-field. Using the `calwf3` pipeline (Brammer, 2016), there is a correction of variable backgrounds that can result in observations taken at different times of the day. In most of the cases, this effect can be seen in grism G141 due to the presence of helium in the atmosphere. Hot pixels and cosmic rays are detected

and removed by `Grizli` and also by AstroDrizzle (Gonzaga et al., 2012). The flat-fielding for the G141 grism is done using the F141W calibration image. Using the procedure previously described in Brammer et al. (2015), a 'master sky' is estimated and removed from the data.

For each spectrum there is a contamination analysis in which there is an automatic removal of possible contaminant objects that are nearby the galaxy. `Grizli` generates 1D and 2D spectra.

4.3 Methodology

4.3.1 Redshifts and emission lines

The redshift of each extracted object spectrum is estimated by fitting the grism spectra using stellar population templates. The fit is done using the templates of the *Flexible Stellar Population Synthesis models* (Conroy et al., 2009; Conroy & Gunn, 2010), in which there are several templates for different types of galaxies. The template is used to fit the spectrum of each galaxy over the selected redshift range. The final redshift and templates selected for each object is the one that results in the minimal χ^2 estimated from the data and model. Through this process, we select the optimal combination of the continuum and emission line templates that fit each spectrum. The emission line fluxes are then estimated from the chosen templates. A more detailed description of this process is available in Simons et al. (2021). Considering the RLAGN redshifts, in the wavelength range used, the emission lines of $H\alpha$, $H\beta$, [OII] and [OIII] could be detected in the proto-cluster members.

4.3.2 Member and field selection

For each proto-cluster target, we identified the proto-cluster members and 'field' galaxies that lie in the same redshift range as other RLAGN in our sample. Each object has a redshift probability distribution function, which we integrated over certain limits to give the probability that the object resides in a particular redshift range that encompasses the proto-cluster redshift estimate from Noirot et al. (2018). We define a galaxy as a proto-cluster member if it satisfies 2 criteria: (1) it has probability greater than 10% of being in the redshift interval of $z_{cluster} - 0.02 < z_{cluster} < 0.02 + z_{cluster}$ and (ii) it has a best fit grism redshift with $z_{grism} < |z_{cluster} + 0.1|$.

We use the same data of the 20 targets to define a field galaxy sample that is selected in exactly the same way as the proto-clusters member candidates. Therefore, field candidates are selected from the other 19 fields for the clusters in target to have $z_{grism} < |z_{cluster} + 0.1|$ and have $> 10\%$ of probability of lying in the redshift interval selected. The 10% threshold is used since in Figure 4.24 shows that it gives qualitatively the same results as 30 and 50%, and at the same time returns a larger sample. We define a field population for each of the 20 proto-cluster candidates. We take care to exclude fields that have proto-clusters at a similar redshift as the one being considered. So we only use a target to select field galaxies when $z_{field} > |z_{cluster} + 0.2|$, where z_{field} is the redshift of the field galaxies we are interested in, and $z_{cluster}$ is the redshift of the known cluster in the observations.

4.3.3 Removing poor spectral fits

We then checked by eye each best fit of the galaxy spectra. We removed from the sample the spectra with contamination from other close objects (see Figure

4.2), spectra with poor model fitting, those that are too noisy or with very large error bars. We generated a catalogue in which galaxies with poor spectra are classified with $Flag = 1$. We show examples of removed spectra in Figure 4.1. From the proto-cluster member sample, 34 galaxies were excluded, and from the field sample, 97 galaxies.

4.3.4 Emission line and continuum

We cannot determine whether a galaxy is forming stars or passively evolving from the grism spectra alone, but we can classify galaxies as either emission line or continuum only. Emission line galaxies are likely to be active, either due to hosting star-formation or and AGN. Galaxies with no emission lines may be passively evolving, or the wavelength coverage of the grism data does not encompass any strong emission lines.

We measured the maximum emission line S/N for each spectrum. We used the flux values estimated by `Grizli` for different emission lines. In the .full file generated by `Grizli`, we extracted from the header the flux and its error for each emission line found in the wavelength range observed. For each emission line in each galaxy, we divided the value by its error to estimate the S/N value. Each galaxy will have a list of S/N, one for each line. We define the S/N_{max} as the highest value in this list, or the S/N of the most prominent emission line.

4.3.5 Luminosity functions

The flux of each galaxy was estimated from the F140W magnitude using $\mathrm{Flux} = 10^{-\frac{48.60+\mathrm{m}}{2.5}}$ and converted to the rest-frame, $\mathrm{Flux_{rest}} = \frac{\mathrm{Flux}}{1+\mathrm{z}}$. Finally, the luminosity of the galaxy was calculated from $\mathrm{Lum} = \mathrm{Flux_{rest}} \times 4\pi \times \mathrm{distance}$,

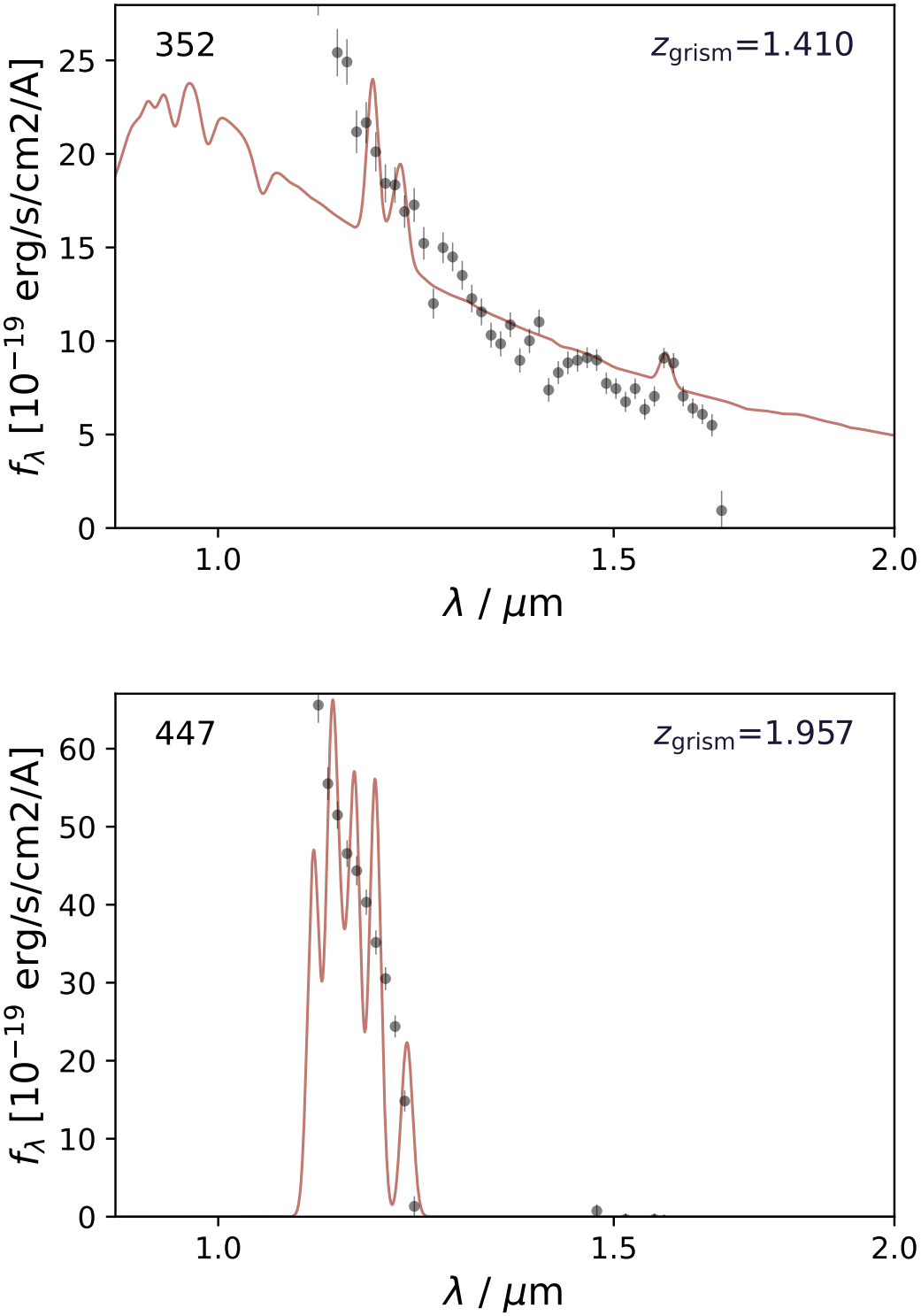

Figure 4.1: Examples of galaxies that were removed from the sample for having poor spectra. The top one is galaxy 352 of CARLA J011652-2052 and the bottom one is galaxy 447 of CARLA J101828+0530. The points are the observed grism spectra and the solid lines are the best fit templates. The number in the top left is the ID of the galaxy and the number in top right is the redshift estimated for the galaxy. Both spectra have large levels of contamination.

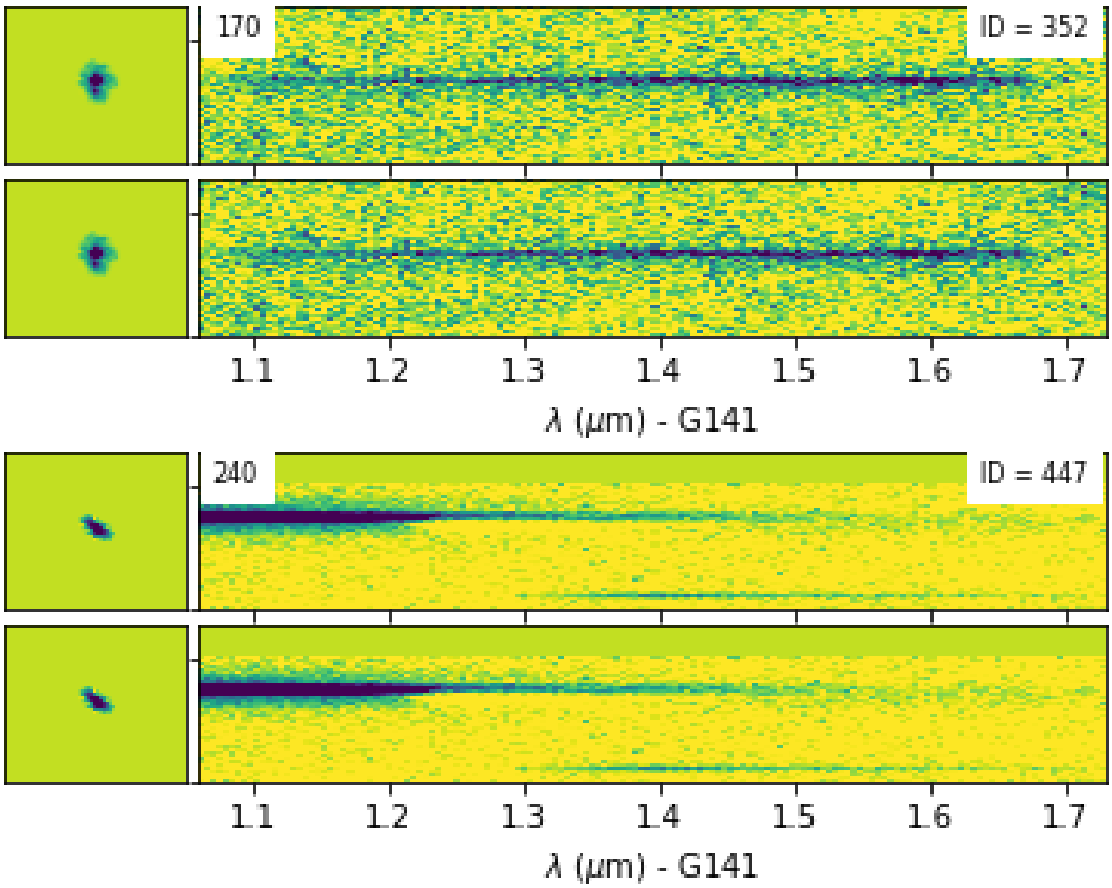

Figure 4.2: Examples of galaxies that were removed from the sample for having poor spectra. We can see that both of them have contamination. The top one has an excess of light on the bottom left part of the spectrum. The bottom one has a parallel line in the bottom of the spectrum.

in which the luminosity distance was estimated using the grism redshift of the galaxy and the astropy cosmological calculator. To convert to solar luminosities, we estimate the luminosity of the Sun using $\text{Flux} = 10^{-\frac{48.60+\text{m}}{2.5}}$, in which m is -26.52, this value comes from Willmer (2018) which is the magnitude of the Sun in the $LSST_g$ filter.

We measure the number of galaxies per area for each luminosity bin. The area of each field is $4.6\,arcmin^2$, to estimate the area for the proto-clusters we multiply the value by 10, which is the number of clusters with $overdensity > 1.0$. To select field galaxies, for each cluster, we select a sample of galaxies from the other fields

that are not in the redshift of the cluster considered. Due to that, 64 galaxies are repeated and the same field is considered many times. For example, consider that we have the images A, B, C, D. In this case, the proto-clusters in fields A and B have similar redshifts. To get field galaxies for proto-cluster A, we have to get the galaxies from the other proto-clusters images, which included B, C and D. However, when we do the same for cluster B, we will have C and D in common, so fields C and D will be counted more than one time. To estimate the area, we consider the total number of fields, including repetitions, which is 63 in total and we multiply it by $4.6\,arcmin^2$. The error bars are the square root of the number of galaxies per each bin.

4.4 Results

4.4.1 Proto-cluster maps and members

With `Grizli`, we obtain a redshift for every object in the field of view, but Noirot et al. (2018)'s method only provided redshifts for 707 sources with emission lines. Our proto-cluster membership catalogue contains 131 member galaxies, whereas only 67 galaxies are present in the catalogue provided by Noirot et al. (2018). There are 64 member galaxies in our catalogue that are not present in Noirot's catalogue, but there is 1 proto-cluster member in Noirot's galaxy catalogue that is not in ours (considering only the proto-clusters candidates with $overdensity > 1$). In addition there are 17 galaxies in their catalogue that are not in our catalogue, of which 6 are classed as A, 11 are classified as B-. Moreover, `Grizli` does not fit well AGN templates, so possibly we are losing AGN in our sample. While `Grizli` fit to the ID combined spectra, Noirot et al. (2018) visually inspected

each orientation separetely, which can affect the differences in the samples. To understand this discrepancy between the full catalogues, we explored the S/N of the emission lines in our samples, the S/N distributions of galaxies only in our sample (black) and galaxies that are also in Noirot's sample (blue) are shown in Figure 4.3. Most of the galaxies that were not selected by Noirot et al. (2018) have small S/N, which means that most of our new sample have weaker emission lines. Figure 4.3 also shows a population of 8 galaxies with $S/N > 50.0$ and a different distribution, these objects were all classified by Noirot et al. (2018) as AGN.

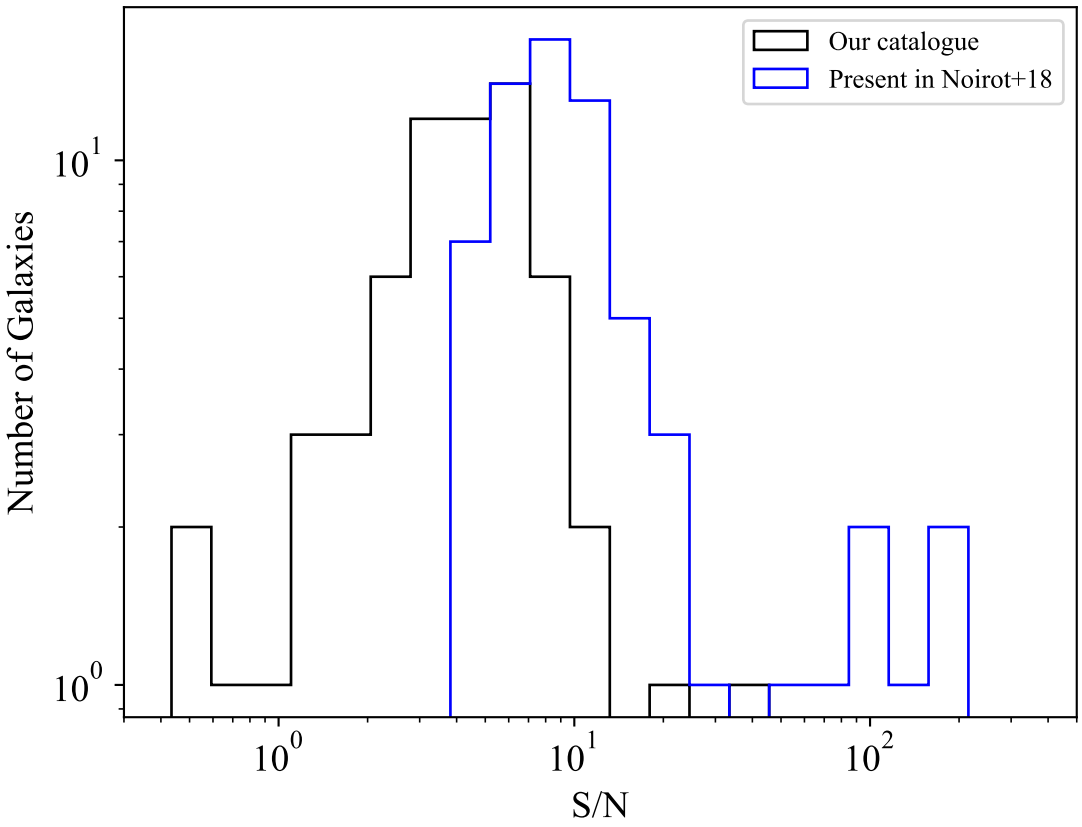

Figure 4.3: S/N distribution for member galaxies. In black we show the number of galaxies per S/N for galaxies only present in our catalogue. In blue, we show galaxies that our catalogue have in common with the catalogue presented in Noirot et al. (2018).

In order to select the known proto-cluster candidates, we define the galaxy

overdensity of each field as $N_m/N_f - 1$, where N_m is the number of members in each candidate proto-cluster, and N_f is the number of field galaxies divided by the number of target fields used to select field candidates. We define proto-clusters as targets with overdensity larger than 1. In total, we have 10 proto-cluster candidates, these are tagged with * in Table 4.1. From these 10 targets we select 131 proto-cluster galaxies.

Comparing our full catalogue of 9768 galaxies with Noirot et al. (2018), we find 690 galaxies of 707 of their catalogue if we match catalogues up to 1″. Of these 17 galaxies they have that we do not find, 7 are in cluster candidates with *overdensity* < 1 and 4 are field galaxies. Only 6 galaxies were galaxies with $|z_{cl} - z_{gal}| < 0.1$. We find 697 galaxies if we include matches up to 3″ of separation. Of these 11 we could not find only 4 are proto-cluster galaxies, the other are field galaxies or in fields that we found *overdensity* < 1. This small mismatch is probably due to how the data was reprocessed, which generated a small difference in the object detection.

For each field, we present the $F140W$ image with the candidate members marked in Figures 4.4-4.23. We mark galaxies that have different probabilities of being a proto-cluster member in different colours. In total we have 131 members with probabilities larger than 10%, 14 with probabilities between 10 and 20%, 5 between 20 and 30% and 112 with probabilities higher than 30%. In the maps, galaxies in red circles have probabilities higher than 30% of being in the redshift of the RLAGN, green between 20-30% and blue between 10-20%. The purple diamond is the RLAGN which is not always counted as a proto-cluster member, but we include it in the table. The IDs of the galaxies are also shown.

The Tables 4.2-4.21 show the member candidates for each field. In each table we list the galaxies' IDs from our catalogue, the associate IDs for the Noirot et al.

ID	IDn	RA (deg)	DEC (deg)	mag	z	Prob	S/N
206	437	19.2143	-20.8686	20.32	1.42	1.0	136.26
347	-	19.2183	-20.8586	22.12	1.43	0.82	3.46
328	398	19.2108	-20.8597	23.30	1.43	1.0	7.12
356	45	19.2318	-20.8582	20.94	1.42	1.0	22.55
291	-	19.2132	-20.8626	22.89	1.43	0.74	7.87
363	-	19.2329	-20.8577	20.96	1.42	0.86	6.39
324	-	19.2275	-20.8602	23.06	1.42	0.78	5.03
246	289	19.2070	-20.8658	23.31	1.41	1.0	6.44
365	705	19.2205	-20.8575	21.22	1.43	1.0	19.5
260	-	19.2121	-20.8651	22.10	1.41	0.24	3.98
368	922	19.2018	-20.8571	22.41	1.43	0.99	12.85
326	380	19.2102	-20.8599	23.93	1.43	1.0	12.22
249	865	19.2049	-20.8657	22.55	1.41	0.42	5.83

Table 4.2: Member candidates for CARLA J011652-2052. The ID is the id for our catalogue. IDn is the id for the Noirot et al. (2018) catalogue, if the galaxy is present in their catalogue. For each galaxy, we show the right ascension and declination in degrees, the redshift, probability of being in the redshift of the RLAGN and maximum S/N.

(2018) catalogue, right ascension in degrees, declination in degrees, grism redshift, probability of being at the same redshift as the AGN, and the maximum S/N for the emission lines (if present). For proto-cluster members, we found that 9% have strong emission lines ($S/N > 30$), 45% have $S/N > 6$ and 55% galaxies have $S/N < 6$. For the field, 8% have strong emission lines, 39% have $S/N > 6$ and 61% have $S/N < 6$.

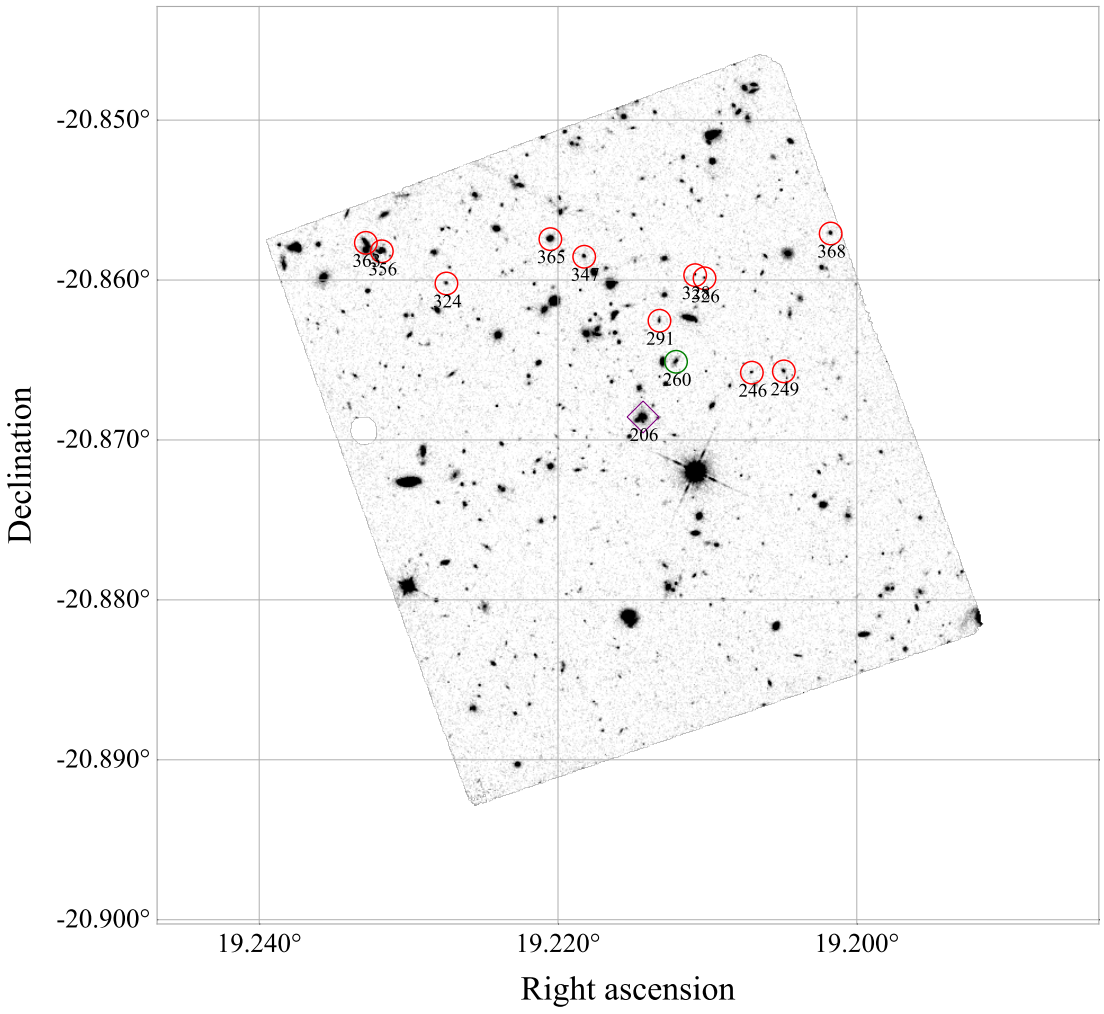

Figure 4.4: The *HST F*140*W* image of CARLA J011652-2052 with marked proto-cluster galaxies. Different colours mean different probabilities of being in the RLAGN redshift. Red circles mean more than 30%, green circles 20-30% and blue circles 10-20%. The RLAGN is inside the purple diamond. The ID of each galaxy is also shown.

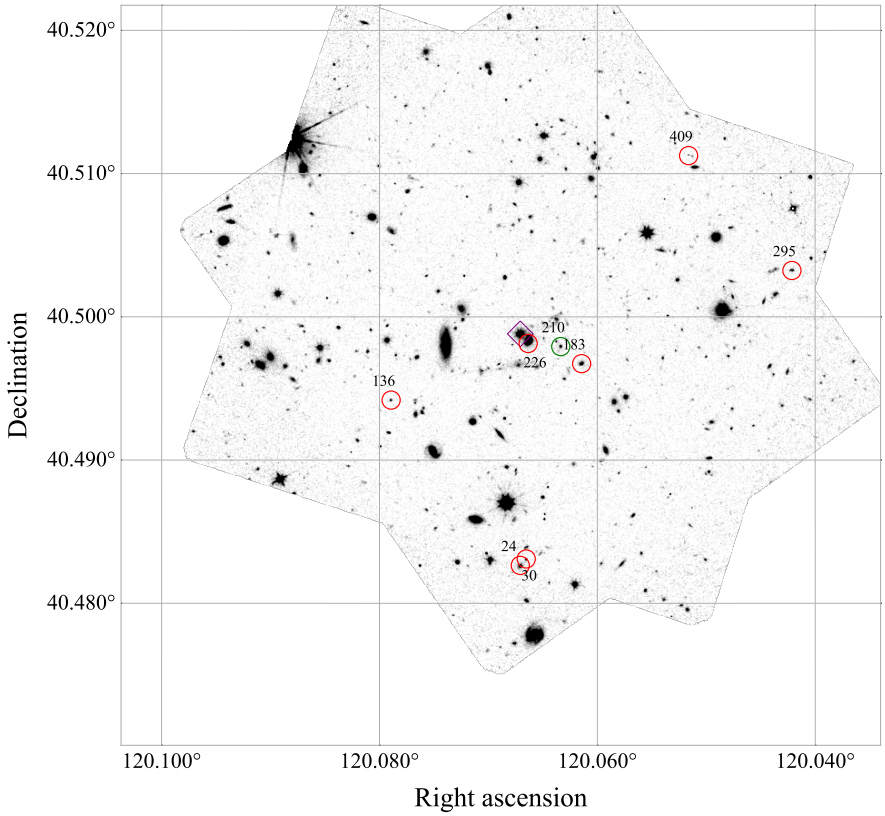

Figure 4.5: The *HST F*140*W* image of CARLA J080016+4030 with marked protocluster galaxies. Symbols as described in Figure 4.4.

ID	IDn	RA (deg)	DEC (deg)	mag	z	Prob	S/N
409	146	120.0516	40.5112	24.90	1.99	0.98	8.06
24	749	120.0671	40.4826	21.38	2.00	1.00	31.47
210	-	120.0634	40.4979	22.66	1.98	0.27	2.90
183	436	120.0615	40.4967	21.67	1.97	1.00	10.96
30	-	120.0666	40.4831	23.51	1.99	0.88	4.35
136	767	120.079	40.4942	23.37	1.98	0.85	6.20
295	-	120.0422	40.5032	22.91	1.97	0.84	6.76
226	372	120.0664	40.4981	20.64	2.00	0.97	21.12

Table 4.3: Member candidates for CARLA J080016+4030. Columns as listed in Table 4.2.

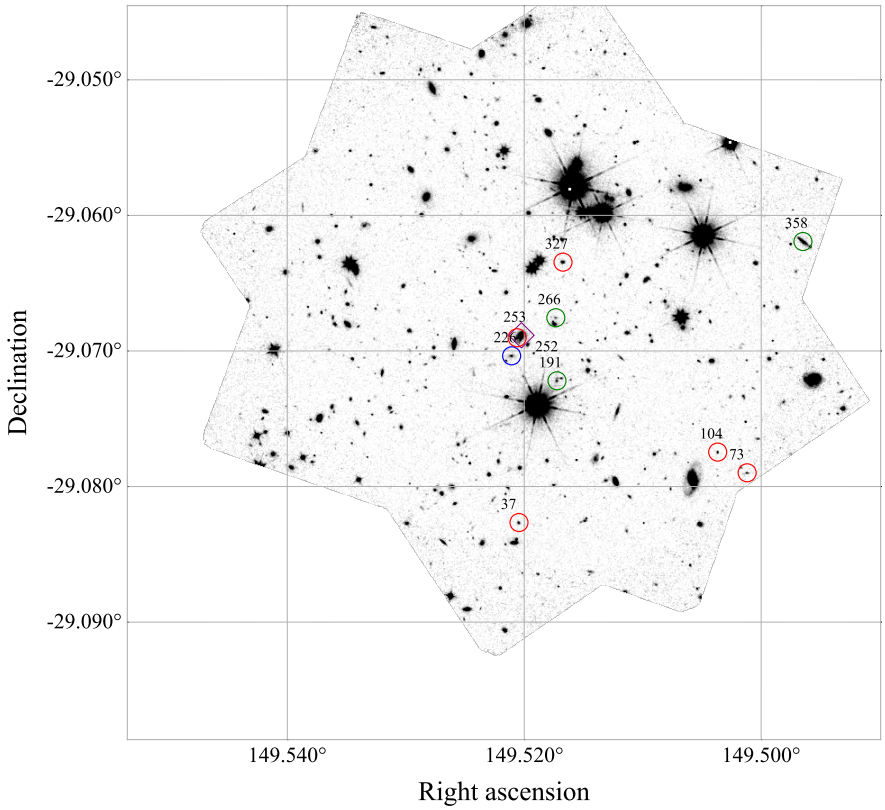

Figure 4.6: The *HST F140W* image of CARLA J095804-2904 with marked proto-cluster galaxies. Symbols as described in Figure 4.4.

ID	IDn	RA (deg)	DEC (deg)	mag	z	Prob	S/N
191	-	149.5173	-29.0722	23.08	1.38	0.25	6.12
252	405	149.5206	-29.069	21.88	1.40	1.00	39.56
104	691	149.5037	-29.0775	23.31	1.38	1.00	7.69
358	-	149.4965	-29.0619	21.20	1.39	0.22	3.32
226	-	149.5211	-29.0704	22.65	1.41	0.15	6.03
73	-	149.5012	-29.079	23.33	1.40	0.38	2.65
37	260	149.5205	-29.0827	22.93	1.38	1.00	11.85
253	406	149.5203	-29.0689	19.75	1.41	1.00	196.08
266	-	149.5174	-29.0676	23.42	1.40	0.21	3.30
327	578	149.5167	-29.0635	22.03	1.38	1.00	27.15

Table 4.4: Member candidates for CARLA J095804-2904. Columns as listed in Table 4.2.

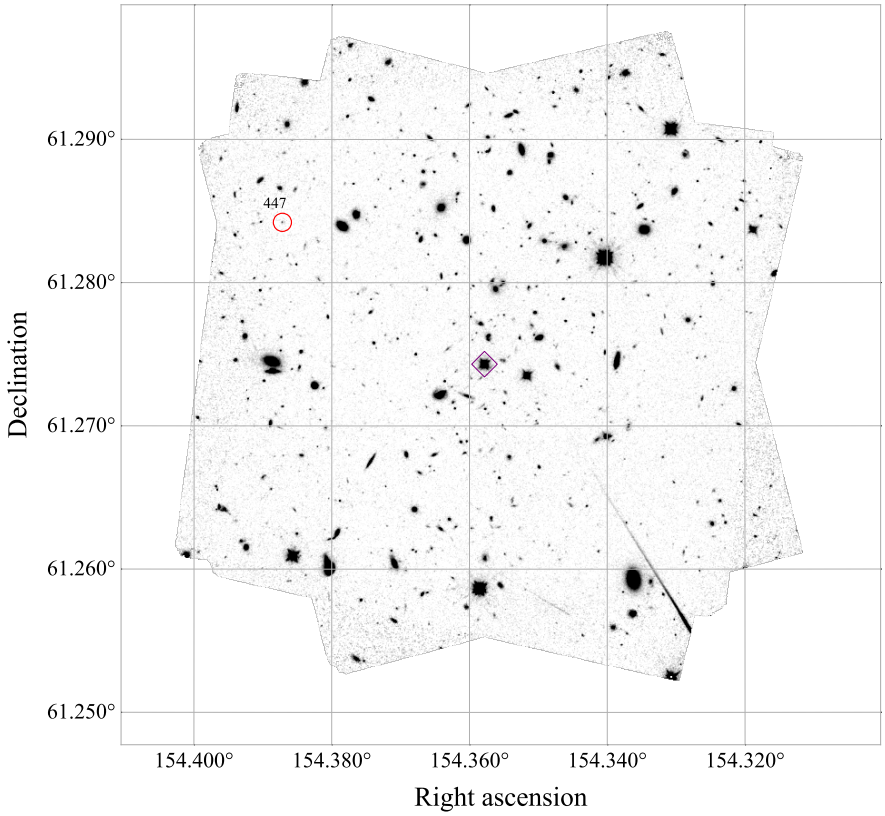

Figure 4.7: The *HST F*140*W* image of CARLA J101724+6116 with marked protocluster galaxies. Symbols as described in Figure 4.4.

ID	IDn	RA (deg)	DEC (deg)	mag	z	Prob	S/N
447	-	154.3872	61.2842	24.43	2.82	0.32	3.36

Table 4.5: Member candidates for CARLA J101724+6116. Columns as listed in Table 4.2.

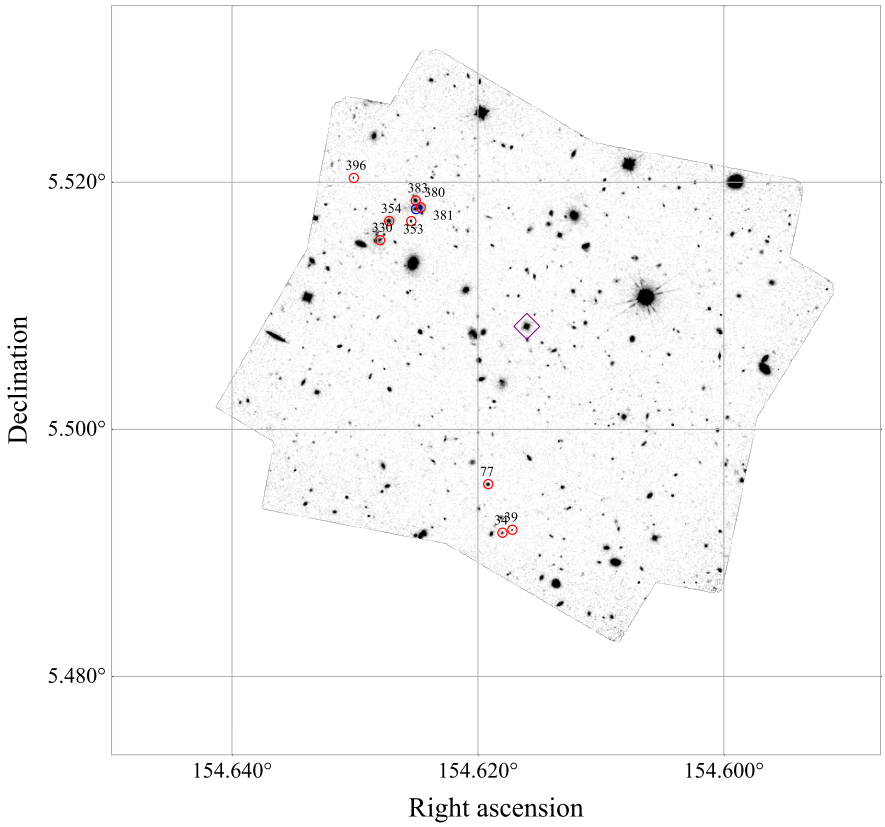

Figure 4.8: The *HST F*140*W* image of CARLA J101828+0530 with marked proto-cluster galaxies. Symbols as described in Figure 4.4.

ID	IDn	RA (deg)	DEC (deg)	mag	z	Prob	S/N
354	-	154.6272	5.5168	21.61	1.96	0.83	1.85
380	-	154.625	5.5178	21.58	1.99	0.12	6.48
396	336	154.6301	5.5203	24.11	1.96	1.00	10.14
353	-	154.6254	5.5168	23.11	1.96	0.36	3.19
34	138	154.618	5.4916	23.27	1.96	0.95	5.35
39	162	154.6172	5.4919	24.20	1.95	1.00	13.60
381	-	154.6247	5.518	21.01	1.95	1.00	6.15
330	-	154.628	5.5153	21.83	1.97	0.56	6.86
383	-	154.6251	5.5185	21.54	1.97	0.49	1.06
77	-	154.6192	5.4956	21.89	1.94	0.88	1.87

Table 4.6: Member candidates for CARLA J101828+0530. Columns as listed in Table 4.2.

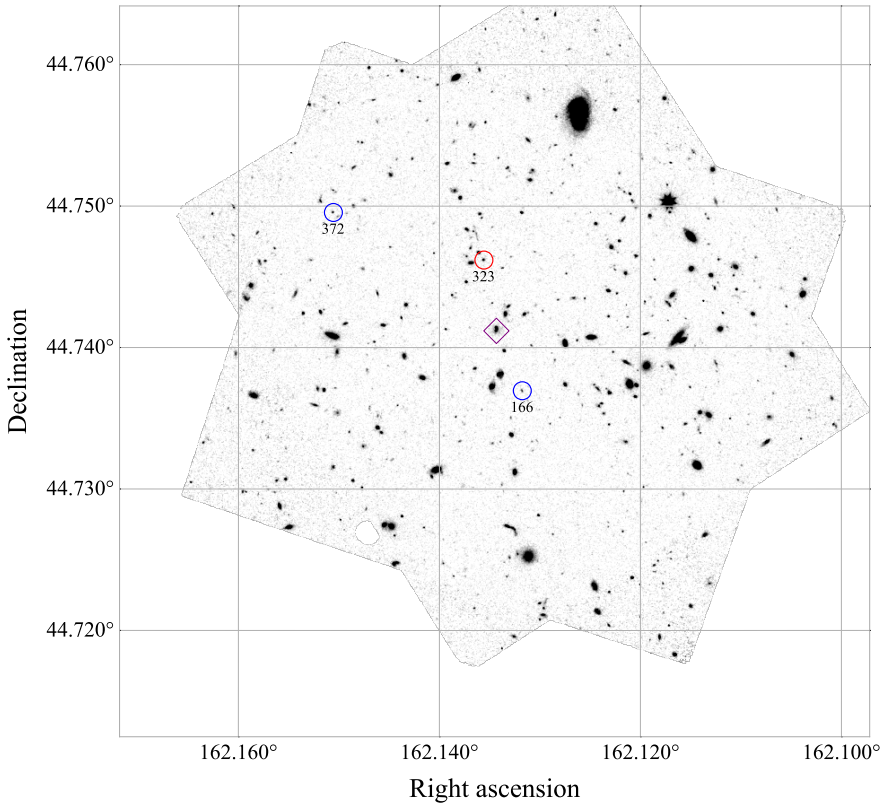

Figure 4.9: The *HST F*140*W* image of CARLA J104832+4444 with marked protocluster galaxies. Symbols as described in Figure 4.4.

ID	IDn	RA (deg)	DEC (deg)	mag	z	Prob	S/N
323	-	162.1356	44.7462	23.08	2.56	0.31	2.71
166	-	162.1318	44.7369	23.87	2.57	0.19	4.92
372	-	162.1506	44.7495	23.79	2.60	0.10	4.76

Table 4.7: Member candidates for CARLA J104832+4444. Columns as listed in Table 4.2.

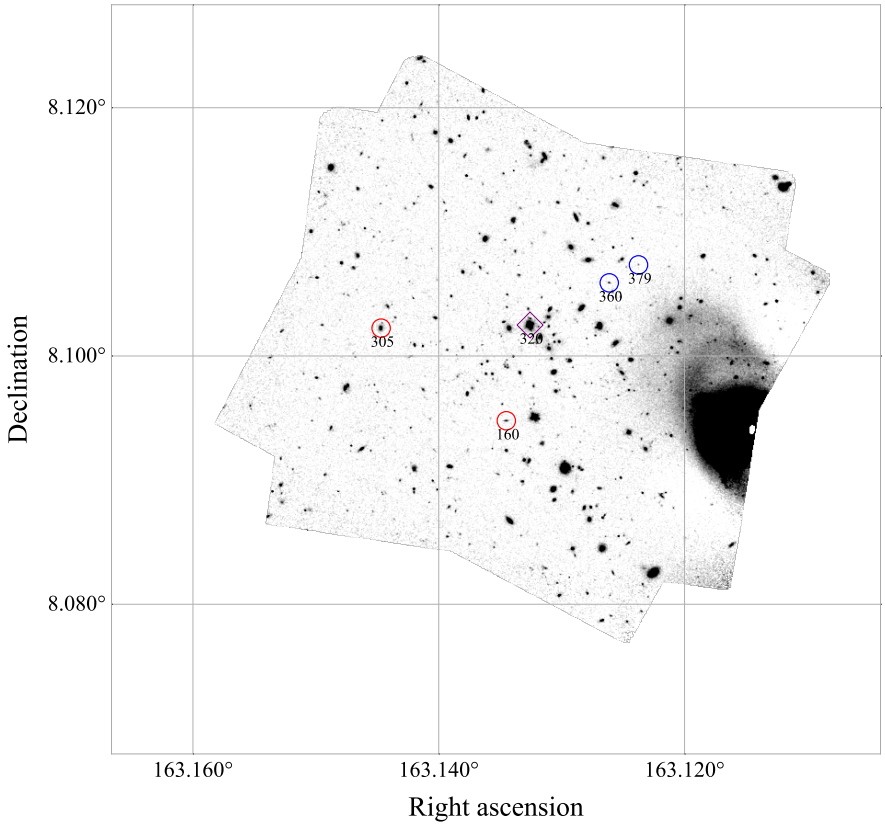

Figure 4.10: The *HST F140W* image of CARLA J105232+0806 with marked proto-cluster galaxies. Symbols as described in Figure 4.4.

ID	IDn	RA (deg)	DEC (deg)	mag	z	Prob	S/N
160	-	163.1345	8.0948	23.21	1.66	0.37	4.41
320	338	163.1326	8.1025	18.39	1.64	1.00	108.41
305	-	163.1447	8.1022	21.3	1.64	0.75	0.86
379	-	163.1238	8.1073	24.77	1.66	0.16	3.79
360	-	163.1261	8.1059	23.73	1.63	0.16	3.22

Table 4.8: Member candidates for CARLA J105232+0806. Columns as listed in Table 4.2.

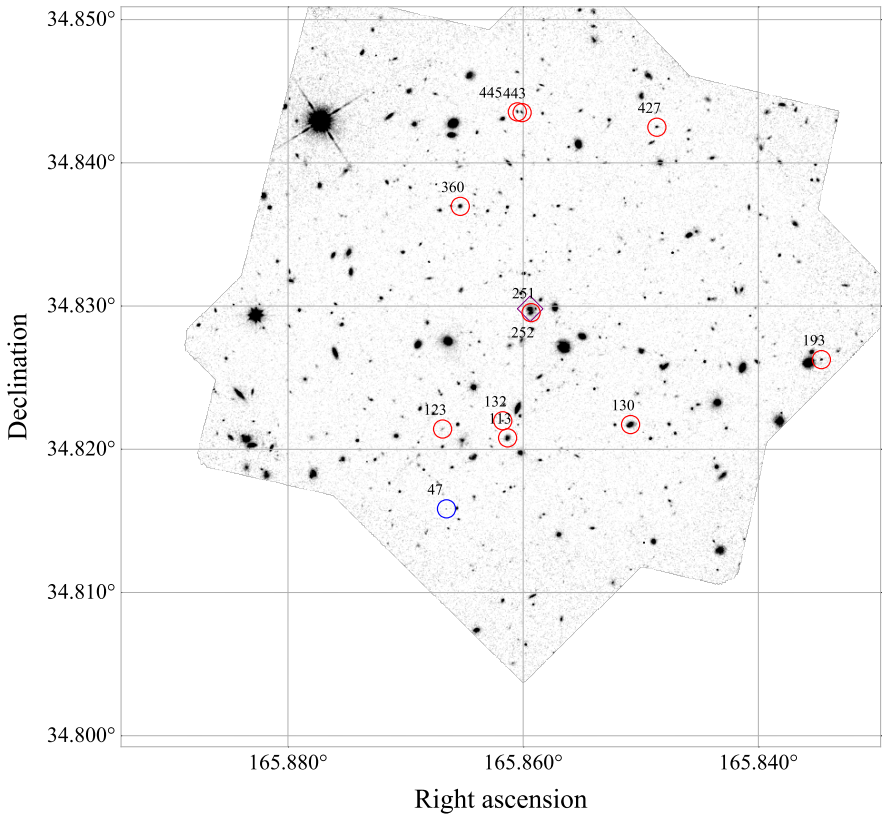

Figure 4.11: The *HST F140W* image of CARLA J110328+3450 with marked proto-cluster galaxies. Symbols as described in Figure 4.4.

ID	IDn	RA (deg)	DEC (deg)	mag	z	Prob	S/N
130	199	165.8509	34.8217	21.31	1.44	0.99	10.37
113	-	165.8613	34.8208	22.10	1.42	0.42	5.33
445	279	165.8605	34.8435	23.56	1.44	1.00	12.72
251	-	165.8593	34.8295	21.31	1.45	0.32	4.65
427	-	165.8486	34.8425	23.39	1.44	1.00	7.30
132	-	165.8618	34.822	24.28	1.45	0.39	4.53
123	-	165.8669	34.8214	24.53	1.44	0.50	4.27
193	93	165.8347	34.8262	23.64	1.45	1.0	8.48
47	-	165.8665	34.8158	25.52	1.44	0.15	2.95
252	491	165.8594	34.8298	20.77	1.44	1.00	63.03
360	320	165.8654	34.8369	22.06	1.44	0.86	6.27
443	283	165.8601	34.8435	23.39	1.44	1.00	13.74

Table 4.9: Member candidates for CARLA J110328+3450. Columns as listed in Table 4.2.

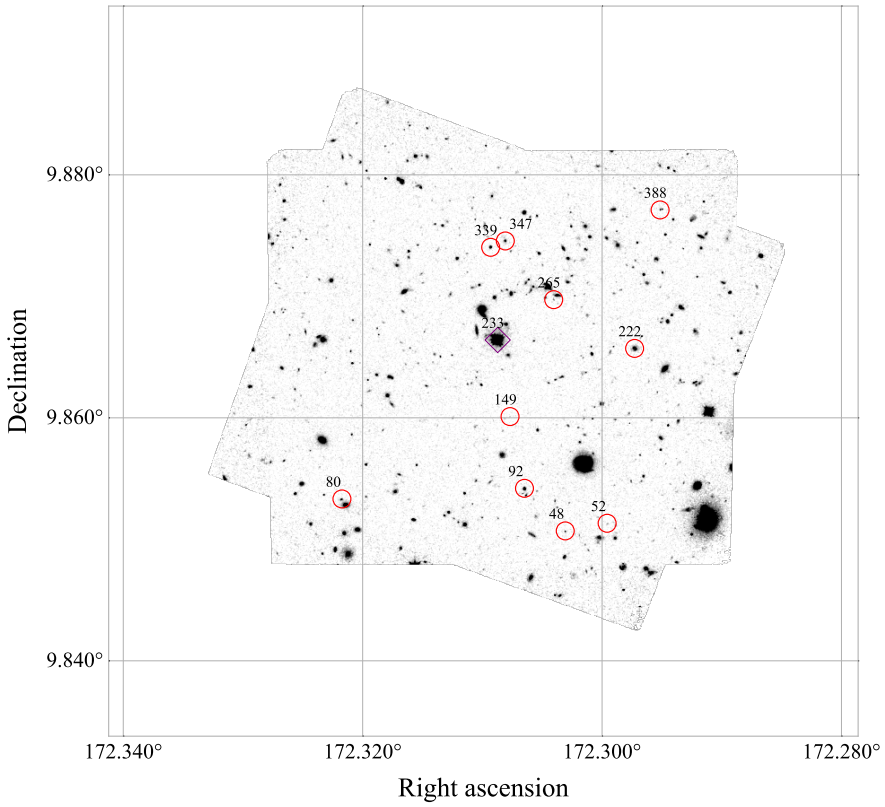

Figure 4.12: The *HST F140W* image of CARLA J112916+0952 with marked proto-cluster galaxies. Symbols as described in Figure 4.4.

ID	IDn	RA (deg)	DEC (deg)	mag	z	Prob	S/N
265	-	172.3041	9.8697	24.67	1.52	0.51	4.82
80	126	172.3218	9.8533	23.13	1.53	1.00	9.06
48	674	172.3031	9.8507	24.25	1.52	1.00	4.90
388	805	172.2952	9.8771	23.92	1.54	0.87	5.33
92	607	172.3065	9.8542	22.01	1.53	0.98	19.58
222	335	172.2973	9.8657	21.32	1.52	1.00	27.05
233	377	172.3087	9.8664	16.83	1.52	1.00	77.93
52	637	172.2996	9.8513	25.04	1.52	1.00	5.69
149	565	172.3077	9.8601	25.88	1.54	0.89	8.43
339	261	172.3093	9.874	22.41	1.54	0.92	4.00
347	240	172.3081	9.8745	22.63	1.54	1.00	14.91

Table 4.10: Member candidates for CARLA J112916+0952. Columns as listed in Table 4.2.

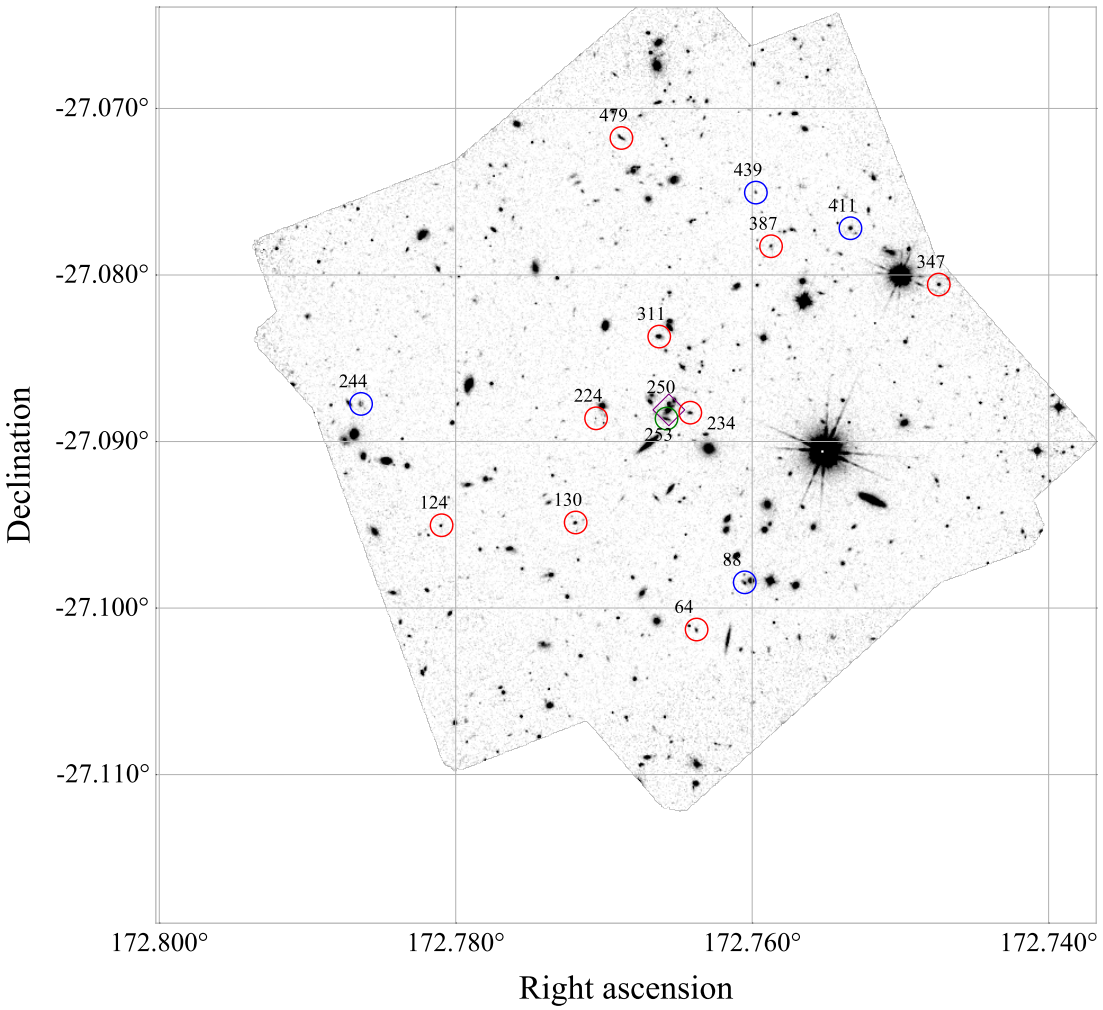

Figure 4.13: The *HST F140W* image of CARLA J113104-27052 with marked proto-cluster galaxies. Symbols as described in Figure 4.4.

ID	IDn	RA (deg)	DEC (deg)	mag	z	Prob	S/N
479	-	172.7688	-27.0718	22.68	1.47	0.55	7.68
224	389	172.7705	-27.0886	24.97	1.45	1.00	9.45
88	-	172.7605	-27.0985	22.62	1.47	0.12	4.89
244	-	172.7864	-27.0878	22.97	1.46	0.16	4.51
64	712	172.7638	-27.1013	23.37	1.44	0.99	6.32
411	-	172.7534	-27.0772	22.07	1.43	0.17	3.94
250	447	172.7656	-27.0881	20.66	1.44	1.00	52.99
311	504	172.7663	-27.0837	22.11	1.44	1.00	10.31
347	115	172.7474	-27.0806	22.91	1.44	0.91	12.21
253	-	172.7658	-27.0886	22.01	1.44	0.22	4.94
439	-	172.7598	-27.0751	23.98	1.47	0.15	3.54
387	701	172.7587	-27.0783	23.33	1.44	0.38	5.53
234	-	172.7642	-27.0883	22.93	1.45	0.72	6.75
124	-	172.781	-27.095	23.51	1.44	0.66	3.94
130	747	172.7719	-27.0949	23.09	1.45	0.73	4.73

Table 4.11: Member candidates for CARLA J113104-2705. Columns as listed in Table 4.2.

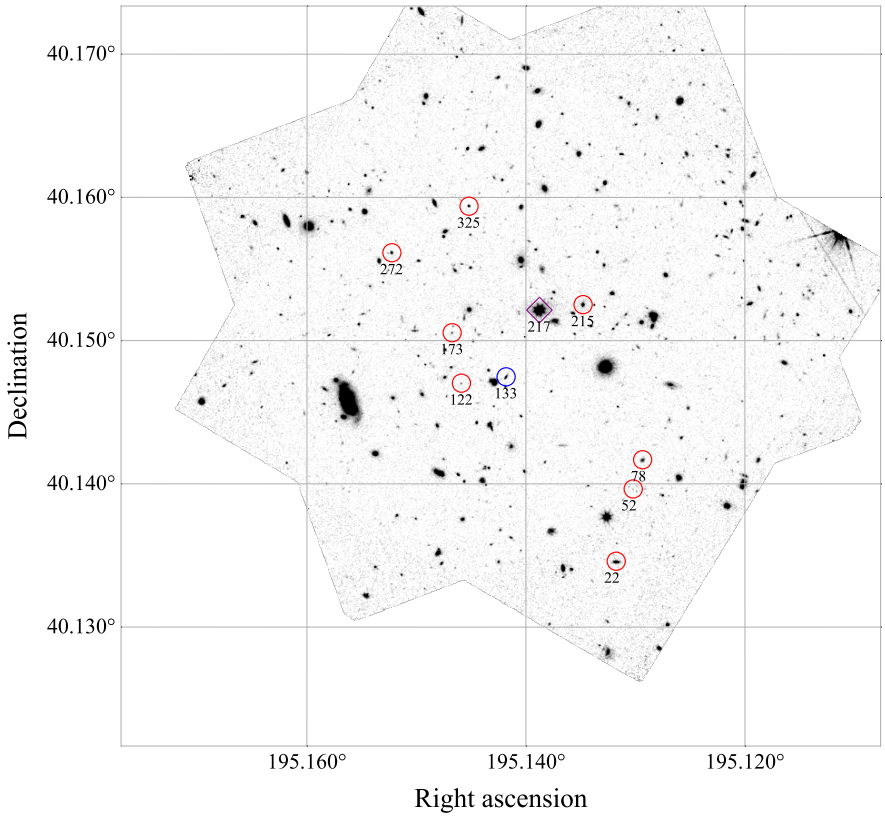

Figure 4.14: The *HST F140W* image of CARLA J130032+4009 with marked proto-cluster galaxies. Symbols as described in Figure 4.4.

ID	IDn	RA (deg)	DEC (deg)	mag	z	Prob	S/N
217	445	195.1388	40.1521	18.31	1.67	1.00	99.35
173	479	195.1468	40.1505	24.32	1.68	0.92	6.51
325	676	195.1452	40.1594	22.88	1.67	0.64	10.79
215	-	195.1348	40.1525	21.94	1.67	0.89	2.03
52	836	195.1302	40.1396	25.91	1.68	0.92	8.25
272	658	195.1523	40.1561	23.13	1.67	1.00	14.38
122	391	195.1459	40.147	24.92	1.68	0.50	4.15
133	-	195.1418	40.1475	23.03	1.67	0.17	3.03
22	-	195.1318	40.1346	21.84	1.67	0.31	6.18
78	-	195.1294	40.1417	22.96	1.68	0.38	6.11

Table 4.12: Member candidates for CARLA J130032+4009. Columns as listed in Table 4.2.

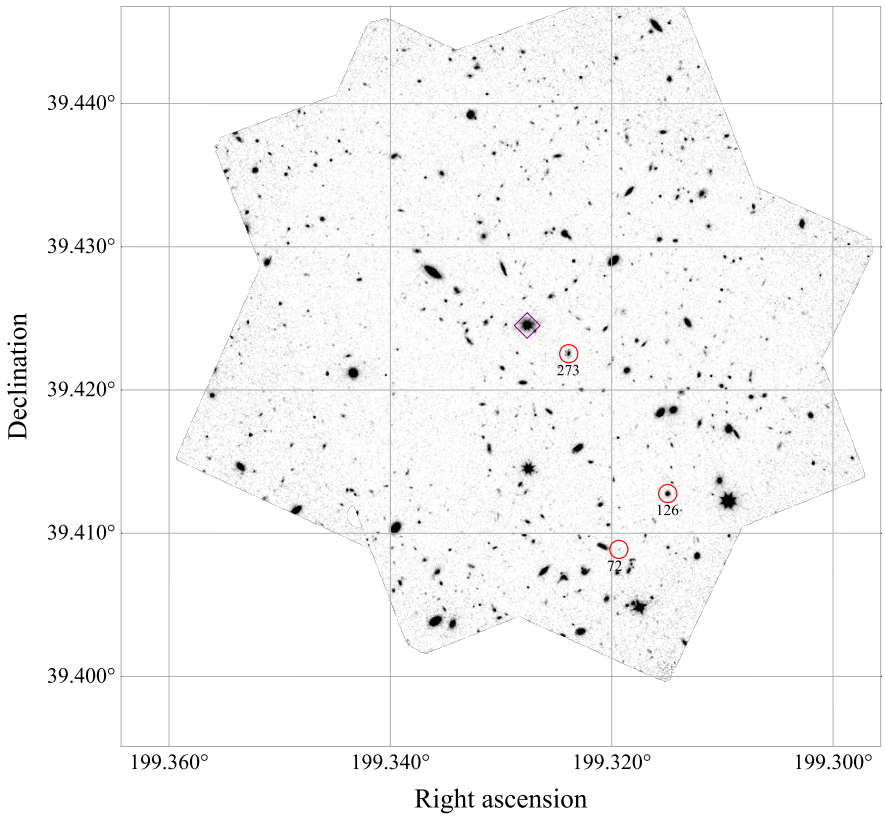

Figure 4.15: The *HST F140W* image of CARLA J131720+3925 with marked proto-cluster galaxies. Symbols as described in Figure 4.4.

ID	IDn	RA (deg)	DEC (deg)	mag	z	Prob	S/N
126	679	199.315	39.4128	21.82	1.57	0.85	3.65
273	-	199.3239	39.4225	22.17	1.57	1.00	12.72
72	-	199.3194	39.4089	25.39	1.57	0.73	7.23

Table 4.13: Member candidates for CARLA J131720+3925. Columns as listed in Table 4.2.

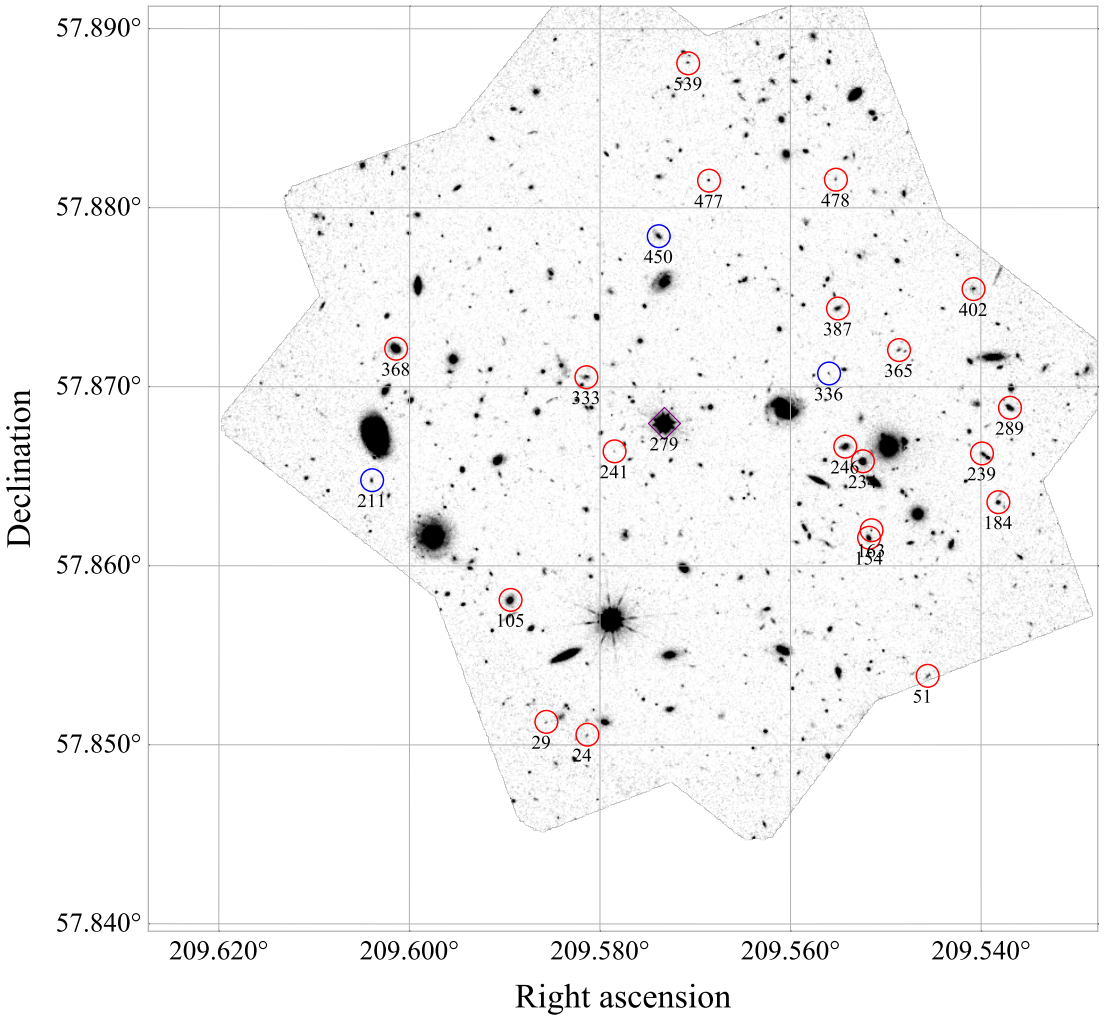

Figure 4.16: The *HST* $F140W$ image of CARLA J135816+5752 with marked proto-cluster galaxies. Symbols as described in Figure 4.4.

ID	IDn	RA (deg)	DEC (deg)	mag	z	Prob	S/N
279	445	209.5733	57.8679	16.54	1.37	1.00	200.67
51	689	209.5456	57.8538	23.36	1.36	0.98	4.73
154	681	209.5518	57.8616	21.82	1.38	0.92	9.01
163	694	209.5515	57.862	24.65	1.37	1.00	7.74
402	52	209.5408	57.8754	22.82	1.36	0.75	5.65
246	-	209.5543	57.8666	21.77	1.38	0.87	10.40
365	-	209.5486	57.872	23.59	1.38	0.31	3.69
368	-	209.6014	57.8721	20.60	1.37	0.49	7.79
289	-	209.537	57.8688	21.93	1.35	0.45	6.40
241	-	209.5785	57.8664	25.32	1.39	0.40	3.58
211	-	209.604	57.8648	23.45	1.39	0.15	3.11
450	-	209.5739	57.8784	22.19	1.36	0.17	4.18
387	250	209.555	57.8744	22.4	1.37	1.00	8.05
478	223	209.5553	57.8816	24.12	1.37	0.99	6.02
239	-	209.5399	57.8663	23.04	1.38	0.97	5.31
105	-	209.5894	57.8581	20.71	1.37	0.89	1.44
539	685	209.5708	57.8881	24.05	1.37	1.00	5.42
184	-	209.5382	57.8635	22.67	1.37	0.75	7.17
234	-	209.5524	57.8658	21.25	1.38	1.00	18.04
333	-	209.5815	57.8705	22.66	1.37	0.60	8.21
24	-	209.5813	57.8506	24.26	1.38	1.00	6.53
29	-	209.5857	57.8513	24.75	1.37	0.72	3.89
477	661	209.5686	57.8815	24.03	1.38	1.00	8.09
336	-	209.556	57.8707	24.70	1.38	0.14	2.75

Table 4.14: Member candidates for CARLA J135816+5752. Columns as listed in Table 4.2.

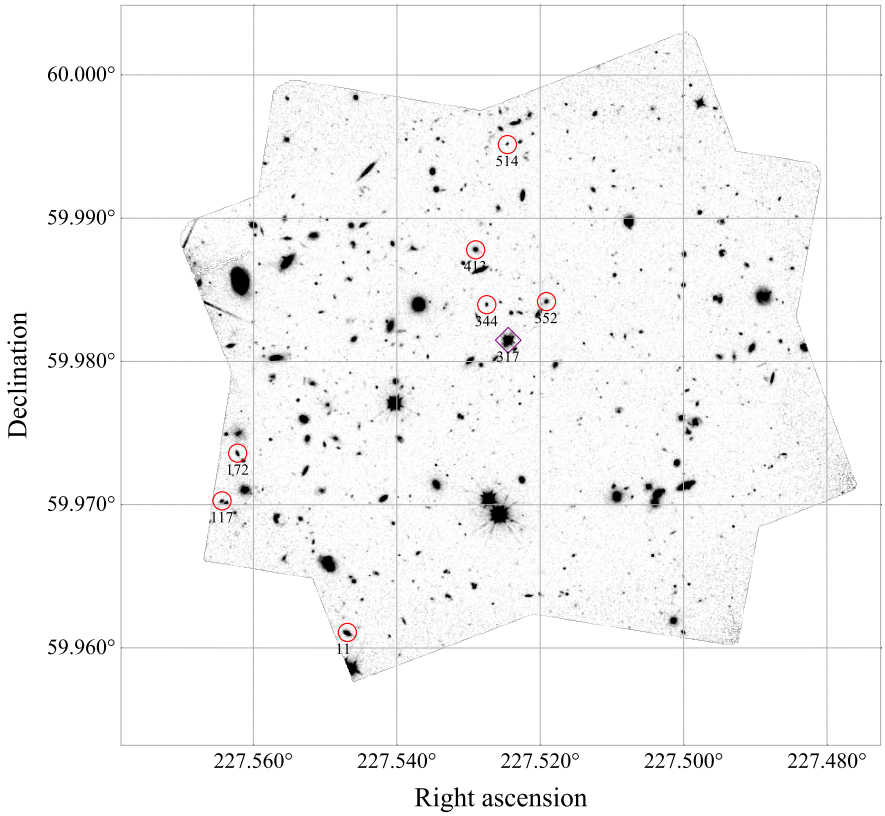

Figure 4.17: The *HST F140W* image of CARLA J151008+5959 with marked proto-cluster galaxies. Symbols as described in Figure 4.4.

ID	IDn	RA (deg)	DEC (deg)	mag	z	Prob	S/N
11	-	227.5469	59.9611	21.20	1.72	0.98	20.06
317	402	227.5245	59.9815	18.17	1.72	1.00	88.81
352	-	227.5192	59.9842	21.86	1.71	0.98	7.22
413	-	227.529	59.9878	21.43	1.71	0.82	2.18
172	-	227.5622	59.9736	22.08	1.72	0.42	3.25
117	-	227.5644	59.9703	22.26	1.74	0.96	12.73
344	771	227.5275	59.984	22.90	1.71	0.85	10.19
514	-	227.5246	59.9951	23.43	1.71	0.33	6.71

Table 4.15: Member candidates for CARLA J151008+5959. Columns as listed in Table 4.2.

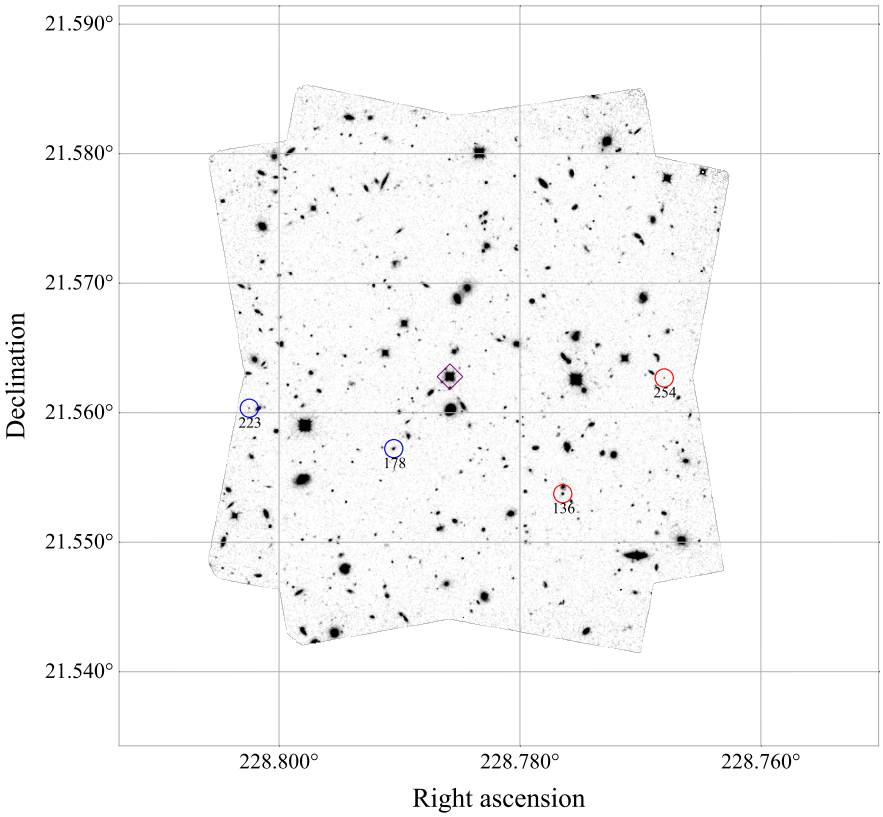

Figure 4.18: The *HST F140W* image of CARLA J151508+2134 with marked proto-cluster galaxies. Symbols as described in Figure 4.4.

ID	IDn	RA (deg)	DEC (deg)	mag	z	Prob	S/N
254	155	228.768	21.5627	24.64	2.27	0.88	14.64
136	-	228.7765	21.5537	22.78	2.26	0.32	3.21
223	-	228.8025	21.5603	24.51	2.23	0.11	2.59
178	-	228.7905	21.5572	22.66	2.27	0.12	1.74

Table 4.16: Member candidates for CARLA J151508+2134. Columns as listed in Table 4.2.

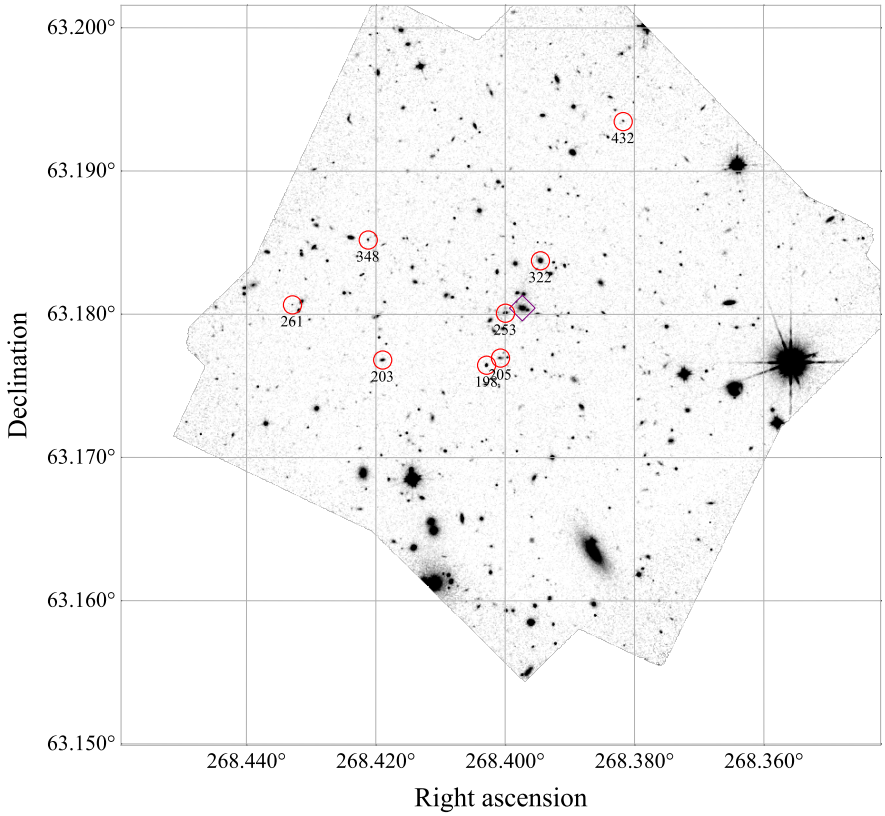

Figure 4.19: The *HST F140W* image of CARLA J175336+6311 with marked proto-cluster galaxies. Symbols as described in Figure 4.4.

ID	IDn	RA (deg)	DEC (deg)	mag	z	Prob	S/N
253	-	268.4	63.1801	21.68	1.57	0.59	0.71
261	619	268.433	63.1806	24.91	1.58	1.00	14.25
203	-	268.419	63.1768	22.11	1.57	0.70	1.43
198	-	268.4029	63.1764	21.85	1.57	0.97	2.29
348	-	268.4212	63.1852	23.67	1.57	0.97	5.73
322	-	268.3946	63.1837	21.18	1.58	0.99	1.34
432	-	268.3818	63.1934	24.01	1.58	0.82	6.77
205	-	268.4008	63.1769	23.07	1.58	0.90	5.26

Table 4.17: Member candidates for CARLA J175336+6311. Columns as listed in Table 4.2.

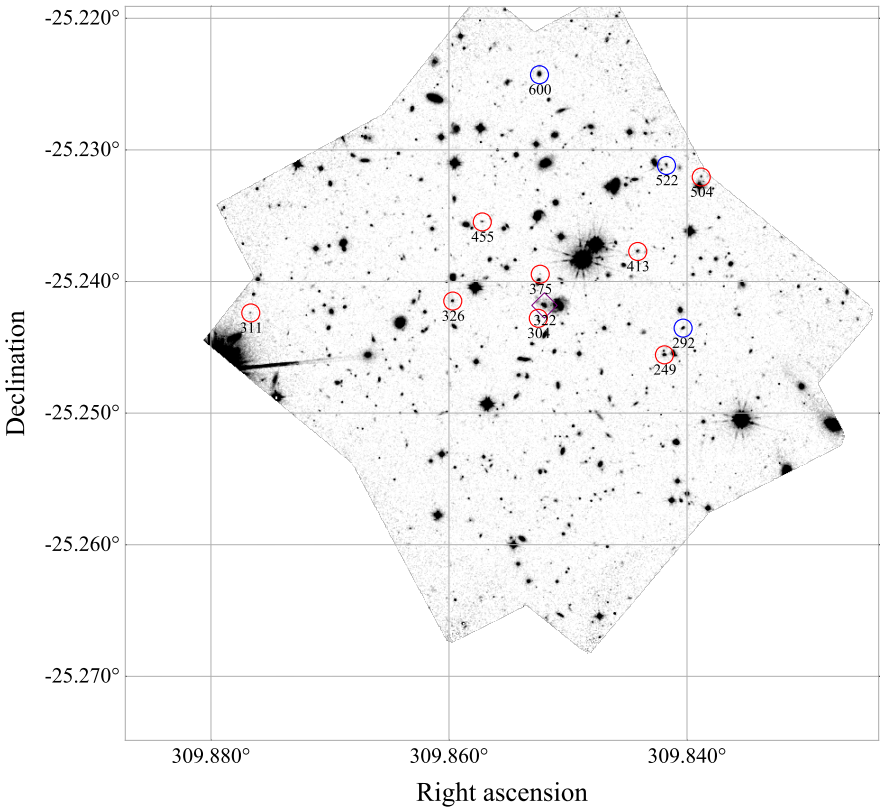

Figure 4.20: The *HST F*140*W* image of CARLA J203924-2515 with marked protocluster galaxies. Symbols as described in Figure 4.4.

ID	IDn	RA (deg)	DEC (deg)	mag	z	Prob	S/N
375	44300	309.8523	-25.2395	25.26	2.01	0.97	7.46
600	-	309.8524	-25.2243	21.74	1.97	0.10	2.60
322	306	309.852	-25.2418	20.91	1.99	1.00	90.67
304	356	309.8525	-25.2428	24.13	2.00	0.96	9.20
522	-	309.8417	-25.2312	23.09	1.98	0.11	3.70
504	697	309.8388	-25.2321	23.64	2.00	0.97	8.55
413	174	309.8442	-25.2377	22.8	2.00	1.00	6.07
292	-	309.8403	-25.2436	22.23	2.04	0.11	2.36
455	360	309.8572	-25.2355	23.74	2.00	1.00	14.40
326	-	309.8597	-25.2415	22.62	2.02	0.35	2.79
311	-	309.8767	-25.2424	24.54	2.02	0.85	9.98
249	-	309.8419	-25.2456	22.03	2.00	0.74	2.12

Table 4.18: Member candidates for CARLA J203924-2515. Columns as listed in Table 4.2.

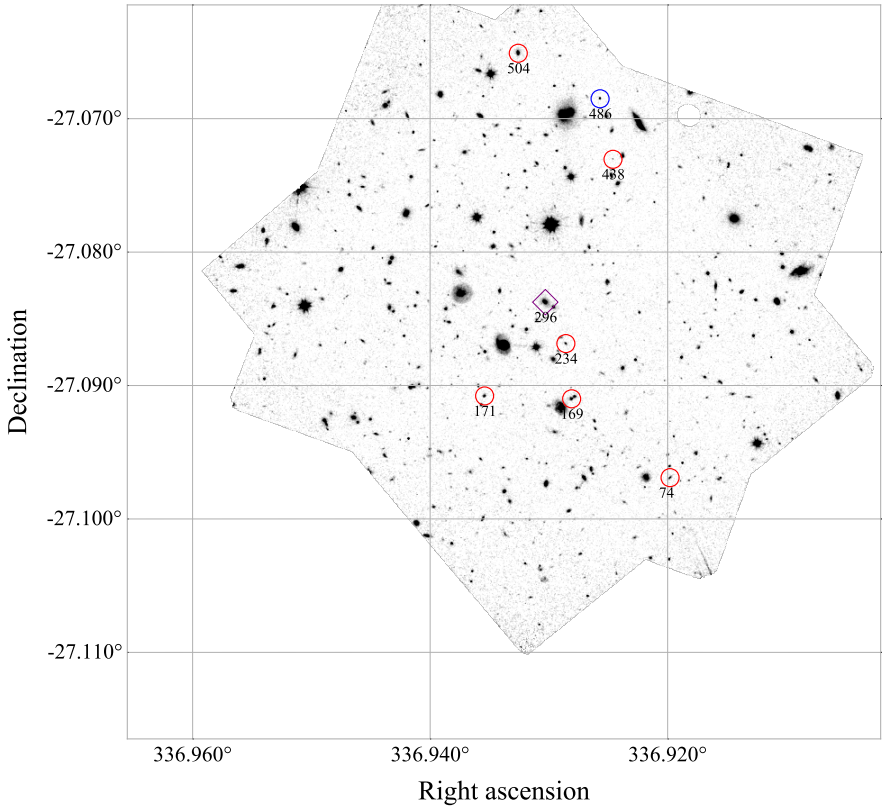

Figure 4.21: The *HST F*140*W* image of CARLA J222744-2705 with marked protocluster galaxies. Symbols as described in Figure 4.4.

ID	IDn	RA (deg)	DEC (deg)	mag	z	Prob	S/N
234	525	336.9286	-27.0869	23.34	1.68	1.00	12.77
296	590	336.9303	-27.0838	20.59	1.68	1.00	192.48
74	846	336.9198	-27.0969	23.16	1.70	0.99	9.67
504	-	336.9326	-27.0651	21.43	1.69	0.86	0.56
171	-	336.9354	-27.0908	22.93	1.70	0.37	5.22
438	268	336.9246	-27.0731	25.21	1.68	1.00	12.51
486	-	336.9257	-27.0685	22.95	1.69	0.18	2.56
169	406	336.9281	-27.091	22.36	1.71	0.86	8.83

Table 4.19: Member candidates for CARLA J222744-2705. Columns as listed in Table 4.2.

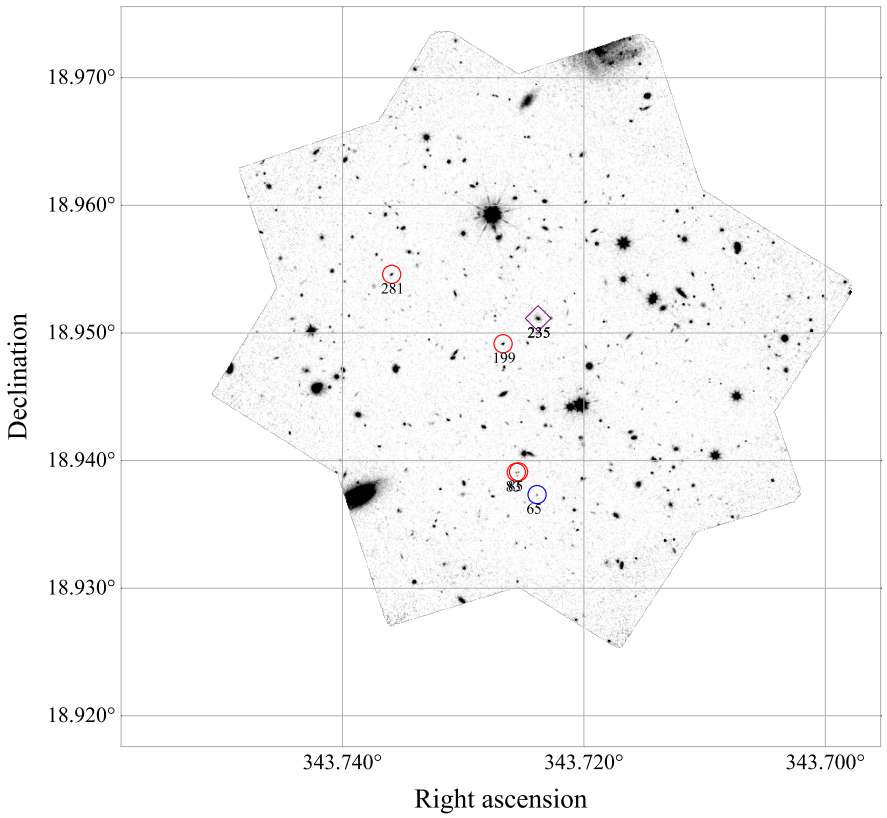

Figure 4.22: The *HST F140W* image of CARLA J225452+1857 with marked proto-cluster galaxies. Symbols as described in Figure 4.4.

ID	IDn	RA (deg)	DEC (deg)	mag	z	Prob	S/N
83	525	343.7256	18.9391	24.64	2.15	1.00	12.38
65	-	343.7239	18.9373	24.49	2.15	0.16	2.64
281	-	343.7359	18.9546	23.22	2.16	0.85	5.20
85	-	343.7254	18.9391	24.79	2.16	0.72	3.88
235	368	343.7238	18.9511	21.94	2.16	1.00	44.87
199	-	343.7267	18.9491	22.74	2.15	0.44	2.91

Table 4.20: Member candidates for CARLA J225452+1857. Columns as listed in Table 4.2.

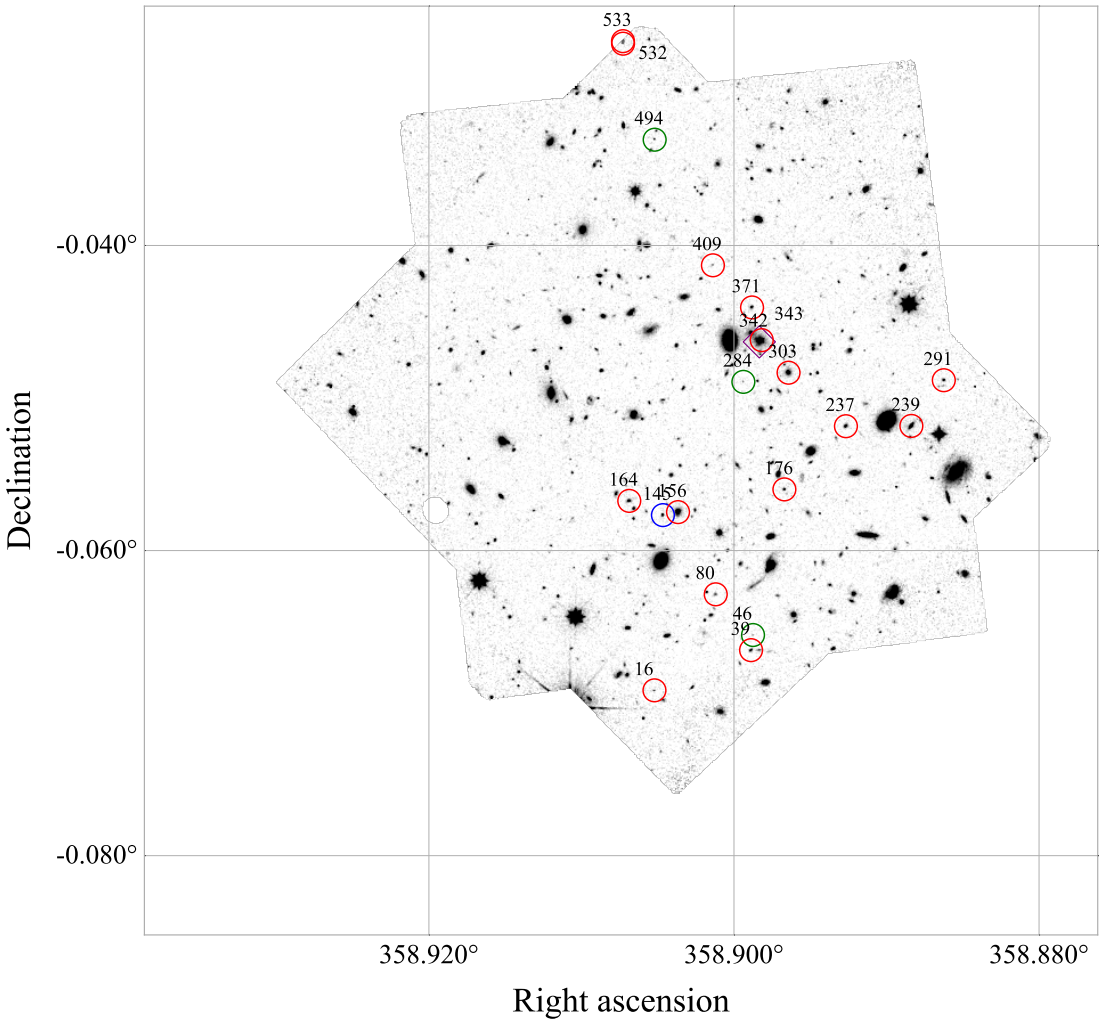

Figure 4.23: The *HST F*140*W* image of CARLA J235536-0003 with marked proto-cluster galaxies. Columns as listed in Table 4.2.

ID	IDn	RA (deg)	DEC (deg)	mag	z	Prob	S/N
371	736	358.8988	-0.0441	22.96	1.48	1.00	7.69
145	-	358.9047	-0.0577	22.87	1.52	0.10	3.00
80	-	358.9012	-0.0629	23.71	1.50	0.65	3.21
343	-	358.8982	-0.0462	20.85	1.49	1.00	34.42
284	-	358.8994	-0.049	25.18	1.50	0.21	3.90
532	893	358.9073	-0.0268	23.88	1.49	1.00	8.95
156	-	358.9037	-0.0575	21.09	1.49	0.33	3.36
39	-	358.8989	-0.0665	23.13	1.49	0.81	3.93
164	676	358.9069	-0.0568	22.44	1.50	1.00	12.68
237	334	358.8927	-0.0519	22.55	1.49	0.92	4.08
239	-	358.8884	-0.0518	21.3	1.49	0.94	0.46
342	351	358.8984	-0.0463	20.84	1.51	0.38	12.59
176	478	358.8967	-0.056	23.09	1.50	0.78	11.00
303	337	358.8964	-0.0484	21.53	1.50	1.00	8.13
291	-	358.8863	-0.0488	23.2	1.49	0.48	7.24
46	685	358.8988	-0.0656	25.2	1.48	0.29	6.26
409	751	358.9014	-0.0413	24.61	1.50	1.00	9.23
494	855	358.9052	-0.0331	24.25	1.49	0.29	6.78
533	879	358.9073	-0.0266	23.2	1.49	0.39	5.15
16	213	358.9052	-0.0692	24.61	1.48	1.00	10.16

Table 4.21: Member candidates for CARLA J235536-0003. Columns as listed in Table 4.2.

4.4.2 Comparing the luminosity functions of proto-cluster and field galaxies

In order to compare proto-cluster galaxies with field galaxies, we built luminosity functions (LFs). In the left panels of Figure 4.24 we show the luminosity functions for all proto-clusters member candidates and field candidates with probabilities larger than 10%. Proto-clusters member candidates are represented in red, whilst field galaxies are shown in blue.

In the top panel, we can see that the number of galaxies per area is higher for proto-cluster galaxies than for the field in each luminosity bin, which is expected since the proto-clusters were selected as having a galaxy overdensity of at least 1. In the bottom panels, we show the total number of proto-cluster member candidates divided by the total number of field candidates (including repeated field galaxies) in each luminosity bin. The mean value is 3.9, which means proto-clusters have ~ 4 times more galaxies than the field.

Although all luminosity bins present an excess of proto-cluster galaxies, the luminosity functions of proto-cluster and field galaxies are clearly different. There is a large excess of luminous galaxies ($> 10^{11}\,L_{\odot}$) in proto-clusters. This excess decreases with decreasing luminosity down to $\sim 10^{10}\,L_{\odot}$. Then we see an increase in the excess of low luminosity galaxies ($\sim 10^{9.5}\,L_{\odot}$) in proto-clusters.

To explore whether this result is dependant on our membership selection criteria, we re-evaluate the LFs based on galaxies selected at 30% and 50% probabilities as shown in the middle and right panels of Figure 4.24. We find exactly the same trends as found for the galaxies selected by 10% probability, with similar N_m/N_f within uncertainties. We therefore do not believe this result is strongly affected by our selection criteria.

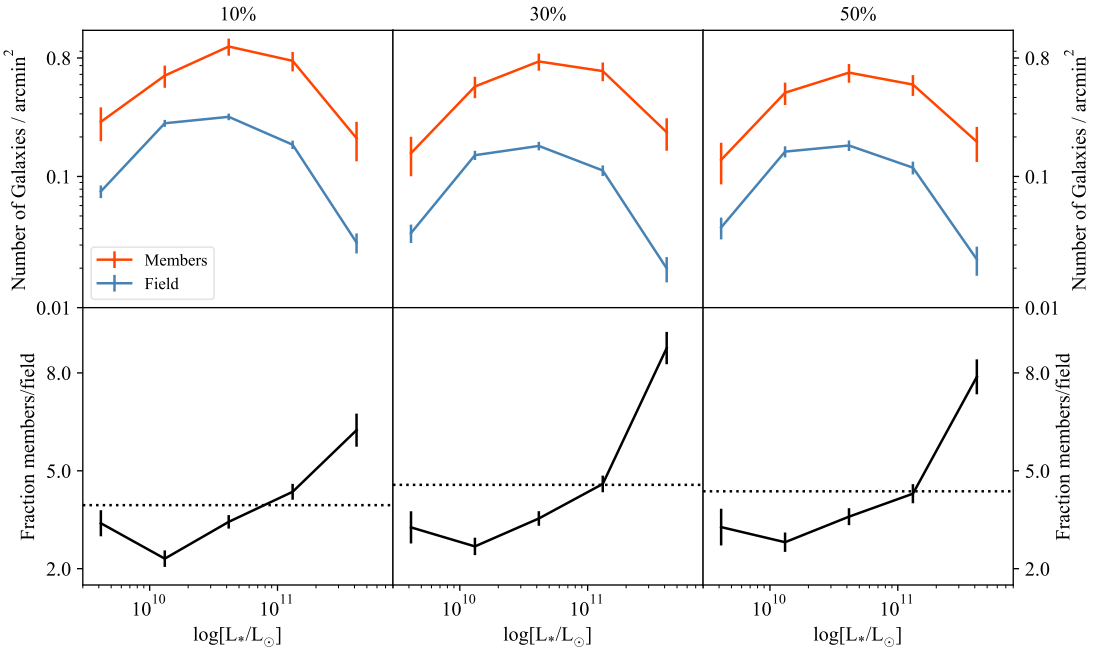

Figure 4.24: Luminosity functions for different probabilities. The top panels show the luminosity functions for members (red) and field (blue) galaxies. The columns show the functions for different selections considering the probability of the galaxy of being in the redshift of the RLAGN (10%, 30% and 50%). The bottom curves show the number of members divided by the field. The dotted lines are the mean values for the samples across all luminosities.

To check the dependency of the LF on redshift, the sample was divided in two redshift bins, $z < 1.6$ and $z > 1.6$. This is shown in Figure 4.25. In the right panel, we show the full sample, in the middle we show the sample at $z < 1.6$, and in the right panel we show the sample for $z > 1.6$. For $z < 1.6$, we find 91 proto-cluster candidates and 368 corresponding to field galaxies. At $z > 1.6$, we find 40 proto-cluster member candidates and 498 field galaxies.

The mean N_m/N_f is highest for the low redshift sample at 5.5, and lowest for the high redshift sample at 3.2, as can be seen in the bottom panels of Figure 4.25. This effect can also be seen in the top panels, in which the red curves have decreased values from the left to the right. In the rightmost bin, there is an excess of luminous ($\sim 10^{11} L_\odot$) galaxies for all redshift bins. Similar to the full

sample, we see the same trends in both $z < 1.6$ and $z > 1.6$ samples. The bottom panels fractions increase slightly from $\sim 10^{10} L_{\odot}$ to $\sim 4 \times 10^{11} L_{\odot}$, and this trend is observed in all redshift ranges. The proto-clusters also have a small excess of the lowest luminosity galaxies in our sample compared to the field. In general, the proto-clusters lack galaxies in the middle luminosity bins ($\sim 1 - 5 \times 10^{10} L_{\odot}$) compared to the field.

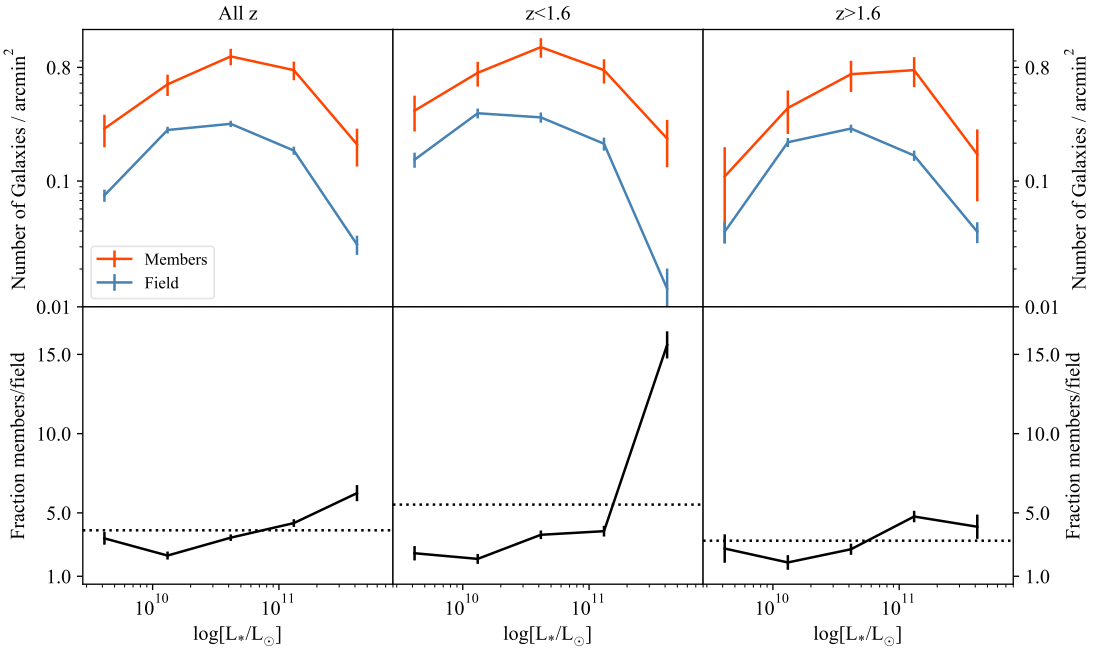

Figure 4.25: Luminosity functions for different redshift ranges. The colors and x and y axis are the same as Figure 4.24, but the columns are for different redshifts. In the left column we use the full sample, in the middle panel we use galaxies with $z < 1.6$ and in the right panel we use galaxies with $z > 1.6$. The dotted lines are the mean values for the fractions dividing the luminosities in 5 bins.

4.4.3 Comparing the ages of proto-cluster and field galaxies

For the subsample of proto-cluster and field galaxies that lie at $z > 1.9$, the grism spectra cover the wavelength range of the rest-frame Balmer and 4000 Åbreaks. Thus the grism spectra allows us to compare the ages of the proto-cluster and

field galaxies for the subset that are at $z > 1.9$ and are bright enough to allow us to measure the D_n4000 break. In total 21 proto-cluster galaxies have a measured D_n4000 break. We make a S/N cut to ensure the D_n4000 break is measured to at least a S/N of 2, which leaves us with 17 proto-cluster galaxies with robust D_n4000 breaks. We also find 48 field galaxies which have at least a S/N of 2 in their break strength. As mentioned in Chapter 1, the D_n4000 is a useful proxy of galaxies' ages. We compared the distribution of D_n4000 measurements for galaxies in the field and proto-clusters in Figure 4.26. Although both samples span a wide range of D_n4000 values, the field sample is peaked around $D_n4000 \sim 0.9$ whereas the proto-cluster samples is not peaked and has more galaxies with higher values of D_n4000. A 2-sided Ks test gives a probability of only 2.5% that these distributions are drawn from the same underlying distribution. Therefore, we find that $z \sim 2$ proto-cluster galaxies tend to have larger D_n4000 breaks than field galaxies, implying an age difference in their stellar populations.

In Figure 4.27 we stack the data into bins of D_n4000 and explore the overdensity of galaxies as a function of D_n4000. We find no overdensity of galaxies with low values of $D_n4000 \sim 0.5$, and the overdensity increases for larger values of D_n4000. This means that older galaxies are increasingly rare at $z \sim 2$, and that proto-clusters contain an increasingly large overdensity of them.

4.5 Discussion

Compared to Noirot et al. (2018), our proto-cluster member catalogue is equal or larger for 16 proto-clusters and includes quiescent galaxies since we do not select only emission line galaxies. This means that we get galaxies with lower S/N that were not present in their previous catalogue, as can be seen in Figure

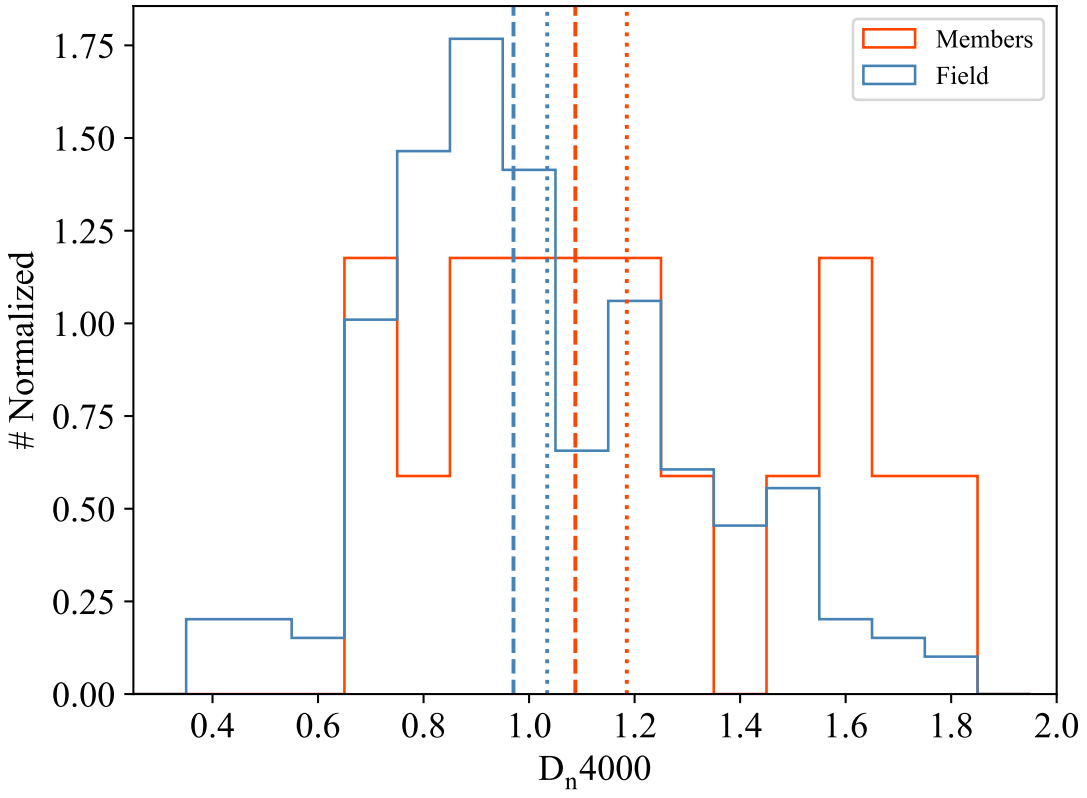

Figure 4.26: D_n4000 distribution for proto-cluster members (red) and field (blue). The dotted lines are the mean D_n4000 for each environment and the dashed lines the median.

4.3. Now we have a sample of continuum galaxies that can be studied separately. However, for 4 proto-clusters, we got fewer members than Noirot et al. (2018). CARLAJ09582904 is not considered as an overdensity by our work, and we miss 3 galaxies that Noirot considered as member. CARLAJ1052+0806 is also not an overdensity and we miss one galaxy. In the case of CARLAJ1129+0951 and CARLAJ0800+4029, these are real proto-clusters and we miss one galaxy from each of them. The possible explanation for this is that we excluded galaxies that were too close and we considered them as duplicates, so we excluded one of them from the catalogue.

One advantage of having an objective way of defining the proto-cluster sample

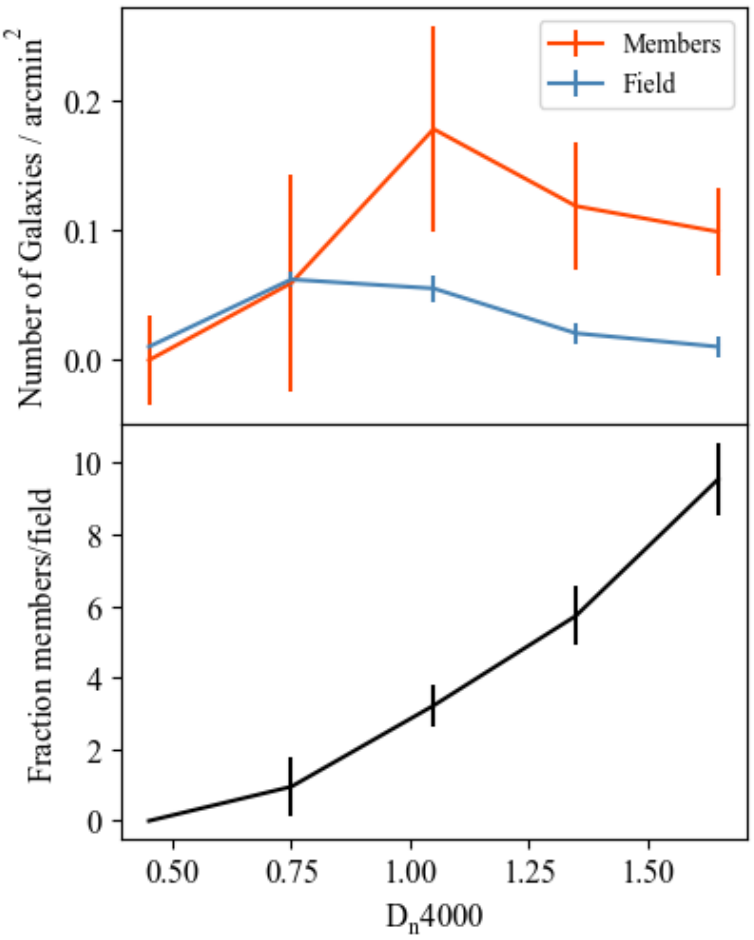

Figure 4.27: D_n4000 fraction. Members are shown in red and field galaxies are in blue. The top panel we show the number of galaxies per area for different D_n4000. In the bottom panel we show the fraction of members divided by field.

is that we can compare the samples in different environments, such as comparing proto-clusters with field galaxies. Due to a well defined sample we were able to compare luminosity functions and D_n4000 in different environments.

We present the first comparisons of D_n4000 in proto-clusters and field at $z \sim 2$. Our D_n4000 estimates indicate that at $z \sim 2$ the stellar population in proto-clusters is already older compared to the field. This means that the star-formation in proto-clusters is less recent than in the field.

Examining the LFs and member to field fractions of Figure 4.25, we can see that

the lowest fractions are in $\sim 10^{10} L_{\odot}$. It is not clear whether this effect is physical or observational. There is the possibility that these galaxies are not being detected due to a high fraction of passive galaxies in proto-clusters in this luminosity range. We would not be able to observe them due to the absence of emission lines and faint continuum. Another possibility is that this is a physical characteristic of these systems and there are fewer objects with $\sim 10^{10} L_{\odot}$ compared to other luminosity ranges.

Cooke et al. (2014) analysed the MRC 2104-242 proto-cluster at $z = 2.5$ and also found an excess of massive galaxies ($M_* > 10^{10.5}\, M_{\odot}$) in the proto-cluster compared to the field, which is in agreement with our results. The same trend was also seen by Shimakawa et al. (2017) analysing the USS1558-003 proto-cluster at $z = 2.5$. They found an excess of $M_* > 10^{10.5}\, M_{\odot}$ galaxies in the densest regions of the proto-cluster. Although we only analyze clusters until $z \sim 2$, we found similar results in terms of stellar mass distribution as these two works. In this work, we extended these results for a sample of 10 spectroscopic confirmed proto-clusters.

The work presented in this Chapter is in agreement with what we found in Chapter 2, that the infall region at $z \sim 1$ already have massive galaxies. Our results regarding the D_n4000 distribution show that proto-clusters have an excess of passive galaxies, which suggests that the excess of passive galaxies seen in Chapter 2 could have already formed in proto-clusters at $z \sim 2$. Although the very massive galaxies seem to be forming in the observed redshift range, our results suggests that if we want to understand the formation of $M_* \sim 10^{11}$ galaxies, we have to look at even higher redshifts since part of this population already exists at $z > 1.6$.

4.6 Conclusion

In this Chapter, we investigated the luminosity functions, quiescent fractions and stellar ages of galaxies in different environments: proto-cluster galaxies and field galaxies. Analysing the luminosity functions we found that the proto-cluster luminosity function differs from the field. As previously shown in Ito et al. (2020) analysing the UV luminosity functions for proto-clusters at $z \sim 4$, and Muldrew et al. (2018) using simulations, we found that there is an excess of luminous galaxies in proto-clusters compared to the field. We found proto-cluster galaxies have higher D_n4000 values, which we interpret that the proto-cluster galaxies have older stellar populations. Considering these results, we conclude that the environment where these galaxies reside affect their properties until at least $z \sim 2$. To fully understand why the properties of galaxies are different in different environments, further data is required. In particular it would be useful to estimate their stellar masses and UVJ colours, so we would be able to classify them between passive and star-forming.

Chapter 5

Conclusions and Future Work

In this thesis, I report my findings on the evolution of galaxies in proto-clusters at $0.8 < z < 3.0$. The main point of this thesis was to investigate the relevance of preprocessing, the presence of ICL and properties of galaxies in high redshift proto-clusters. Specifically, how the properties of galaxies in proto-clusters differ from field galaxies and from low redshift cluster galaxies.

5.1 Questions and Answers

In this work, I answered three main questions related to the evolution of galaxies in proto-clusters. I describe the questions and answers below.

- *Is pre-processing important in high redshift clusters?* Using the GOGREEN and GCLASS sample of clusters at $0.8 < z < 1.3$, and analysing the cluster main halo, infall and field galaxies, I found that most galaxies with stellar masses $> 10^{10}\,M_{\odot}$ quenched prior entering the cluster main halo. This means that galaxies quenched before arriving in the cluster and this is stronger for

more massive galaxies $> 10^{11}\,M_{\odot}$. I also found that infall galaxies have more satellites than the field, which indicates a larger presence of groups in the infall region. I found that satellite quenching is independent of stellar mass. I conclude that satellite quenching is not important for $z \sim$1 clusters, most quenching occurred during infall. So the answer for this question is: yes, pre-processing is an important mechanism for quenching galaxies at high redshifts. This has consequences for estimating quenching timescales. We proved that galaxies in the field are not progenitors of cluster galaxies, the progenitors are galaxies in the infall population. I showed that using the field population as a substitute for the infalling population can result in incorrect quenching timescales. So when estimating quenching timescales, the infall population should be carefully constructed.

- *Is ICL present in galaxy proto-clusters?* I detected a considerable amount of ICL in two proto-clusters at $z \sim 2$. This was not expected by previous simulations, that predict that the bulk of ICL was formed only at $z \sim 1$. So I conclude that ICL was formed earlier than expected by models. Analysing the surface brightness profiles of the BCGs of the two proto-clusters, I found that they have extended profiles compared to other proto-cluster massive galaxies. The BCGs profiles are similar to other BCGs profiles in lower redshifts. Because the intracluster light is made of free-floating stars connected to the dark matter halo of the proto-cluster, I argue that the ICL can be a useful way to detect massive dark matter halos at high redshifts. So the answer of this question is: yes, there is a significant amount of ICL in proto-clusters at $z \sim 2$.

- *When does the properties of proto-cluster galaxies and field start to differ?* Analysing proto-cluster galaxies at $1.3 < z < 3.0$, I found that proto-cluster

galaxies have different luminosity functions compared to field galaxies. I also found that proto-cluster galaxies have stronger D_n4000 breaks compared to field galaxies. I interpret this to mean that proto-clusters have older stellar populations than field galaxies. So at least by $z \sim 3$, proto-cluster galaxies differ from field galaxies.

With these findings we advanced the knowledge about pre-processing and ICL in proto-clusters of galaxies at high redshifts. This work shows that it is necessary to extend the study of the infall region around proto-clusters, since galaxies in this region are progenitors of cluster galaxies. My work also indicates that ICL was formed previously than thought and points to the necessity of searching for ICL at $z > 2$. Furthermore, more research about proto-clusters at $z > 3$ is required to answer the question when is the limit where the proto-cluster environment affects galaxies properties, since until $z \sim 3$ I have found that proto-cluster galaxies differ from the field.

This work changed our perspective on galaxy evolution at high redshifts and why we should care both about the inner regions and outskirts of galaxy proto-clusters in high redshifts. So, to understand the evolution of galaxies in high redshifts, the proto-cluster environment should be considered since we have shown that it will affect galaxies' properties.

How galaxies evolve in different cosmic times is still an open question, and in this thesis I have added important pieces to this puzzle of how they evolve in dense environments in the early Universe.

5.2 Long-term follow-up

My thesis research has produced several new avenues that can be explored. The three main questions are:

- *How can we differentiate a cluster from a proto-cluster?* It is essential to be able to observationally differentiate between a collapsed cluster and a collection of smaller halos that make a proto-cluster. This is necessary because the halo mass function of clusters is an important cosmological probe, with most of the power from this probe coming from the highest redshifts (z$\sim$2), where clusters and proto-clusters can be easily confused when only considering galaxy richness. This confusion adds systematic errors in the cosmological parameters derived from the evolution of cluster abundance. The work I have presented in this thesis shows that it may be possible to differentiate between a collapsed cluster and a proto-cluster by measuring the different properties of these structures. Possible properties that may be different are the ICL fraction, the number of passive galaxies in the main halo and X-ray emission in structures at z$\sim$2. My initial studies into the ICL and galaxy population in a few proto-clusters can be extended to thousands of clusters and proto-clusters that will be observed with Euclid and LSST.

- *How does the fraction of free-floating stars evolve at z>2?* Related to that, the ICL represents the stars that do not end up in the remnant after galaxy mergers and close interactions. Since the amount of ICL is related to the merger history of galaxies, its light is connected to how structures grow. Therefore, the evolution of ICL provides a means to test the growth efficiency of galaxy mergers and is a reliable test of galaxy formation and evolution models. I have shown that there is currently a lack in both observations

and simulations of ICL at z>2.0. Improvements in the simulations should be done, and higher redshift analysis is needed. Regarding the simulations, although hydrodynamical simulations showed that ICL is a common feature around BCGs at high redshifts, the BCG mass is too massive compared to observations, so improvements in the estimates of BCG growth is needed. Regarding the observations, the analysis of BCGs in proto-clusters at $z > 2$ is needed to confirm the maximum redshift that we can find ICL. To estimate the ICL mass, mass-to-light ratios are needed. The best way to obtain accurate mass-to-light ratios is to fit the spectral energy distributions of the intracluster light, which requires deep multi-band images in the near to mid-infrared that have only become possible recently due to the successful deployment of *JWST*.

- *What is the fraction of AGN in the outskirts of clusters?* The third question comes from the fact that in Werner et al. (2021), we found that most massive galaxies quench in the infall region of clusters. One possible process that is known for quenching massive galaxies is AGN feedback. Since z∼2.0 is the peak of AGN activity, it is possible that AGN feedback is responsible for quenching the massive infalling galaxies. This can also be explored using deep X-ray images of the outskirts of distant clusters and proto-clusters to identify the fraction of AGN in these environments. Also, through my data analysis, I found many groups of passive galaxies falling in the cluster's main halo. The infalling region of high redshift clusters and proto-clusters is still poorly understood. Specifically, the relation between AGN and the proto-cluster environment. I therefore believe it would be fruitful to search for AGN in the infall region of proto-clusters and investigate the effects of AGN activity in those galaxies. This would provide hints about what could be the

main physical process that is quenching these galaxies.

Data from recent and future telescopes, such as *Euclid*, *LSST* and *JWST*, will be useful to get deeper data and more complete samples.

Bibliography

Abell G.O., 1958. *The Distribution of Rich Clusters of Galaxies.* ApJS, 3, 211.

Abell G.O., 1965. *Clustering of Galaxies.* ARA&A, 3, 1.

Adami C., Pompei E., Sadibekova T. et al., 2016. *The XXL Survey. VIII. MUSE characterisation of intracluster light in a z ~0.53 cluster of galaxies.* A&A, 592, A7.

Aghanim N., Akrami Y., Ashdown M. et al., 2020. *iPlanck/i2018 results.* A&A, 641, A6.

Allen S.W., Evrard A.E. & Mantz A.B., 2011. *Cosmological Parameters from Observations of Galaxy Clusters.* Annual Review of Astronomy and Astrophysics, 49, 1, 409–470.

Allen S.W., Evrard A.E. & Mantz A.B., 2011. *Cosmological Parameters from Observations of Galaxy Clusters.* ARA&A, 49, 409–470.

Alonso Asensio I., Dalla Vecchia C., Bahé Y.M. et al., 2020. *The intracluster light as a tracer of the total matter density distribution: a view from simulations.* MNRAS, 494, 2, 1859–1864.

Arnaboldi M., Freeman K.C., Mendez R.H. et al., 1996. *The Kinematics of the Planetary Nebulae in the Outer Regions of NGC 4406.* ApJ, 472, 145.

Bahcall N.A. & Cen R., 1992. *Galaxy clusters and cold dark matter - A low-density unbiased universe?* ApJ, 398, L81–L84.

Bahé Y.M., Barnes D.J., Vecchia C.D. et al., 2017. *The Hydrangea simulations: galaxy formation in and around massive clusters.* MNRAS, 470, 4, 4186–4208.

Baldry I.K., Glazebrook K., Brinkmann J. et al., 2004. *Quantifying the Bimodal Color-Magnitude Distribution of Galaxies.* ApJ, 600, 2, 681–694.

Baldry I.K., Balogh M.L., Bower R.G. et al., 2006. *Galaxy bimodality versus stellar mass and environment.* MNRAS, 373, 2, 469–483.

Balogh M.L., Baldry I.K., Nichol R. et al., 2004. *The Bimodal Galaxy Color Distribution: Dependence on Luminosity and Environment.* ApJ, 615, 2, L101–L104.

Balogh M.L., McGee S.L., Mok A. et al., 2016. *Evidence for a change in the dominant satellite galaxy quenching mechanism atz = 1.* Monthly Notices of the Royal Astronomical Society, 456, 4, 4364–4376.

Balogh M.L., Gilbank D.G., Muzzin A. et al., 2017. *Gemini Observations of Galaxies in Rich Early Environments (GOGREEN) I: survey description.* MNRAS, 470, 4, 4168–4185.

Balogh M.L., van der Burg R.F.J., Muzzin A. et al., 2021. *The GOGREEN and GCLASS surveys: first data release.* MNRAS, 500, 1, 358–387.

Bartelmann M., 1996. *Arcs from a universal dark-matter halo profile.* A&A, 313, 697–702.

Behroozi P.S. & Silk J., 2015. *A Simple Technique for Predicting High-redshift Galaxy Evolution.* ApJ, 799, 1, 32.

Bekki K., 1998. *Unequal-Mass Galaxy Mergers and the Creation of Cluster S0 Galaxies.* The Astrophysical Journal, 502, 2, L133–L137.

Bell E.F., Wolf C., Meisenheimer K. et al., 2004. *Nearly 5000 Distant Early-Type Galaxies in COMBO-17: A Red Sequence and Its Evolution since z˜1.* ApJ, 608, 2, 752–767.

Benson A.J., Bower R.G., Frenk C.S. et al., 2003. *What Shapes the Luminosity Function of Galaxies?* ApJ, 599, 1, 38–49.

Bertin E. & Arnouts S., 1996. *SExtractor: Software for source extraction.* A&AS, 117, 393–404.

Bialas D., Lisker T., Olczak C. et al., 2015. *On the occurrence of galaxy harassment.* Astronomy &amp Astrophysics, 576, A103.

Bianconi M., Smith G.P., Haines C.P. et al., 2018. *LoCuSS: pre-processing in galaxy groups falling into massive galaxy clusters at z = 0.2.* MNRAS, 473, 1, L79–L83.

Binggeli B., Sandage A. & Tammann G.A., 1988. *The luminosity function of galaxies.* ARA&A, 26, 509–560.

Birnboim Y. & Dekel A., 2003. *Virial shocks in galactic haloes?* MNRAS, 345, 1, 349–364.

Biviano A., van der Burg R.F.J., Balogh M.L. et al., 2021. *The GOGREEN survey: the internal dynamics of clusters of galaxies at redshift 0.9-1.4.*

Blanton M.R., Hogg D.W., Bahcall N.A. et al., 2003. *The Galaxy Luminosity Function and Luminosity Density at Redshift z = 0.1.* ApJ, 592, 2, 819–838.

Böhringer H. & Schartel N., 2013. *X-ray galaxy cluster studies for astrophysics and cosmology.* Astronomische Nachrichten, 334, 482.

Booth C.M. & Schaye J., 2010. *Dark matter haloes determine the masses of supermassive black holes.* Monthly Notices of the Royal Astronomical Society: Letters, 405, 1, L1–L5.

Borlaff A.S., Gó mez-Alvarez P., Altieri B. et al., 2022. *iEuclid/i preparation.* A&A, 657, A92.

Bower R.G., Benson A.J., Malbon R. et al., 2006. *Breaking the hierarchy of galaxy formation.* MNRAS, 370, 2, 645–655.

Brammer G., Ryan R. & Pirzkal N., 2015. *Source-dependent master sky images for the WFC3/IR grisms.* Instrument Science Report WFC3 2015-17, 18 pages.

Brammer G., 2016. *Reprocessing WFC3/IR Exposures Affected by Time-Variable Backgrounds.* Instrument Science Report WFC3 2016-16, 12 pages.

Brammer G., 2019. *Grizli: Grism redshift and line analysis software.*

Brammer G.B., van Dokkum P.G. & Coppi P., 2008. *EAZY: A Fast, Public Photometric Redshift Code.* ApJ, 686, 2, 1503–1513.

Bruzual G. & Charlot S., 2003a. *Stellar population synthesis at the resolution of 2003.* MNRAS, 344, 4, 1000–1028.

Bruzual G. & Charlot S., 2003b. *Stellar population synthesis at the resolution of 2003.* MNRAS, 344, 4, 1000–1028.

Burenin R.A., Vikhlinin A., Hornstrup A. et al., 2007. *The 400 Square Degree ROSAT PSPC Galaxy Cluster Survey: Catalog and Statistical Calibration.* ApJS, 172, 561–582.

Butcher H. & Oemler A. J., 1978. *The evolution of galaxies in clusters. I. ISIT photometry of Cl 0024+1654 and 3C 295.* ApJ, 219, 18–30.

Calzetti D., Armus L., Bohlin R.C. et al., 2000. *The Dust Content and Opacity of Actively Star-forming Galaxies.* ApJ, 533, 2, 682–695.

Casey C.M., 2016. *THE UBIQUITY OF COEVAL STARBURSTS IN MASSIVE GALAXY CLUSTER PROGENITORS.* The Astrophysical Journal, 824, 1, 36.

Cattaneo A. & Best P.N., 2009. *On the jet contribution to the active galactic nuclei cosmic energy budget.* Monthly Notices of the Royal Astronomical Society, 395, 1, 518–523.

Chabrier G., 2003a. *Galactic Stellar and Substellar Initial Mass Function.* PASP, 115, 763–795.

Chabrier G., 2003b. *Galactic Stellar and Substellar Initial Mass Function.* PASP, 115, 809, 763–795.

Chan T.K., Kereš D., Wetzel A. et al., 2018. *The origin of ultra diffuse galaxies: stellar feedback and quenching.* MNRAS, 478, 1, 906–925.

Chiang Y.K., Overzier R. & Gebhardt K., 2013. *Ancient Light from Young Cosmic Cities: Physical and Observational Signatures of Galaxy Proto-clusters.* ApJ, 779, 2, 127.

Chiang Y.K., Overzier R.A., Gebhardt K. et al., 2017. *Galaxy Protoclusters as Drivers of Cosmic Star Formation History in the First 2 Gyr.* ApJ, 844, 2, L23.

Chu A., Durret F. & Márquez I., 2021. *Physical properties of brightest cluster galaxies up to redshift 1.80 based on HST data.* A&A, 649, A42.

Clowe D., Gonzalez A. & Markevitch M., 2004. *Weak-Lensing Mass Reconstruction of the Interacting Cluster 1E 0657-558: Direct Evidence for the Existence of Dark Matter*. The Astrophysical Journal, 604, 2, 596–603.

Coccato L., Gerhard O. & Arnaboldi M., 2010. *Distinct core and halo stellar populations and the formation history of the bright Coma cluster early-type galaxy NGC 4889*. Monthly Notices of the Royal Astronomical Society: Letters, 407, 1, L26–L30.

Cole S. & Kaiser N., 1989. *Biased clustering in the cold dark matter cosmogony.* MNRAS, 237, 1127–1146.

Collins C.A., Stott J.P., Hilton M. et al., 2009. *Early assembly of the most massive galaxies*. Nature, 458, 7238, 603–606.

Conroy C., Gunn J.E. & White M., 2009. *The Propagation of Uncertainties in Stellar Population Synthesis Modeling. I. The Relevance of Uncertain Aspects of Stellar Evolution and the Initial Mass Function to the Derived Physical Properties of Galaxies*. ApJ, 699, 1, 486–506.

Conroy C. & Gunn J.E., 2010. *The Propagation of Uncertainties in Stellar Population Synthesis Modeling. III. Model Calibration, Comparison, and Evaluation.* ApJ, 712, 2, 833–857.

Conselice C.J., Bershady M.A., Dickinson M. et al., 2003. *A Direct Measurement of Major Galaxy Mergers atiz/i3*. The Astronomical Journal, 126, 3, 1183–1207.

Conselice C.J., Mundy C.J., Ferreira L. et al., 2022. *A Direct Measurement of Galaxy Major and Minor Merger Rates and Stellar Mass Accretion Histories at Z &lt 3 Using Galaxy Pairs in the REFINE Survey*. The Astrophysical Journal, 940, 2, 168.

Contini E., De Lucia G., Villalobos et al., 2013. *On the formation and physical properties of the intracluster light in hierarchical galaxy formation models.* MNRAS, 437, 4, 3787–3802.

Contini E., Yi S.K. & Kang X., 2018. *The different growth pathways of Brightest Cluster Galaxies and the Intra-Cluster Light.* Monthly Notices of the Royal Astronomical Society.

Contini E., Yi S.K. & Kang X., 2019. *Theoretical Predictions of Colors and Metallicity of the Intracluster Light.* ApJ, 871, 1, 24.

Contini E., Gu Q., Ge X. et al., 2020. *The Roles of Mass and Environment in the Quenching of Galaxies. II.* The Astrophysical Journal, 889, 2, 156.

Contini E. & Gu Q., 2021. *Brightest Cluster Galaxies and Intracluster Light: Their Mass Distribution in the Innermost Regions of Groups and Clusters.* ApJ, 915, 2, 106.

Contini E., 2021. *On the Origin and Evolution of the Intra-Cluster Light: A Brief Review of the Most Recent Developments.* Galaxies, 9, 3, 60.

Cooke E.A., Hatch N.A., Muldrew S.I. et al., 2014. *A $z = 2.5$ protocluster associated with the radio galaxy MRC 2104-242: star formation and differing mass functions in dense environments.* MNRAS, 440, 4, 3262–3274.

Cooke E.A., Hatch N.A., Rettura A. et al., 2015. *The formation history of massive cluster galaxies as revealed by CARLA.* MNRAS, 452, 3, 2318–2336.

Cooke E.A., Hatch N.A., Stern D. et al., 2016. *A Mature Galaxy Cluster at z=1.58 around the Radio Galaxy 7C1753+6311.* ApJ, 816, 2, 83.

Cooper M.C., Coil A.L., Gerke B.F. et al., 2010. *Absence of evidence is not evidence of absence: the colour-density relation at fixed stellar mass persists to z ~1.* MNRAS, 409, 1, 337–345.

Costa-Duarte M.V., Viola M., Molino A. et al., 2018. *The galaxy environment in GAMA G3C groups using the Kilo Degree Survey Data Release 3.* MNRAS, 478, 1968–1979.

Cowie L.L. & Songaila A., 1977. *Thermal evaporation of gas within galaxies by a hot intergalactic medium.* Nature, 266, 501–503.

Croton D.J., Springel V., White S.D.M. et al., 2006. *The many lives of active galactic nuclei: cooling flows, black holes and the luminosities and colours of galaxies.* Monthly Notices of the Royal Astronomical Society, 365, 1, 11–28.

Cui W., Murante G., Monaco P. et al., 2013. *Characterizing diffused stellar light in simulated galaxy clusters.* Monthly Notices of the Royal Astronomical Society, 437, 1, 816–830.

De Lucia G. & Blaizot J., 2007. *The hierarchical formation of the brightest cluster galaxies.* MNRAS, 375, 1, 2–14.

De Lucia G., Weinmann S., Poggianti B.M. et al., 2012. *The environmental history of group and cluster galaxies in a Λ cold dark matter universe.* MNRAS, 423, 2, 1277–1292.

de Vaucouleurs G., 1959. *Classification and Morphology of External Galaxies.* Handbuch der Physik, 53, 275.

Dekel A. & Birnboim Y., 2006. *Galaxy bimodality due to cold flows and shock heating.* MNRAS, 368, 1, 2–20.

Dekel A., Sari R. & Ceverino D., 2009. *Formation of Massive Galaxies at High Redshift: Cold Streams, Clumpy Disks, and Compact Spheroids.* ApJ, 703, 1, 785–801.

DeMaio T., Gonzalez A.H., Zabludoff A. et al., 2015. *On the origin of the intracluster light in massive galaxy clusters.* Monthly Notices of the Royal Astronomical Society, 448, 2, 1162–1177.

DeMaio T., Gonzalez A.H., Zabludoff A. et al., 2017. *Lost but not forgotten: intracluster light in galaxy groups and clusters.* Monthly Notices of the Royal Astronomical Society, 474, 3, 3009–3031.

DeMaio T., Gonzalez A.H., Zabludoff A. et al., 2019. *The growth of brightest cluster galaxies and intracluster light over the past 10 billion years.* MNRAS, 491, 3, 3751–3759.

DeMaio T., Gonzalez A.H., Zabludoff A. et al., 2020a. *The growth of brightest cluster galaxies and intracluster light over the past 10 billion years.* MNRAS, 491, 3, 3751–3759.

DeMaio T., Gonzalez A.H., Zabludoff A. et al., 2020b. *The growth of brightest cluster galaxies and intracluster light over the past 10 billion years.* MNRAS, 491, 3, 3751–3759.

Diamond-Stanic A.M., Moustakas J., Tremonti C.A. et al., 2012. *High-velocity Outflows without AGN Feedback: Eddington-limited Star Formation in Compact Massive Galaxies.* ApJ, 755, 2, L26.

Diemer B. & Kravtsov A.V., 2014. *Dependence of the Outer Density Profiles of Halos on Their Mass Accretion Rate.* ApJ, 789, 1, 1.

Dolag K., Murante G. & Borgani S., 2010. *Dynamical difference between the cD galaxy and the diffuse, stellar component in simulated galaxy clusters.* Monthly Notices of the Royal Astronomical Society.

Dressler A., 1980. *Galaxy morphology in rich clusters: implications for the formation and evolution of galaxies.* ApJ, 236, 351–365.

Dressler A., Oemler Augustus J., Couch W.J. et al., 1997. *Evolution since z = 0.5 of the Morphology-Density Relation for Clusters of Galaxies.* ApJ, 490, 2, 577–591.

Durret F., Adami C., Cappi A. et al., 2011. *Galaxy cluster searches based on photometric redshifts in the four CFHTLS Wide fields.* A&A, 535, A65.

Ebeling H., Edge A.C., Mantz A. et al., 2010. *The X-ray brightest clusters of galaxies from the Massive Cluster Survey.* MNRAS, 407, 83–93.

Ellien A., Slezak E., Martinet N. et al., 2021. *DAWIS: a detection algorithm with wavelets for intracluster light studies.* Astronomy &amp Astrophysics, 649, A38.

Faber S.M., Willmer C.N.A., Wolf C. et al., 2007. *Galaxy Luminosity Functions to z˜1 from DEEP2 and COMBO-17: Implications for Red Galaxy Formation.* ApJ, 665, 1, 265–294.

Finoguenov A., Guzzo L., Hasinger G. et al., 2007. *The XMM-Newton Wide-Field Survey in the COSMOS Field: Statistical Properties of Clusters of Galaxies.* ApJS, 172, 1, 182–195.

Finoguenov A., Watson M.G., Tanaka M. et al., 2010. *X-ray groups and clusters of galaxies in the Subaru-XMM Deep Field.* MNRAS, 403, 4, 2063–2076.

Fioc M. & Rocca-Volmerange B., 1997. *PEGASE: a UV to NIR spectral evolution model of galaxies. Application to the calibration of bright galaxy counts.* A&A, 500, 507–519.

Fixsen D.J., Cheng E.S., Gales J.M. et al., 1996. *The Cosmic Microwave Background Spectrum from the Full COBE FIRAS Data Set.* ApJ, 473, 576.

Foley R.J., Andersson K., Bazin G. et al., 2011. *DISCOVERY AND COSMOLOGICAL IMPLICATIONS OF SPT-CL J2106-5844, THE MOST MASSIVE KNOWN CLUSTER ATz>1.* The Astrophysical Journal, 731, 2, 86.

Foltz R., Wilson G., Muzzin A. et al., 2018. *The Evolution of Environmental Quenching Timescales to $z \sim 1.6$: Evidence for Dynamically Driven Quenching of the Cluster Galaxy Population.* ApJ, 866, 2, 136.

Foreman-Mackey D., Hogg D.W., Lang D. et al., 2013. *emcee: The MCMC Hammer.* Publications of the Astronomical Society of the Pacific, 125, 925, 306–312.

Fossati M., Wilman D.J., Mendel J.T. et al., 2017. *Galaxy Environment in the 3D-HSTFields: Witnessing the Onset of Satellite Quenching atz∼ 1–2.* The Astrophysical Journal, 835, 2, 153.

Friedmann M. & Maoz D., 2018. *The rate of Type-Ia supernovae in galaxy clusters and the delay-time distribution out to redshift 1.75.* MNRAS, 479, 3, 3563–3581.

Fī A.R.I., 903. *uwar Al-Kawākib.*

Gabor J.M., Davé R., Finlator K. et al., 2010. *How is star formation quenched in massive galaxies?* Monthly Notices of the Royal Astronomical Society, 407, 2, 749–771.

Galametz A., Stern D., De Breuck C. et al., 2012. *The Mid-infrared Environments of High-redshift Radio Galaxies.* ApJ, 749, 2, 169.

George M.R., Leauthaud A., Bundy K. et al., 2011. *Galaxies in X-Ray Groups. I. Robust Membership Assignment and the Impact of Group Environments on Quenching.* ApJ, 742, 2, 125.

Giodini S., Finoguenov A., Pierini D. et al., 2012. *The galaxy stellar mass function of X-ray detected groups. Environmental dependence of galaxy evolution in the COSMOS survey.* A&A, 538, A104.

Girardi M., Biviano A., Giuricin G. et al., 1993. *Velocity Dispersions in Galaxy Clusters.* ApJ, 404, 38.

Gobat R., Rosati P., Strazzullo V. et al., 2008. *Star formation histories of early-type galaxies at $z = 1.2$ in cluster and field environments.* A&A, 488, 3, 853–860.

Golden-Marx J.B., Miller C.J., Zhang Y. et al., 2022. *The Observed Evolution of the Stellar Mass–Halo Mass Relation for Brightest Central Galaxies.* ApJ, 928, 1, 28.

Gómez P.L., Nichol R.C., Miller C.J. et al., 2003. *Galaxy Star Formation as a Function of Environment in the Early Data Release of the Sloan Digital Sky Survey.* ApJ, 584, 1, 210–227.

Gonçalves T.S., Martin D.C., Menéndez-Delmestre K. et al., 2012. *Quenching Star Formation at Intermediate Redshifts: Downsizing of the Mass Flux Density in the Green Valley.* ApJ, 759, 1, 67.

Gonzaga S., Hack W., Fruchter A. et al., 2012. *The DrizzlePac Handbook.*

Gonzalez A.H., Zabludoff A.I. & Zaritsky D., 2005. *Intracluster Light in Nearby Galaxy Clusters: Relationship to the Halos of Brightest Cluster Galaxies.* The Astrophysical Journal, 618, 1, 195.

Gonzalez A.H., Gettings D.P., Brodwin M. et al., 2019. *The Massive and Distant Clusters of iWISE/i Survey. I. Survey Overview and a Catalog of &gt2000 Galaxy Clusters at iz/i $\simeq$ 1.* The Astrophysical Journal Supplement Series, 240, 2, 33.

Granato G.L., De Zotti G., Silva L. et al., 2004. *A Physical Model for the Coevolution of QSOs and Their Spheroidal Hosts.* ApJ, 600, 2, 580–594.

Guennou, L., Adami, C., Da Rocha, C. et al., 2012. *Intracluster light in clusters of galaxies at redshifts 0.4 $<$ z $<$ 0.8.* A&A, 537, A64.

Gunn J.E. & Gott J. Richard I., 1972. *On the Infall of Matter Into Clusters of Galaxies and Some Effects on Their Evolution.* ApJ, 176, 1.

Gursky H., Kellogg E., Murray S. et al., 1971. *A Strong X-Ray Source in the Coma Cluster Observed by UHURU.* ApJ, 167, L81.

Haggar R., Gray M.E., Pearce F.R. et al., 2020. *The Three Hundred project: backsplash galaxies in simulations of clusters.* MNRAS, 492, 4, 6074–6085.

Haines C.P., Pereira M.J., Smith G.P. et al., 2015. *LoCuSS: THE SLOW QUENCHING OF STAR FORMATION IN CLUSTER GALAXIES AND THE NEED FOR PRE-PROCESSING.* The Astrophysical Journal, 806, 1, 101.

Harris W.E., Brown R.A., Durrell P.R. et al., 2020. *The PIPER Survey. I. An Initial Look at the Intergalactic Globular Cluster Population in the Perseus Cluster.* The Astrophysical Journal, 890, 2, 105.

Hatch N.A., Overzier R.A., Röttgering H.J.A. et al., 2008. *Diffuse UV light associated with the Spiderweb Galaxy: evidence for in situ star formation outside galaxies.* MNRAS, 383, 3, 931–942.

Hatch N.A., Kurk J.D., Pentericci L. et al., 2011. *Hα emitters in z˜ 2 protoclusters: evidence for faster evolution in dense environments.* MNRAS, 415, 4, 2993–3005.

Henriksen M. & Byrd G., 1996. *Tidal Triggering of Star Formation by the Galaxy Cluster Potential.* ApJ, 459, 82.

Henriques B.M.B., White S.D.M., Thomas P.A. et al., 2015. *Galaxy formation in the Planck cosmology - I. Matching the observed evolution of star formation rates, colours and stellar masses.* MNRAS, 451, 2663–2680.

Hilton M., Hasselfield M., Sifón C. et al., 2018. *The Atacama Cosmology Telescope: The Two-season ACTPol Sunyaev-Zeldovich Effect Selected Cluster Catalog.* ApJS, 235, 20.

Hoekstra H., Bartelmann M., Dahle H. et al., 2013. *Masses of Galaxy Clusters from Gravitational Lensing.* Space Science Reviews, 177, 1-4, 75–118.

Hou S.Q., He J.J., Parikh A. et al., 2017. *NON-EXTENSIVE STATISTICS TO THE COSMOLOGICAL LITHIUM PROBLEM.* The Astrophysical Journal, 834, 2, 165.

Hubble E., 1926. *No. 324. Extra-galactic nebulae.* Contributions from the Mount Wilson Observatory / Carnegie Institution of Washington, 324, 1–49.

Hubble E. & Humason M.L., 1931. *The Velocity-Distance Relation among Extra-Galactic Nebulae.* ApJ, 74, 43.

Hubble E.P., 1927. *The classification of spiral nebulae.* The Observatory, 50, 276–281.

Hubble E.P., 1929. *A spiral nebula as a stellar system, Messier 31.* ApJ, 69, 103–158.

Hubble E.P., 1936. *Realm of the Nebulae.*

Iodice E., Spavone M., Cantiello M. et al., 2017. *Intracluster Patches of Baryons in the Core of the Fornax Cluster.* ApJ, 851, 2, 75.

Ito K., Kashikawa N., Toshikawa J. et al., 2020. *The UV Luminosity Function of Protocluster Galaxies at $z \sim 4$: The Bright-end Excess and the Enhanced Star Formation Rate Density.* The Astrophysical Journal, 899, 1, 5.

Ivanov V.D., Rieke M.J., Engelbracht C.W. et al., 2004. *A Medium-Resolution Near-Infrared Spectral Library of Late-Type Stars. I.* ApJS, 151, 2, 387–397.

Jimé nez-Teja Y., Dupke R., Benítez N. et al., 2018. *Unveiling the Dynamical State of Massive Clusters through the ICL Fraction.* The Astrophysical Journal, 857, 2, 79.

Jiménez-Teja Y., Dupke R.A., de Oliveira R.L. et al., 2019. *J-PLUS: Analysis of the intracluster light in the Coma cluster.* Astronomy &amp Astrophysics, 622, A183.

Just D.W., Kirby M., Zaritsky D. et al., 2019. *Preprocessing among the Infalling Galaxy Population of EDisCS Clusters.* The Astrophysical Journal, 885, 1, 6.

Kaiser N., 1984. *On the spatial correlations of Abell clusters.* ApJ, 284, L9–L12.

Kawinwanichakij L., Papovich C., Quadri R.F. et al., 2014. *THE DISTRIBUTION OF SATELLITES AROUND MASSIVE GALAXIES AT 1 z 3 IN*

ZFOURGE/CANDELS: DEPENDENCE ON STAR FORMATION ACTIVITY. The Astrophysical Journal, 792, 2, 103.

Kawinwanichakij L., Papovich C., Quadri R.F. et al., 2017. *Effect of Local Environment and Stellar Mass on Galaxy Quenching and Morphology at 0.5 < z < 2.0*. The Astrophysical Journal, 847, 2, 134.

Kellogg E., Gursky H., Leong C. et al., 1971. *X-Ray Observations of the Virgo Cluster, NGC 5128, and 3c 273 from the UHURU Satellite*. ApJ, 165, L49.

Kodama T., Balogh M.L., Smail I. et al., 2004. *A panoramic Hα imaging survey of the z= 0.4 cluster Cl0024.0+1652 with Subaru*. MNRAS, 354, 4, 1103–1119.

Koyama Y., Kodama T., Nakata F. et al., 2011. *Red Star-forming Galaxies and Their Environment at z = 0.4 Revealed by Panoramic Hα Imaging*. ApJ, 734, 1, 66.

Krick J.E. & Bernstein R.A., 2007. *Diffuse Optical Light in Galaxy Clusters. II. Correlations with Cluster Properties*. The Astronomical Journal, 134, 2, 466–493.

Krick J.E., Glaccum W.J., Carey S.J. et al., 2012. *A Spitzer/IRAC Measure of the Zodiacal Light*. ApJ, 754, 1, 53.

Kriek M., van Dokkum P.G., Labbé I. et al., 2009. *An Ultra-Deep Near-Infrared Spectrum of a Compact Quiescent Galaxy at z = 2.2*. ApJ, 700, 1, 221–231.

Kriek M., van Dokkum P.G., Labbé I. et al., 2018. *FAST: Fitting and Assessment of Synthetic Templates*.

Krishnan C., Hatch N.A., Almaini O. et al., 2017. *Enhancement of AGN in a*

protocluster at z = 1.6. Monthly Notices of the Royal Astronomical Society, 470, 2, 2170–2178.

Kurk J.D., Pentericci L., Overzier R.A. et al., 2004. *A search for clusters at high redshift. IV. Spectroscopy of Hα emitters in a proto-cluster at z = 2.16.* A&A, 428, 817–821.

Larson R.B., 1974. *Dynamical models for the formation and evolution of spherical galaxies.* MNRAS, 166, 585–616.

Larson R.B., Tinsley B.M. & Caldwell C.N., 1980. *The evolution of disk galaxies and the origin of S0 galaxies.* ApJ, 237, 692–707.

Leavitt H.S. & Pickering E.C., 1912. *Periods of 25 Variable Stars in the Small Magellanic Cloud.* Harvard College Observatory Circular, 173, 1–3.

Lee-Brown D.B., Rudnick G.H., Momcheva I.G. et al., 2017. *The Ages of Passive Galaxies in a z = 1.62 Protocluster.* ApJ, 844, 1, 43.

Leja J., Carnall A.C., Johnson B.D. et al., 2019. *How to Measure Galaxy Star Formation Histories. II. Nonparametric Models.* ApJ, 876, 1, 3.

Lewis I., Balogh M., De Propris R. et al., 2002. *The 2dF Galaxy Redshift Survey: the environmental dependence of galaxy star formation rates near clusters.* MNRAS, 334, 3, 673–683.

Li Y., Habouzit M., Genel S. et al., 2020. *Correlations between Black Holes and Host Galaxies in the Illustris and IllustrisTNG Simulations.* The Astrophysical Journal, 895, 2, 102.

Lidman C., Iacobuta G., Bauer A.E. et al., 2013. *The importance of major mergers*

in the build up of stellar mass in brightest cluster galaxies at z = 1. Monthly Notices of the Royal Astronomical Society, 433, 1, 825–837.

Lima Neto G.B., 2016. *Notas de Aula em Astronomia Extragaláctica.*

Liu C., Peng E.W., Côté P. et al., 2015. *The Next Generation Virgo Cluster Survey. X. Properties of Ultra-compact Dwarfs in the M87, M49, and M60 Regions.* ApJ, 812, 34.

Lopes P.A.A., de Carvalho R.R., Gal R.R. et al., 2004. *The Northern Sky Optical Cluster Survey. IV. An Intermediate-Redshift Galaxy Cluster Catalog and the Comparison of Two Detection Algorithms.* AJ, 128, 1017–1045.

Lotz J.M., Jonsson P., Cox T.J. et al., 2011. *The Major and Minor Galaxy Merger Rates at z < 1.5.* ApJ, 742, 2, 103.

Madau P., Ferguson H.C., Dickinson M.E. et al., 1996. *High-redshift galaxies in the Hubble Deep Field: colour selection and star formation history to z~4.* MNRAS, 283, 4, 1388–1404.

Madau P. & Dickinson M., 2014. *Cosmic Star-Formation History.* Annual Review of Astronomy and Astrophysics, 52, 1, 415–486.

Mantz A.B., Allen S.W., Morris R.G. et al., 2017. *The metallicity of the intracluster medium over cosmic time: further evidence for early enrichment.* Monthly Notices of the Royal Astronomical Society, 472, 3, 2877–2888.

Mantz A.B., Abdulla Z., Allen S.W. et al., 2018. *The XXL Survey.* A&A, 620, A2.

Mapelli M., 2015. *Back to the green valley: how to rejuvenate an S0 galaxy through minor mergers.*

Maraston C., 2005. *Evolutionary population synthesis: models, analysis of the ingredients and application to high-z galaxies.* MNRAS, 362, 799–825.

Markevitch M., Gonzalez A.H., Clowe D. et al., 2004. *Direct Constraints on the Dark Matter Self-Interaction Cross Section from the Merging Galaxy Cluster 1E 0657-56.* The Astrophysical Journal, 606, 2, 819–824.

Mateo M., 1998. *DWARF GALAXIES OF THE LOCAL GROUP.* Annual Review of Astronomy and Astrophysics, 36, 1, 435–506.

Matharu J., Muzzin A., Brammer G.B. et al., 2021. *HST/WFC3 Grism Observations of $z \sim 1$ Clusters: Evidence for Rapid Outside-in Environmental Quenching from Spatially Resolved H Maps.* The Astrophysical Journal, 923, 2, 222.

McGee S.L., Bower R.G. & Balogh M.L., 2014. *Overconsumption, outflows and the quenching of satellite galaxies.* MNRAS, 442, L105–L109.

Mehrtens N., Romer A.K., Hilton M. et al., 2012. *The XMM Cluster Survey: optical analysis methodology and the first data release.* MNRAS, 423, 1024–1052.

Mei S., Hatch N.A., Amodeo S. et al., 2022. *Morphology-density Relation, Quenching, and Mergers in CARLA Clusters and Proto-Clusters at* $1.4 < z < 2.8$. arXiv e-prints, arXiv:2209.02078.

Melnick J., Giraud E., Toledo I. et al., 2012. *Intergalactic stellar populations in intermediate redshift clusters.* Monthly Notices of the Royal Astronomical Society, 427, 1, 850–858.

Merritt D., 1984. *Relaxation and tidal stripping in rich clusters of galaxies. II. Evolution of the luminosity distribution.* ApJ, 276, 26–37.

Mihos J.C., Harding P., Feldmeier J. et al., 2005. *Diffuse Light in the Virgo Cluster.* ApJ, 631, 1, L41–L44.

Minkowski R., 1960. *A New Distant Cluster of Galaxies.* ApJ, 132, 908–910.

Mo H.J., Jing Y.P. & White S.D.M., 1996. *The correlation function of clusters of galaxies and the amplitude of mass fluctuations in the Universe.* MNRAS, 282, 3, 1096–1104.

Montes M. & Trujillo I., 2017. *Intracluster light at the Frontier – II. The Frontier Fields Clusters.* Monthly Notices of the Royal Astronomical Society, 474, 1, 917–932.

Montes M. & Trujillo I., 2018. *Intracluster light: a luminous tracer for dark matter in clusters of galaxies.* MNRAS, 482, 2, 2838–2851.

Montes M., 2019. *The intracluster light and its role in galaxy evolution in clusters.*

Montes M., 2022. *The faint light in groups and clusters of galaxies.* Nature Astronomy, 6, 308–316.

Moore B., Katz N., Lake G. et al., 1996. *Galaxy harassment and the evolution of clusters of galaxies.* Nature, 379, 6566, 613–616.

Muldrew S.I., Hatch N.A. & Cooke E.A., 2015. *What are protoclusters? - Defining high-redshift galaxy clusters and protoclusters.* MNRAS, 452, 3, 2528–2539.

Muldrew S.I., Hatch N.A. & Cooke E.A., 2015. *What are protoclusters? – Defining high-redshift galaxy clusters and protoclusters.* MNRAS, 452, 3, 2528–2539.

Muldrew S.I., Hatch N.A. & Cooke E.A., 2018. *Galaxy evolution in protoclusters.* MNRAS, 473, 2, 2335–2347.

Murante G., Arnaboldi M., Gerhard O. et al., 2004. *The Diffuse Light in Simulations of Galaxy Clusters.* The Astrophysical Journal, 607, 2, L83–L86.

Muzzin A., Wilson G., Yee H.K.C. et al., 2009. *Spectroscopic Confirmation of Two Massive Red-Sequence-Selected Galaxy Clusters at z ~1.2 in the SpARCS-North Cluster Survey.* ApJ, 698, 2, 1934–1942.

Muzzin A., Wilson G., Yee H.K.C. et al., 2012a. *The Gemini Cluster Astrophysics Spectroscopic Survey (GCLASS): The Role of Environment and Self-regulation in Galaxy Evolution at z ~1.* ApJ, 746, 2, 188.

Muzzin A., Wilson G., Yee H.K.C. et al., 2012b. *The Gemini Cluster Astrophysics Spectroscopic Survey (GCLASS): The Role of Environment and Self-regulation in Galaxy Evolution at z ~1.* ApJ, 746, 2, 188.

Muzzin A., Marchesini D., Stefanon M. et al., 2013a. *The Evolution of the Stellar Mass Functions of Star-forming and Quiescent Galaxies to z = 4 from the COSMOS/UltraVISTA Survey.* ApJ, 777, 1, 18.

Muzzin A., Marchesini D., Stefanon M. et al., 2013b. *The Evolution of the Stellar Mass Functions of Star-forming and Quiescent Galaxies to z = 4 from the COSMOS/UltraVISTA Survey.* ApJ, 777, 1, 18.

Nantais J.B., van der Burg R.F.J., Lidman C. et al., 2016. *Stellar mass function of cluster galaxies at z ~1.5: evidence for reduced quenching efficiency at high redshift.* A&A, 592, A161.

Navarro J.F., Frenk C.S. & White S.D.M., 1996. *The Structure of Cold Dark Matter Halos.* ApJ, 462, 563.

Navarro J.F., Frenk C.S. & White S.D.M., 1997. *A Universal Density Profile from Hierarchical Clustering.* ApJ, 490, 2, 493–508.

Newman A.B., Ellis R.S., Andreon S. et al., 2014. *Spectroscopic Confirmation of the Rich z = 1.80 Galaxy Cluster JKCS 041 using the WFC3 Grism: Environmental Trends in the Ages and Structure of Quiescent Galaxies.* ApJ, 788, 1, 51.

Nierenberg A.M., Auger M.W., Treu T. et al., 2011. *Luminous Satellites of Early-type Galaxies. I. Spatial Distribution.* ApJ, 731, 1, 44.

Nierenberg A.M., Auger M.W., Treu T. et al., 2012. *Luminous Satellites. II. Spatial Distribution, Luminosity Function, and Cosmic Evolution.* ApJ, 752, 2, 99.

Noirot G., Vernet J., Breuck C.D. et al., 2016. *HST GRISM CONFIRMATION OF TWO z ∼ 2 STRUCTURES FROM THE CLUSTERS AROUND RADIO-LOUD AGN (CARLA) SURVEY.* ApJ, 830, 2, 90.

Noirot G., Stern D., Mei S. et al., 2018. *iHST/i Grism Confirmation of 16 Structures at 1.4 &lt iz/i &lt 2.8 from the Clusters Around Radio-Loud AGN (CARLA) Survey.* ApJ, 859, 1, 38.

Noordeh E., Canning R.E.A., Willis J.P. et al., 2021. *Quiescent galaxies in a virialized cluster at redshift 2: evidence for accelerated size growth.* MNRAS, 507, 4, 5272–5280.

Oemler Augustus J., 1974. *The Systematic Properties of Clusters of Galaxies. Photometry of 15 Clusters.* ApJ, 194, 1–20.

Oemler Augustus J., Dressler A., Gladders M.G. et al., 2013. *The IMACS Cluster Building Survey. III. The Star Formation Histories of Field Galaxies.* ApJ, 770, 1, 63.

Old L.J., Balogh M.L., van der Burg R.F.J. et al., 2021. *Erratum: The GOGREEN survey: the environmental dependence of the star-forming galaxy main sequence at 1.0 < z < 1.5.* MNRAS, 500, 1, 355–357.

Overzier R.A., 2016. *The realm of the galaxy protoclusters.* The Astronomy and Astrophysics Review, 24, 1.

Papovich C., Shipley H.V., Mehrtens N. et al., 2016. *The Spitzer-HETDEX Exploratory Large-area Survey.* ApJS, 224, 2, 28.

Papovich C., Kawinwanichakij L., Quadri R.F. et al., 2018. *The Effects of Environment on the Evolution of the Galaxy Stellar Mass Function.* ApJ, 854, 1, 30.

Patel S.G., Kelson D.D., Holden B.P. et al., 2011. *The Star-formation-rate-Density Relation at 0.6 < z < 0.9 and the Role of Star-forming Galaxies.* ApJ, 735, 1, 53.

Peng Y.j., Lilly S.J., Kovač K. et al., 2010. *Mass and Environment as Drivers of Galaxy Evolution in SDSS and zCOSMOS and the Origin of the Schechter Function.* ApJ, 721, 1, 193–221.

Pentericci L., Kurk J.D., Röttgering H.J.A. et al., 2000. *A search for clusters at high redshift. II. A proto cluster around a radio galaxy at z=2.16.* A&A, 361, L25–L28.

Penzias A.A. & Wilson R.W., 1965. *A Measurement of Excess Antenna Temperature at 4080 Mc/s.* ApJ, 142, 419–421.

Pickles A.J., 1998. *A Stellar Spectral Flux Library: 1150-25000 Å.* PASP, 110, 749, 863–878.

Pintos-Castro I., Yee H.K.C., Muzzin A. et al., 2019. *The Evolution of the Quenching of Star Formation in Cluster Galaxies since $z \sim 1$.* The Astrophysical Journal, 876, 1, 40.

Piotrowska J.M., Bluck A.F.L., Maiolino R. et al., 2021. *On the quenching of star formation in observed and simulated central galaxies: evidence for the role of integrated AGN feedback.* Monthly Notices of the Royal Astronomical Society, 512, 1, 1052–1090.

Planck Collaboration, Ade P.A.R., Aghanim N. et al., 2014. *Planck 2013 results. XVI. Cosmological parameters.* A&A, 571, A16.

Planck Collaboration, Ade P.A.R., Aghanim N. et al., 2016. *Planck 2015 results. XXIV. Cosmology from Sunyaev-Zeldovich cluster counts.* A&A, 594, A24.

Poggianti B.M., von der Linden A., Lucia G.D. et al., 2006. *The Evolution of the Star Formation Activity in Galaxies and Its Dependence on Environment.* The Astrophysical Journal, 642, 1, 188–215.

Press W.H. & Schechter P., 1974. *Formation of Galaxies and Clusters of Galaxies by Self-Similar Gravitational Condensation.* ApJ, 187, 425–438.

Puchwein E., Springel V., Sijacki D. et al., 2010. *Intracluster stars in simulations with active galactic nucleus feedback.* Monthly Notices of the Royal Astronomical Society, pages no–no.

Purcell C.W., Bullock J.S. & Zentner A.R., 2007. *Shredded Galaxies as the Source of Diffuse Intrahalo Light on Varying Scales.* ApJ, 666, 1, 20–33.

Rakos K., Schombert J. & Odell A., 2007. *Age and Metallicities of Cluster Galaxies: A1185 and Coma.* The Astrophysical Journal, 658, 2, 929.

Rettura A., Rosati P., Nonino M. et al., 2010. *Formation Epochs, Star Formation Histories, and Sizes of Massive Early-Type Galaxies in Cluster and Field Environments at z = 1.2: Insights from the Rest-Frame Ultraviolet.* ApJ, 709, 1, 512–524.

Rettura A., Rosati P., Nonino M. et al., 2010. *FORMATION EPOCHS, STAR FORMATION HISTORIES, AND SIZES OF MASSIVE EARLY-TYPE GALAXIES IN CLUSTER AND FIELD ENVIRONMENTS ATiz/i= 1.2: INSIGHTS FROM THE REST-FRAME ULTRAVIOLET.* The Astrophysical Journal, 709, 1, 512–524.

Riess A.G., 2019. *The expansion of the Universe is faster than expected.* Nature Reviews Physics, 2, 1, 10–12.

Roberts I.D., Parker L.C., Brown T. et al., 2019. *Quenching Low-mass Satellite Galaxies: Evidence for a Threshold ICM Density.* The Astrophysical Journal, 873, 1, 42.

Rodriguez-Gomez V., Genel S., Vogelsberger M. et al., 2015. *The merger rate of galaxies in the Illustris simulation: a comparison with observations and semi-empirical models.* MNRAS, 449, 1, 49–64.

Rogstad D.H., Rougoor G.W. & Whiteoak J.B., 1965. *Radio Emission in the Direction of Clusters of Galaxies.* ApJ, 142, 1665.

Rudick C.S., Mihos J.C. & McBride C., 2006. *The Formation and Evolution of Intracluster Light.* ApJ, 648, 2, 936–946.

Rudnick G.H., Tran K.V., Papovich C. et al., 2012. *A Tale of Dwarfs and Giants: Using a z = 1.62 Cluster to Understand How the Red Sequence Grew over the Last 9.5 Billion Years.* ApJ, 755, 1, 14.

Rykoff E.S., Rozo E., Busha M.T. et al., 2014. *redMaPPer. I. Algorithm and SDSS DR8 Catalog.* ApJ, 785, 104.

Santos-Lleo M., Schartel N., Tananbaum H. et al., 2009. *The first decade of science with Chandra and XMM-Newton.* Nature, 462, 7276, 997–1004.

Scaramella R., Amiaux J., Mellier Y. et al., 2022. *iEuclid/i preparation.* A&A, 662, A112.

Schaye J., Crain R.A., Bower R.G. et al., 2014. *The EAGLE project: simulating the evolution and assembly of galaxies and their environments.* MNRAS, 446, 1, 521–554.

Schechter P., 1976. *An analytic expression for the luminosity function for galaxies.* ApJ, 203, 297–306.

Schirmer M., 2013. *THELI: Convenient Reduction of Optical, Near-infrared, and Mid-infrared Imaging Data.* ApJS, 209, 21.

Schlegel D.J., Finkbeiner D.P. & Davis M., 1998. *Maps of Dust Infrared Emission for Use in Estimation of Reddening and Cosmic Microwave Background Radiation Foregrounds.* ApJ, 500, 2, 525–553.

Schneider P., 2006. *Extragalactic Astronomy and Cosmology.* Springer Berlin Heidelberg, Berlin, Heidelberg. ISBN 978-3-540-33174-2.

Sérsic J.L., 1963. *Influence of the atmospheric and instrumental dispersion on the brightness distribution in a galaxy.* Boletin de la Asociacion Argentina de Astronomia La Plata Argentina, 6, 41–43.

Sheth R.K., Mo H.J. & Tormen G., 2001. *Ellipsoidal collapse and an improved*

model for the number and spatial distribution of dark matter haloes. MNRAS, 323, 1, 1–12.

Shimakawa R., Kodama T., Hayashi M. et al., 2017. *MAHALO Deep Cluster Survey I. Accelerated and enhanced galaxy formation in the densest regions of a protocluster at z = 2.5.* Monthly Notices of the Royal Astronomical Society, 473, 2, 1977–1999.

Sifón C., Battaglia N., Hasselfield M. et al., 2016. *The Atacama Cosmology Telescope: dynamical masses for 44 SZ-selected galaxy clusters over 755 square degrees.* MNRAS, 461, 1, 248–270.

Silk J. & Rees M.J., 1998. *Quasars and galaxy formation.* A&A, 331, L1–L4.

Simons R.C., Papovich C., Momcheva I. et al., 2021. *CLEAR: The Gas-phase Metallicity Gradients of Star-forming Galaxies at 0.6 &lt z &lt 2.6.* The Astrophysical Journal, 923, 2, 203.

Skrutskie M.F., Cutri R.M., Stiening R. et al., 2006. *The Two Micron All Sky Survey (2MASS).* AJ, 131, 2, 1163–1183.

Snowden S.L., Mushotzky R.F., Kuntz K.D. et al., 2007. *A catalog of galaxy clusters observed by XMM-Newton.* Astronomy &amp Astrophysics, 478, 2, 615–658.

Sobral D., Best P.N., Smail I. et al., 2011. *The dependence of star formation activity on environment and stellar mass at z∼ 1 from the HiZELS-Hα survey.* MNRAS, 411, 1, 675–692.

Springel V., Frenk C.S. & White S.D.M., 2006. *The large-scale structure of the Universe.* Nature, 440, 7088, 1137–1144.

Stalder B., Ruel J., Šuhada R. et al., 2013. *SPT-CL J0205–5829: Az= 1.32 EVOLVED MASSIVE GALAXY CLUSTER IN THE SOUTH POLE TELESCOPE SUNYAEV-ZEL'DOVICH EFFECT SURVEY.* The Astrophysical Journal, 763, 2, 93.

Staniszewski Z., Ade P.A.R., Aird K.A. et al., 2009. *Galaxy Clusters Discovered with a Sunyaev-Zel'dovich Effect Survey.* ApJ, 701, 32–41.

Strateva I., Ivezić Ž., Knapp G.R. et al., 2001. *Color Separation of Galaxy Types in the Sloan Digital Sky Survey Imaging Data.* AJ, 122, 4, 1861–1874.

Strazzullo V., Pannella M., Mohr J.J. et al., 2019. *Galaxy populations in the most distant SPT-SZ clusters. I. Environmental quenching in massive clusters at 1.4* $\lesssim z \lesssim$ *1.7.* A&A, 622, A117.

Sunyaev R.A. & Zeldovich Y.B., 1969. *Distortions of the Background Radiation Spectrum.* Nature, 223, 721–722.

Sunyaev R.A. & Zeldovich Y.B., 1970. *The Spectrum of Primordial Radiation, its Distortions and their Significance.* Comments on Astrophysics and Space Physics, 2, 66.

Sunyaev R.A. & Zeldovich Y.B., 1972. *Formation of Clusters of Galaxies; Protocluster Fragmentation and Intergalactic Gas Heating.* A&A, 20, 189.

Takey A., Schwope A. & Lamer G., 2013. *The 2XMMi/SDSS Galaxy Cluster Survey. II. The optically confirmed cluster sample and the* L_X *- T relation.* A&A, 558, A75.

Takey A., Schwope A. & Lamer G., 2014. *The 2XMMi/SDSS Galaxy Cluster Survey. III. Clusters associated with spectroscopically targeted luminous red galaxies in SDSS-DR10.* A&A, 564, A54.

Takey A., Durret F., Márquez I. et al., 2019. *The 3XMM/SDSS Stripe 82 Galaxy Cluster Survey - II. X-ray and optical properties of the cluster sample.* MNRAS, 486, 4863–4879.

Tal T., Wake D.A. & van Dokkum P.G., 2012. *Observations of Dark and Luminous Matter: The Radial Distribution of Satellite Galaxies around Massive Red Galaxies.* ApJ, 751, 1, L5.

Tal T., van Dokkum P.G., Franx M. et al., 2013. *Galaxy Environments over Cosmic Time: The Non-evolving Radial Galaxy Distributions around Massive Galaxies since z = 1.6.* ApJ, 769, 1, 31.

Tanaka M., Kodama T., Arimoto N. et al., 2006. *Spectroscopically confirmed large-scale structures associated to a z= 0.83 cluster.* MNRAS, 365, 4, 1392–1404.

Trussler J., Maiolino R., Maraston C. et al., 2019. *Both starvation and outflows drive galaxy quenching.* Monthly Notices of the Royal Astronomical Society, 491, 4, 5406–5434.

van den Bosch F.C., Aquino D., Yang X. et al., 2008. *The importance of satellite quenching for the build-up of the red sequence of present-day galaxies.* Monthly Notices of the Royal Astronomical Society, 387, 1, 79–91.

van der Burg, Rudnick, Gregory, Balogh, Michael L. et al., 2020. *The GOGREEN Survey: A deep stellar mass function of cluster galaxies at 1.0 < z < 1.4 and the complex nature of satellite quenching.* A&A, 638, A112.

van der Burg R.F.J., Muzzin A., Hoekstra H. et al., 2013. *The environmental dependence of the stellar mass function at z ~1. Comparing cluster and field between the GCLASS and UltraVISTA surveys.* A&A, 557, A15.

van der Burg R.F.J., McGee S., Aussel H. et al., 2018. *The stellar mass function of galaxies in Planck-selected clusters at $0.5 < z < 0.7$: new constraints on the timescale and location of satellite quenching.* A&A, 618, A140.

Vandame B., 2004. *Processing multi-wavelwength and wide-field imaging data: application to the ESO imaging survey.* PhD Thesis, Université de Nice-Sophia Antipolis, France.

Vikhlinin A., Kravtsov A., Forman W. et al., 2006. *Chandra Sample of Nearby Relaxed Galaxy Clusters: Mass, Gas Fraction, and Mass-Temperature Relation.* ApJ, 640, 691–709.

Vikhlinin A., Kravtsov A.V., Burenin R.A. et al., 2009. *Chandra Cluster Cosmology Project III: Cosmological Parameter Constraints.* ApJ, 692, 2, 1060–1074.

Voit G.M., 2005. *Tracing cosmic evolution with clusters of galaxies.* Reviews of Modern Physics, 77, 207–258.

Wang W. & White S.D.M., 2012. *Satellite abundances around bright isolated galaxies.* Monthly Notices of the Royal Astronomical Society, 424, 4, 2574–2598.

Wang W., Sales L.V., Henriques B.M.B. et al., 2014. *Satellite abundances around bright isolated galaxies – II. Radial distribution and environmental effects.* Monthly Notices of the Royal Astronomical Society, 442, 2, 1363–1378.

Watson D.F., Berlind A.A. & Zentner A.R., 2012. *Constraining Satellite Galaxy Stellar Mass Loss and Predicting Intrahalo Light. I. Framework and Results at Low Redshift.* ApJ, 754, 2, 90.

Webb K., Balogh M.L., Leja J. et al., 2020. *The GOGREEN survey: post-infall environmental quenching fails to predict the observed age difference between quiescent field and cluster galaxies at $z > 1$.* MNRAS, 498, 4, 5317–5342.

Wen Z.L., Han J.L. & Liu F.S., 2012. *A Catalog of 132,684 Clusters of Galaxies Identified from Sloan Digital Sky Survey III.* ApJS, 199, 34.

Werner S.V., Hatch N.A., Muzzin A. et al., 2021. *Satellite quenching was not important for iz/i ∼ 1 clusters: most quenching occurred during infall.* Monthly Notices of the Royal Astronomical Society, 510, 1, 674–686.

Werner S.V., Cypriano E.S., Gonzalez A.H. et al., 2022. *S-PLUS DR1 galaxy clusters and groups catalogue using PzWav.* Monthly Notices of the Royal Astronomical Society. Stac3273.

Wetzel A.R., Tinker J.L., Conroy C. et al., 2013. *Galaxy evolution in groups and clusters: satellite star formation histories and quenching time-scales in a hierarchical Universe.* MNRAS, 432, 1, 336–358.

Whiley I.M., Aragó n-Salamanca A., Lucia G.D. et al., 2008. *The evolution of the brightest cluster galaxies sinceiz/i∼ 1 from the ESO Distant Cluster Survey (EDisCS).* MNRAS, 387, 3, 1253–1263.

White S.D.M. & Rees M.J., 1978. *Core condensation in heavy halos: a two-stage theory for galaxy formation and clustering.* MNRAS, 183, 341–358.

White S.D.M. & Frenk C.S., 1991. *Galaxy Formation through Hierarchical Clustering.* ApJ, 379, 52.

Williams B.F., Ciardullo R., Durrell P.R. et al., 2007. *The Metallicity Distribution of Intracluster Stars in Virgo.* The Astrophysical Journal, 656, 2, 756–769.

Williams R.J., Quadri R.F., Franx M. et al., 2009. *DETECTION OF QUIESCENT GALAXIES IN A BICOLOR SEQUENCE FROMZ= 0-2.* The Astrophysical Journal, 691, 2, 1879–1895.

Willis J.P., Clerc N., Bremer M.N. et al., 2013. *Distant galaxy clusters in the XMM Large Scale Structure survey.* MNRAS, 430, 1, 134–156.

Willis J.P., Canning R.E.A., Noordeh E.S. et al., 2020a. *Spectroscopic confirmation of a mature galaxy cluster at a redshift of 2.* Nature, 577, 7788, 39–41.

Willis J.P., Canning R.E.A., Noordeh E.S. et al., 2020b. *Spectroscopic confirmation of a mature galaxy cluster at a redshift of 2.* Nature, 577, 7788, 39–41.

Willmer C.N.A., 2018. *The Absolute Magnitude of the Sun in Several Filters.* The Astrophysical Journal Supplement Series, 236, 2, 47.

Wilson G., Muzzin A., Yee H.K.C. et al., 2009a. *Spectroscopic Confirmation of a Massive Red-Sequence-Selected Galaxy Cluster at z = 1.34 in the SpARCS-South Cluster Survey.* ApJ, 698, 2, 1943–1950.

Wilson G., Muzzin A., Yee H. et al., 2009b. *The SpARCS z > 1 Cluster Survey.* volume 213 of *American Astronomical Society Meeting Abstracts*, page 315.01.

Wylezalek D., Galametz A., Stern D. et al., 2013. *Galaxy Clusters around Radio-loud Active Galactic Nuclei at 1.3 < z < 3.2 as Seen by Spitzer.* ApJ, 769, 1, 79.

Wylezalek D., Vernet J., Breuck C.D. et al., 2014. *THE GALAXY CLUSTER MID-INFRARED LUMINOSITY FUNCTION AT 1.3 &ltiz/i&lt 3.2.* ApJ, 786, 1, 17.

Zhang Y., Yanny B., Palmese A. et al., 2019. *Dark Energy Survey Year 1 Results: Detection of Intracluster Light at Redshift ∼ 0.25.* ApJ, 874, 2, 165.

Zubovas K., Nayakshin S., King A. et al., 2013. *AGN outflows trigger starbursts*

in gas-rich galaxies. Monthly Notices of the Royal Astronomical Society, 433, 4, 3079–3090.

Zwicky F., 1933a. *Die Rotverschiebung von extragalaktischen Nebeln.* Helvetica Physica Acta, 6, 110–127.

Zwicky F., 1933b. *Die Rotverschiebung von extragalaktischen Nebeln.* Helvetica Physica Acta, 6, 110–127.